

Electronic, adsorption, and transport properties of diamondoid-based complexes

Von der Fakultät Mathematik und Physik und dem
Stuttgart Research Centre for Simulation Technology
(SRC SimTech) der Universität Stuttgart zur Erlangung
der Würde eines Doktors der Naturwissenschaften
(Dr. rer. nat.) genehmigte Abhandlung

Vorgelegt von

Bibek Adhikari

aus Jhapa, Nepal

Hauptberichter: Jun. Prof. Dr. Maria Fyta

Mitberichter: Prof. Dr. Siegfried Schmauder

Mitberichter: Prof. Dr. Udo Seifert

Tag der mündlichen Prüfung: 24.03.2017

Institut für Computerphysik der Universität Stuttgart

2017

Erklärung

Hiermit versichere ich, die vorliegende Arbeit selbstständig verfasst und keine anderen als die angegebenen Quellen und Hilfsmittel benutzt, sowie die Zitate deutlich kenntlich gemacht zu haben.

Stuttgart, den 24.03.2017

Bibek Adhikari

Acknowledgements

I would like to thank my advisor Jun. Prof. Maria Fyta for the opportunity to work with her in the field of solid state physics and quantum chemistry. She has been a great support during this time. This thesis would not have been possible without her scientific and technical guidance. I would also like to thank Prof. Siegfried Schmauder and Prof. Udo Seifert for being the co-referees of this thesis.

I am very grateful to Prof. Sheng Meng for hosting me as a guest student in his group at the Institute of Physics, Chinese Academy of Sciences and for granting me the use of its computational resources. This thesis would have been incomplete without the results obtained from my stay in China. Special thanks go to Huixia Fu, Jin Zhang, and Zijing Ding for their invaluable cooperation and fruitful scientific discussions.

Many thanks to Dr. Christos Mathioudakis, Ganesh Sivaraman, and Balaji Muthuraman who contributed and collaborated with me in different projects which are a part of this thesis. I would like to thank Frank Maier for his kind help in proof-reading the Zusammenfassung of this thesis, other colleagues and the administrative staff from the Institute for Computational Physics for their help and advice during my time at the institute. I would like to thank the SimTech staff for the organization of the fun and refreshing Ph.D. weekends and the annual Graduate School seminars.

I would also like to acknowledge the financial support from the Juniorprofessorenprogramm funded by the Ministry of Science, Research, and the Arts Baden-Württemberg (MWK) and from the collaborative network SFB 716 "Dynamic simulations of systems with large particle numbers" funded by the German Funding Agency (Deutsche Forschungsgemeinschaft-DFG). This research was supported in part by the bwHPC initiative and the bwHPC-C5 project provided through associated computing services of the JUSTUS HPC facility at the University of Ulm.

Finally, I would like to thank my family in Nepal and my friends in Stuttgart, especially Liana without whom I would have not been able to come this far.

Summary

Quantum simulation is an invaluable tool to researchers from various fields of scientific research. It allows the investigation of various complex condensed matter in the regimes of physics, chemistry, and biology. In this work, we focused our attention in unraveling the physical, chemical, electronic, transport, and optical properties of diamondoids and their complexes through quantum simulations. We have implemented a bottom-up approach where we move from the doping and functionalization of single diamondoids up to the diamondoid-based molecular devices. Naturally, diamondoids have been extracted from petroleum and also have been synthesized in the lab. These diamondoids are hydrogen terminated carbon cage-like structures which have lattice structure similar to diamond. As a result, they are found to be as rigid and stiff as diamonds and are comparable to the stiffness of graphite and carbon nanotubes. In addition to their strong physical properties, they are also the building blocks for important drugs. Furthermore, because they have a negative electron affinity, they are potentially useful in molecular electronics and electron-emitting devices.

Electronic properties were probed by modelling the doping and functionalization possibilities of diamondoids starting from adamantane up to heptamantane. For the doped diamondoids, boron, nitrogen, silicon, oxygen, and phosphorus were used. These dopants substituted a carbon site according to an energy minimization criterion for the choice of the doping site. A single- and double-functionalization using an amine- and a thiol-group involved the substitution of a hydrogen site. The analysis started from the smallest adamantane, while the effect of isomerization, using four isomers of tetramantane was also investigated. The electronic properties of all these cases were probed through the electronic density of states and the frontier orbitals, HOMO and LUMO. The main goal of this study was the evaluation of the electronic band gap i.e., the conducting and optical properties of these modified diamondoids. We observed a decrease in the band gap for all doped and functionalized diamondoids as compared to the respective values of unmodified diamondoids. This decrease was also evident in the double-functionalized molecules moving from the smallest adamantane up to heptamantane. The band gap variation was found to be related to a strong localization of the frontier orbitals on the modified diamondoids. In addition to showing the possibility of selectively tuning the electronic properties of diamondoids, we also investigated the optical properties of these complexes. The optical properties were only explored for adamantane and

diamantane which were modified through single and double-functionalization. Different functional groups lead to different electronic and optical properties, while a double-functionalization as compared to a single-functionalization decreases even further the electronic and optical band gap, moving it towards the conducting region for the ground state and towards the visible region for the excited state. We chose representative atoms and functional groups but more can be tested.

Accordingly, synthesizing diamondoid-based complexes of specific size and modification has the potential to tune their electronic and optical properties. In terms of practical applications, the presence of functional groups provides additional functional properties, as the diamondoids include sites that not only tune their properties but also provide binding sites to other structures. The fact that a double functionalization leads to a larger increase of the optical properties provides the potential to form novel diamondoid-based emission devices which include one functional group for the attachment of the diamondoid on the substrate and another atomic group like the N-heterocyclic carbenes (NHC)s molecules which provide the diamondoid with functionalities. The NHCs can promote the selective binding or sensing of molecules in its vicinity which was evident in the study of the adsorption of carbene-functionalized diamondoids on metal surfaces. Keeping that goal in mind, we analyzed the self-assembly of carbene-mediated diamondoids over Au(111), Ag(111), and Pt(111) metal surfaces, respectively. The self-assembly of these complexes was probed through the stability and adsorption, binding possibilities, and surface morphology after adsorption. In our study, Au(111) and Pt(111) were the most efficient metal surfaces for the adsorption of carbene-mediated diamondoid self-assembled monolayers (SAM)s. Orbitals of d-symmetry are essential in order to have orbital overlapping with carbon p-electrons and bond formation as in the case of the Au(111) and Pt(111) surfaces. In Ag(111), the weaker bonding was justified by the non-availability of the d-orbital of the metallic first layer of the surface around the Fermi level. Calculation of the work functions of carbene-mediated diamondoid SAMs on Au(111), Ag(111), and Pt(111) surfaces demonstrated that the modulation of the work function with respect to the properties of clean metal surfaces and a dynamic tuning can be easily achieved in NHC-ada/metal devices for organic electronic applications. The charge re-distribution and the simulated STM images of the surfaces showed that on Pt(111) the whole carbene ring of the NHC-ada molecule is associated with the SAM/metal bonding, increasing the adsorption energy of SAMs. By comparing the molecular adsorption energies on reconstructed Au(111), Ag(111), and Pt(111) surfaces, we found out that these geometries are stable and of practical interest. However, it is essential to examine the thermal stability of these structures and the influence of environmental conditions on their stability. Nevertheless, carbene molecules have proven to be a better alternative to the thiol-based bonding of diamondoids on metallic surfaces, opening up the path for more stable and efficient SAMs/metal devices.

In search of highly efficient diamondoid-based molecular devices, electronic transport across molecular junctions made up of functionalized and doped diamondoids were investigated. A small diamondoid was placed in between the two gold electrodes of the nano gap. The diamondoids were covalently bonded to the gold electrodes through two different molecules, a thiol group, and an N-heterocyclic carbene molecule. The transport properties of the diamondoid-based molecular device were evaluated with respect to these two binding possibilities and the size of the diamondoid. We also investigated the influence of doping the diamondoid on the properties of the molecular device. The comparison of the results was discussed based on the functionalization, the type of dopants, and the diamondoid size. A di-thiol linker group was found to be efficient compared to a carbene group attached to the Au(111) nano gap. Using a nitrogen atom to dope the diamondoids lead to a considerable increase of the electron transmission across the device. We showed the asymmetric feature of the I-V curve applying the positive and negative bias, which indicates the diode-like property resulting in rectification within a very small range of bias voltages. The zero bias transmission function of undoped diamondoid systems reveals that the highest occupied molecular orbitals (HOMO) peaks are away from the Fermi level, which was beyond any practical voltage bias window. In all the cases, the efficiency of the device was manifested and is discussed in view of novel nanotechnological applications. We were able to selectively tuned the electronic and transport properties of the diamondoid-based molecular junctions by doping the molecules with boron and nitrogen. Doping with nitrogen leads to an addition of a transmission peak very close to the Fermi level leading to higher molecular conductance. Increasing the diamondoid size leads to the slight decrease in the zero bias conductance. Such a decrease was also observed when using the carbene molecules as the linker of the diamondoid on the nano gap surfaces. Bias dependent transport calculations revealed that doping leads to a higher rectification ratio at very small applied bias voltages. This behavior is the result of the energy shift of the HOMO peaks with respect to the zero bias case. The rectifying effect in N-doped diamondoids is related to the asymmetry in the structure when introducing the dopant. Since a similar asymmetry is introduced by means of doping in the case of B and B-N co-doping, we can assume that a similar rectifying behavior is observed also for these latter cases.

Zusammenfassung

Quantensimulation ist ein unschätzbares Werkzeug für Forscher aus verschiedenen Bereichen der Wissenschaft. Sie ermöglicht die Untersuchung verschiedener komplexer kondensierter Materie in der Physik, Chemie und Biologie. In dieser Arbeit geht es um die Entschlüsselung der physikalischen, chemischen, elektrischen, transport und optischen Eigenschaften von Diamantoiden und deren Komplexen durch Quantensimulationen. Wir haben einen bottom-up Ansatz implementiert, beginnend mit der Dotierung und Funktionalisierung einzelner Diamantoiden bis hin zu Diamantoid-basierten molekularen Systemen. Diamantoide werden nicht nur natürlich aus Petroleum extrahiert, sondern auch im Labor synthetisiert.

Diese Diamantoide sind Wasserstoff-terminierte Kohlenstoffstrukturen, deren Kohlenstoffgerüste denen von Diamanten gleichen. Aus diesem Grund sind sie so starr und steif wie Diamanten und ihre Steifigkeit mit der von Graphit- und Kohlenstoff-Nanoröhrchen vergleichbar. Abgesehen von ihrer Robustheit dienen sie auch als Bausteine wichtiger Medikamente. Aufgrund der negativen Elektronenaffinität von Diamantoiden weisen sie ein hohes Potential zum Einsatz in molekularelektrischen und Elektronen-emittierenden Systemen auf.

In dieser Dissertation wurden die elektrischen Eigenschaften durch Modellierung der Dotierungs- und Funktionalisierungsmöglichkeiten von Diamantoiden, ausgehend von Adamantan bis hin zu Heptamantan, untersucht. Für die dotierten Diamantoide wurden Bor, Stickstoff, Silizium, Sauerstoff und Phosphor verwendet. Diese Dotierungen ersetzen eine Kohlenstoffstelle aufgrund eines Energieminimierungskriteriums bei der Wahl der Dotierungsstelle. Die Einzel- und Doppelfunktionalisierung der Diamantoiden erfolgte durch die Substituierung eines Wasserstoffatoms mit einer Amin- und einer Thiol-Gruppe.

Die Untersuchung begann beim kleinsten Diamantoid, dem Adamantan, wobei der Einfluss der Isomerisierung an vier Isomeren von Tetramantan ebenfalls erarbeitet wurde. Die elektrischen Eigenschaften aller dieser Strukturen wurden mittels der Zustandsdichte, sowie den Grenzorbitalen HOMO (highest occupied molecular orbital) und LUMO (lowest unoccupied molecular orbital) untersucht. Das Hauptziel dieser Arbeit war die Auswertung der elektrischen Bandlücke, d.h. die Leitfähigkeit und optischen Eigenschaften dieser modifizierten Diamantoide. Wir haben eine Abnahme der Bandlücke für alle dotierten und

funktionalisierten Diamantoiden beobachtet, im Vergleich zu den jeweiligen Werten von nichtmodifizierten Diamantoiden. Diese Abnahme war auch in den doppelfunktionalisierten Molekülen sichtbar, die sich vom Adamantan bis hin zu Heptamantan erstrecken.

Es wurde festgestellt, dass die Bandlückenvariation auf eine starke Lokalisierung der Grenzorbitale in den modifizierten Diamantoiden zurückzuführen ist. Dadurch wird eine gezielte Abstimmung der elektrischen Eigenschaften von Diamantoiden möglich. Zusätzlich haben wir auch die optischen Eigenschaften dieser Komplexe für Adamantan und Diamantan untersucht, die durch Einzel- und Doppelfunktionalisierung modifiziert wurden. Dabei wurde beobachtet, dass unterschiedliche funktionelle Gruppen zu unterschiedlichen elektrischen und optischen Eigenschaften führen. Verglichen mit der Einzelfunktionalisierung schiebt die Doppelfunktionalisierung die elektrische und optische Bandlücke noch weiter in den leitenden Bereich des Grundzustandes und somit in die Richtung des sichtbaren Bereichs des angeregten Zustandes. Wir wählten repräsentative Atome und funktionelle Gruppen, um die Tendenz darzulegen, wobei mehr noch getestet werden kann.

Dementsprechend könnte durch gezielte Herstellung von Diamantoid-basierten Komplexen spezifischer Größe und Modifikation die elektrischen und optischen Eigenschaften dieser Komplexe abgestimmt werden. Zusätzlich werden durch funktionelle Atomgruppen weitere Bindungsmöglichkeiten geschaffen, sodass eine Bindung mit anderen Strukturen ermöglicht wird. Die Tatsache, dass eine Doppelfunktionalisierung zu einer großen Zunahme der optischen Eigenschaften führt, bietet die Möglichkeit, neue diamantoid-basierte Emitter zu bilden, wobei eine funktionelle Gruppe der Befestigung des Diamantoids auf einem Substrat dient und eine weitere den Diamantoid mit Funktionalitäten versorgt. Ein Beispiel einer solchen Atomgruppe wäre ein N-Heterocyclisches Carbene (NHC) Molekül. NHC können die selektive Bindung oder Detektion von naheliegenden Molekülen begünstigen, was bei der Untersuchung der Adsorption von Carben-funktionalisierten Diamantoiden auf Metalloberflächen deutlich wurde. In Anbetracht dieser Untersuchung haben wir die Selbstorganisation von Carben-vermittelten Diamantoiden über Gold (Au(111)-, Silber (Ag(111))-bzw. Platinum (Pt(111))-Metalloberflächen analysiert.

Die Selbstorganisation dieser Komplexe wurde durch die Stabilität, Adsorption, Bindungsmöglichkeiten und Oberflächenmorphologie untersucht. Wir konnten zeigen, dass Au(111) und Pt(111) die effizientesten Metalloberflächen für die Adsorption von carbenvermittelten Diamantoid-basierten selbstorganisierten Monolagen (SAM) waren. Unsere Ergebnisse haben weiter gezeigt, dass molekulare Orbitale der d-Symmetrie für die Orbitalüberlappung mit Kohlenstoff-p-Elektronen und die Bindungsbildung wie im Fall der Au(111)- und Pt(111)-Oberflächen essentiell sind. In Ag(111)-Oberflächen wurde die schwächere Bindung durch die Nichtverfügbarkeit des d-Orbitales der metallischen ersten Schicht der Oberfläche um das Fermi-Niveau gerechtfertigt. Die

Berechnung der Arbeitsfunktionen von Carben-vermittelten Diamantoid-SAMs auf Au(111)-, Ag(111)-, und Pt(111)- Oberflächen zeigte auf, dass durch die Modulation der Arbeitsfunktionen in Bezug zu den Eigenschaften einer reinen Metalloberfläche, eine dynamische Abstimmung von NHC-ada/Metall-Bauelementen für organische elektrische Anwendungen möglich wird.

Die Ladungsverteilung und die simulierten STM-Abbildungen der Oberflächen machten sichtbar, dass auf Pt(111) der gesamte Carbenring des NHC-ada-Moleküls mit der SAM/Metall-Bindung assoziiert ist, was die Adsorptionsenergie von SAMs erhöht. Durch Vergleich der molekularen Adsorptionsenergien auf rekonstruierten Au(111)-, Ag(111)- und Pt(111)-Oberflächen haben wir herausgefunden, dass diese Geometrien stabil und von praktischem Interesse sind. Es ist jedoch wichtig, die thermische Stabilität dieser Strukturen und den Einfluss der Umweltbedingungen auf ihre Stabilität zu untersuchen. Durch dieser Arbeit haben sich Carbenmoleküle als eine bessere Alternative zur thiolbasierten Bindung von Diamantoiden auf metallische Oberflächen erwiesen, was den Weg für stabilere und effizientere SAMs/Metall-Bauelemente öffnet.

Auf der Suche nach hocheffizienten Diamantoid-basierten molekularen Systemen wurde der elektrische Transport innerhalb von molekularen Verbindungen zwischen funktionalisierten und dotierten Diamantoiden untersucht. Dafür platzierten wir einen Diamantoid zwischen zwei Goldelektroden, deren Abstand wenige Nanometer betrug. Die untersuchten Diamantoiden wurden durch zwei unterschiedliche Moleküle, einer Thiolgruppe und einem N-heterocyclischen Carbenmolekül, kovalent an die Goldelektroden gebunden. Die Transporteigenschaften des diamantoidbasierten molekularen Systems wurden hinsichtlich dieser beiden Bindungsmöglichkeiten und der Größe des Diamantoids ausgewertet. Ebenso untersuchten wir den Einfluss der Dotierung des Diamantoids auf die Eigenschaften des molekularen Systems. Der Vergleich der Ergebnisse wurde anhand der Funktionalisierung, der Dotierung und der Diamantoidgröße diskutiert. Eine Di-Thiol-Linkergruppe hat sich als effizienter erwiesen, im Vergleich zu einer an den Goldelektroden gebundenen Carbengruppe. Die Verwendung eines Stickstoffatoms zur Dotierung der Diamantoiden führte zu einer erheblichen Verbesserung der Elektronenübertragung durch das molekulare System. Wir zeigten den asymmetrischen Verlauf der Strom-Spannungs-Kurve (I-V) durch Anlegen einer positiven und negativen Vorspannung. Die Kurve zeigte eine diodenartige Eigenschaft auf, die zu einer Gleichrichtung innerhalb eines sehr kleinen Bereichs von Vorspannungen führt. Die Transmissionsfunktion bei keiner Vorspannung für nicht dotierte Diamantoid-basierte Systeme zeigte, dass die Peaks der höchst besetzten molekularen Orbitale (HOMO) vom Fermi-Niveau entfernt sind und somit entfernt vom nutzbaren Bereich für eine Vorspannung. In allen Fällen zeigte sich die Effizienz des Diamantoid-basierten Systems und diese wurde im Hinblick auf neue nanotechnologische Anwendungen erörtert. Wir konnten die Elektronen- und Transporteigenschaften der Diamantoid-basierten molekularen Systeme durch Dotierung der Moleküle mit Bor und Stickstoff selektiv abstimmen.

Die Dotierung mit Stickstoff führt zu einer Vergrößerung eines Transmissionsspeaks sehr nahe am Fermi-Niveau, was zu einer höheren molekularen Leitfähigkeit führt. Eine Erhöhung der Diamantoidgröße führt zu einer leichten Abnahme der Leitungsleitfähigkeit bei keiner Vorspannung. Eine solche Abnahme wurde auch beobachtet, wenn die Carbenmoleküle zur Verbindung des Diamantoids an den Nano-Spaltflächen verwendet wurden. Vorspannungsabhängige Transportberechnungen zeigten, dass Dotierungen zu einem höheren Gleichrichtungsverhältnis bei sehr kleinen angelegten Vorspannungen führt. Dieses Verhalten ist das Ergebnis der Energieverschiebung der HOMO-Peaks gegenüber denen bei keiner Vorspannung. Die gleichrichtende Wirkung in N-dotierten Diamantoiden hängt mit der Asymmetrie in der Struktur zusammen, wenn diese dotiert wird. Bei der B- und B-N-Dotierung kommt es zu einer ähnlichen Asymmetrie durch Dotierung, woraus wir folgern können, dass auch für diese Fälle ein ähnliches Gleichrichtungsverhältnis beobachtet werden kann.

Contents

Abbreviations	xv
Nomenclature	xvii
1 Introduction	1
1.1 Structure and nomenclature	1
2 Computational and theoretical background	7
2.1 Electronic structure and DFT	7
2.1.1 The many-body problem	8
2.1.2 Hohenberg-Kohn theorem	9
2.1.3 Kohn-Sham theory	10
2.2 Solving the Kohn-Sham equations	13
2.2.1 Plane wave method	15
2.2.2 Localized atomic orbital method	15
2.3 Electronic transport	16
2.3.1 Molecular junction	16
2.4 Time-dependent density functional theory	19
2.4.1 Runge-Gross formalism	19
2.5 Computational tools	20
3 Modified diamondoids: doping and functionalization	22
3.1 Introduction	22
3.2 Electronic properties of diamondoids	24
3.2.1 Adamantane	26
3.2.2 Isomers of tetramantane	32
3.2.3 Band gap tuning	35
3.3 Optical properties of lower diamondoids	37
3.3.1 Adamantane	38
3.3.2 Diamantane	43
3.3.3 Optical band gap	47
3.4 Conclusions	50
4 Self-assembled monolayers	51
4.1 NHC mediated diamondoids	51
4.2 Diamondoid mediated SAMs	52
4.2.1 Structural analysis	53
4.2.2 Adsorption Energies	55

4.2.3	Isolated NHC-functionalized adamantane	57
4.2.4	Work function	60
4.2.5	Surface morphology	63
4.3	Discussion	66
5	Diamondoid-based molecular junction	68
5.1	Molecular junction	68
5.2	Diamondoid within a gold nano gap	72
5.2.1	Structural Characteristics	73
5.2.2	Electronic properties	74
5.2.3	Electronic transport	75
5.3	Current-Voltage Characteristics	81
5.4	Discussion	84
6	Conclusions and outlook	85
	Appendix	88
A	Promoting assembly of carbon onions	88
A.1	Introduction	88
A.2	Methodology	90
A.3	Results and discussions	92
A.3.1	Introducing vacancies	92
A.3.2	Introducing dopants	95
A.3.3	Electronic properties	98
A.4	Summary and conclusions	102
	List of Tables	105
	List of Figures	107
	Bibliography	111

Abbreviations

cam-B3LYP coulomb-attenuating method-Becke 3-parameter Lee Yang Parr

CI Configuration Interaction

CNT Carbon Nanotube

C/N Carbon Nitrogen ratio

CVD Chemical Vapour Deposition

DFT Density Functional Theory

DNA Deoxyribonucleic Acid

DOS Density Of States

DZP Double Zeta Polarization

EDOS Electronic Density Of States

EFW Eigenchannel Wavefunction

FEDs Field Emission Displays

GAMESS General Atomic and Molecular Electronic Structure System

GGA Generalized Gradient Approximation

HF Hartree-Fock

HK Hohenberg-Kohn

HOMO Highest Occupied Molecular Orbital

LAMMPS Large-scale Atomic/Molecular Massively Parallel Simulator

LCAO Linear Combination of Atomic Orbitals

LDA Local Density Approximation

LUMO Lowest Unoccupied Molecular orbital

MD Molecular Dynamics

MGGA Meta Generalized Gradient Approximation
NEGF Non-Equilibrium Green's Function
NHC N-Heterocyclic Carbene
OPW Orthogonalised Plane Wave
PAW Projector Augmented Wave
PBE-GGA Perdew Burke Ernzerhof-Generalized Gradient Approximation
PDOS Partial Density Of States
PW91 Perdew Wang 91
RR Rectification Ratio
SCF Self-Consistent Field
SAM Self-Assembled Monolayer
SIESTA Spanish Initiative for Electronic Simulations for Thousands of Atoms
STM Simulated Tunnelling Microscopy
S-matrix Scattering matrix
SZP Single Zeta Polarization
TDDFT Time-Dependent Density Functional Theory
TDOS Total Density Of States
UV Ultra Violet
VDW Van Der Waals
VASP Vienna Ab-initio Simulation Package
XC Exchange-Correlation
XPS X-ray Photoelectron Spectroscopy

Nomenclature

$\{t\}$	Time
$\{\alpha'\}$	Polarization vector of the electromagnetic wave
$\{\alpha\}$	The exchange mixing parameter
$\{\mathbf{r}\}$	Position vector
$\{\epsilon_0\}$	Dielectric Constant
$\{\epsilon_{hom}^C\}$	Correlation electron density
$\{\epsilon_{hom}^X\}$	Exchange electron density
$\{\Gamma_L\}$	Energy level broadening of the left electrode
$\{\Gamma_R\}$	Energy level broadening of the right electrode
$\{\hat{H}\}$	Hamiltonian operator
$\{\hbar\}$	Planck Constant
$\{\mu_0\}$	Surface dipole moment per area
$\{\mu_L\}$	Chemical potential of left electrode
$\{\mu_L\}$	Chemical potential with respect to the left electrode
$\{\mu_R\}$	Chemical potential of right electrode
$\{\mu_R\}$	Chemical potential with respect to the right electrode
$\{\mu_z\}$	Surface normal dipole moment per area
$\{\nu_1(\mathbf{r}, t)\}$	Time-dependent potential
$\{\nu_{ext}(\mathbf{r}, t)\}$	Time-dependent external potential
$\{\omega\}$	Frequency of the electromagnetic wave
$\{\Phi\}$	Work function
$\{\Psi(\mathbf{r}, t)\}$	Total wave function of a many-body system

$\{\rho(\mathbf{r})\}$	Ground state electron density
$\{\rho(\mathbf{r}, t)\}$	Time-dependent external density
$\{\rho^\downarrow\}$	Densities of electrons with down spins
$\{\rho^\uparrow\}$	Densities of electrons with up spins
$\{c(t)\}$	Time-dependent constant term
$\{e\}$	Charge of an electron
$\{f(t)\}$	Envelope function the controls the electromagnetic wave
$\{f_{L/R}\}$	Fermi-Dirac distribution of the left and the right electrode
$\{G\}$	Reciprocal lattice vector
$\{G^a\}$	Advanced Green's function
$\{G^r\}$	Retarded Green's function
$\{H_{eff}\}$	Effective Hamiltonian
$\{i\}$	Imaginary unit
$\{L_m\}$	Mean free path length
$\{L_\phi\}$	Phase relaxation length
$\{m_e\}$	Mass of electron
$\{M_I\}$	Mass of nucleus
$\{r_c\}$	Cutoff distance
$\{T\}$	Kinetic energy
$\{V\}$	Potential energy
$\{V_b\}$	Bias voltage
$\{V_{ext}(\mathbf{r})\}$	External potential
$\{Z_I\}$	Atomic number of the nucleus

Chapter 1

Introduction

Diamondoids are a series of perfectly defined, hydrogen-terminated nano-diamonds [1–3]. These diamondoids are available in various shapes and sizes that can be extracted and isolated from petroleum products [4] and can be organically synthesized [2] or nucleated from energetic species [3]. These nano-diamondoids constitute a number of diamond cages which forms a diamondoid family starting from adamantane ($C_{10}H_{16}$) and then diamantane ($C_{14}H_{20}$) and so on. A self-assembly of diamondoids encapsulated inside carbon nanotubes has also been investigated in the past [5–7]. In view of biotechnological applications, efficient site-specific incorporation of diamondoids on DNA [8], as well as the use of diamondoids as biosensors for reading-out DNA molecules [9]. Diamondoids possess technologically interesting properties such as negative electron affinity [10, 11] and are also used in CVD diamond growth [12]. The chemical functionalization of diamondoids [10, 13, 14] has paved the way for new diamondoid devices and various nanotechnological applications [15]. Doping and functionalization have opened various new possibilities for tailoring the properties of diamondoids. Additionally, the exact understanding of the structure of each diamondoid yields unique possibilities, such as investigating shape and size effects in nanocrystals and the influence of single or multiple doping with various impurity atoms. Diamondoids doped with boron and nitrogen atoms can be interlinked to form functional nanostructures in carbon nanotubes [15], while lower diamondoids and their derivatives have also been theoretically found to self-assemble into larger interlinked nanostructures [16]. In view of biotechnological applications, efficient site-specific incorporation of diamondoids on DNA are possible [8], as well as the use of diamondoids as biosensors for reading-out DNA molecules [9].

1.1 Structure and nomenclature

Diamondoids are found to form molecular van-der-Waals crystals at room temperature and possess a large band gap [1–3, 17]. As a result, these crystals are colorless and visually appear white due to the scattering of light. These molecules have a high melting point around 200 °C and they also sublime at room temperature [17]. The partial pressure of the diamondoids depends

on their molecular weight and the shape of the diamondoid. The shape of the diamondoid depends on the stacking order of the smallest molecular unit which is known as adamantane. This order of stacking determines the strength of these diamondoids. In Fig. 1.1, we can see the atomic structures of these diamondoids starting from the smallest unit adamantane until heptamantane. The diamondoid family is classified by the increasing number of crystal cages. Adamantane is the smallest unit of the diamondoid family. It is composed of a greek numeric prefix which resembles the number of cages by which a diamondoid is constructed. Similarly, diamantane is the second member of the diamondoid family which consist of two adamantane cages, triamantane comprises of three and the series goes on. For the first three members of the diamondoid family namely; adamantane, diamantane, and triamantane, no isomers exist. However, as we go up increasing the number of adamantane subunits, different isomers can be found for the same size of diamondoid starting from tetramantane, which has four isomers.

In Fig. 1.2, all the diamondoid structures up to triamantane and isomers of tetramantane structures are shown. Tetramantane possesses four structural isomers. Similarly, for pentamantane there are ten different isomers and so on. To differentiate between various isomers, Balaban and von Schleyer introduced the nomenclature system that describes the structural arrangement of the cages. The name of the diamondoid is usually preceded by a numeric prefix in brackets. These brackets indicate the direction of the addition cages along various axes of a tetrahedron [1]. This concept is schematically shown in Fig. 1.2. Lower diamondoids from adamantane to tetramantane are built on n -fused adamantane units which is followed by a general formula $[C_{4n+6} H_{4n+12}]$, where $n = 1-4$. However, several isomeric forms for $n > 3$ exist, and some higher diamondoids of high symmetry do not necessarily follow this formula. For the diamondoids like the diamantane and triamantane which possess explicit names, the full notation such as the [1] diamantane and [12] triamantane are not used. There are three different ways to attach a fourth diamond cage to a triamantane molecule which comprises a tetramantanes. These are shown in the second row of Fig. 1.2. These isomers are classified as anti-, M skew-, P skew-, iso- tetramantane and named as [121] tetramantane, M[123] tetramantane, P[123] tetramantane and [1(2)3] tetramantane. Panel (d) of Fig. 1.2 depicts the sketches of the addition of a cage parallel to the first extension, which generates [121] tetramantane. In Fig. 1.2(e), the additional cage is attached in a different direction, therefore the resulting diamondoid is labelled as [123] tetramantane. In Fig. 1.2(f), the fourth cage diverges off the main axis. Such a diversion is indicated in the Balaban-Schleyer [1] nomenclature using round brackets as [1(2)3] tetramantane. For larger diamondoids, another adamantane sub-unit is added for each additional cage.

These nanometer-sized cages can also attach on metallic surfaces through a thiol group [18,19] to form self-assembled monolayers (SAMs) with a negative electron affinity and a strong monochromatic emission [10,20] as shown in Fig.

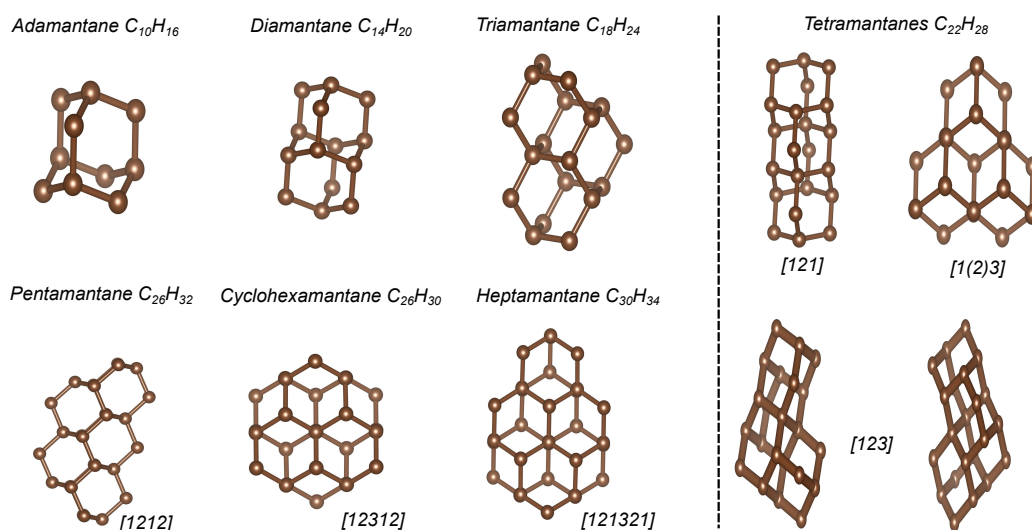


Figure 1.1: Diamondoids of different sizes and shapes are shown. The numerals in the brackets indicate the structural arrangement of the cages in accordance with the Balaban-Schleyer nomenclature.

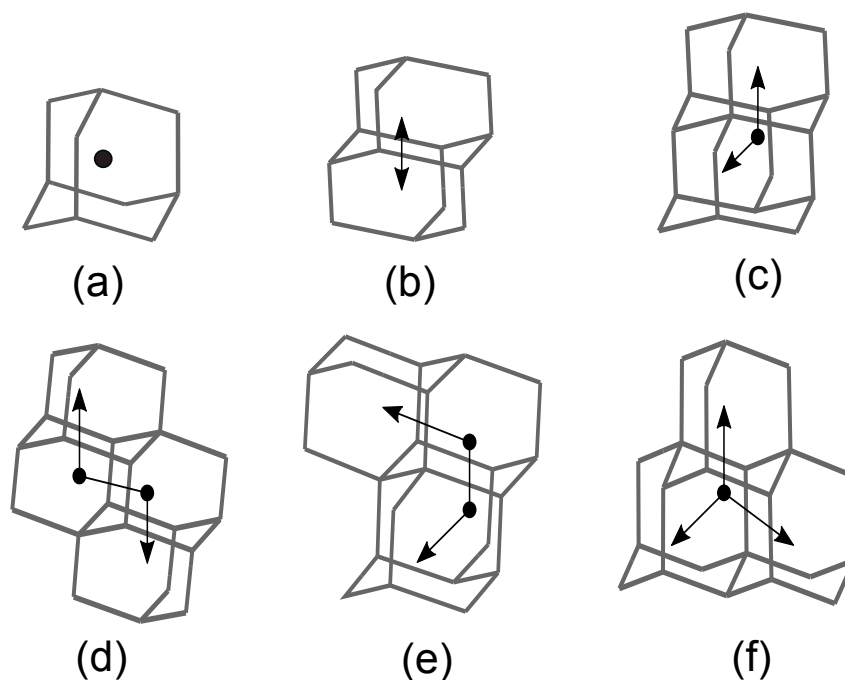


Figure 1.2: When the diamond cages are fused along the tetragonal axes of a bulk diamond, a diamondoid is formed. Three different tetramantane (d)-(f) can be formed based on the structure of triamantane (c). These are classified as (d) [121] tetramantane, (e) [123] tetramantane and (f) [1(2)3] tetramantane with respect to the site of the fourth cage. The black arrows represent the direction of the addition of the cages. [1]

1.3. These properties make diamondoids very promising for electronics applications. In the past, thiol-based SAMs on metal surfaces have led to significant applications in the field of surface emission, sensing, electrochemistry, drug delivery, and microelectronics [21–25]. However, thermal instability of these thiol-based SAMs on gold in harsh environmental conditions has been a huge hindrance in using them for industrial purposes [26–30]. Thiol-based SAMs are found to be stable only when stored in an ultra high vacuum in the absence of light but tend to degrade after few weeks at room temperature [31–33]. The experimental shortcomings in the preparation of SAM's usually include an unknown surface reconstruction, undefined particle shape and interactions of the sample with its environment. The present vacuum phase investigations on diamondoids allow us to get rid of these experimental hindrances and produce data of atomically defined neutral particles.

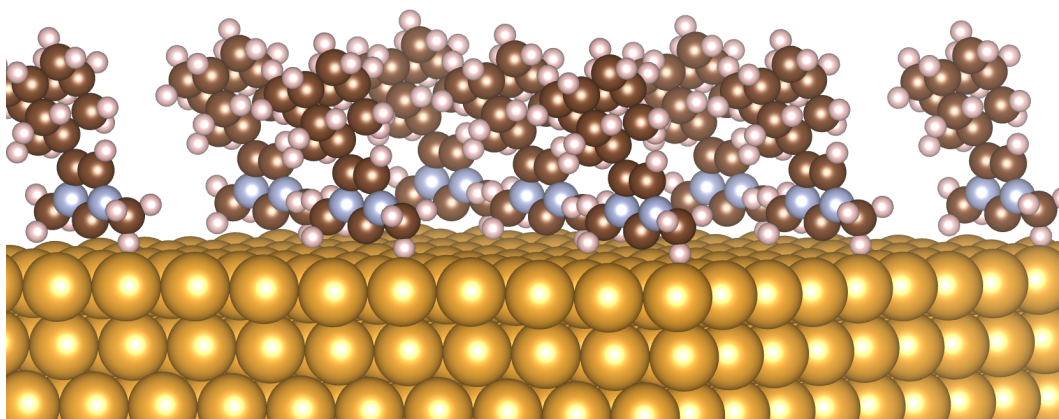


Figure 1.3: Schematic illustration of a self-assembled monolayer of [121]-tetramantane-6-thiol on a noble metal surface.

The goal of the present study is the theoretical investigation of the influence of different variables that define the electronic, transport, and optical properties of diamondoids. We implemented a bottom-up approach to studying the properties of diamondoids, the influence of structural modification (doping and functionalization) on their electronic and optical properties. The fundamental aim of our research is to computationally develop modified diamondoid-based complexes and transition metals structures in view of their nanotechnological applications. We examined their stability, metal-carbon, and metal-thiol electronic properties keeping in mind the long-term applications as the growth of diamond-like films over various metal surfaces. Our investigation is based upon various parameters such as the size of diamondoid, its shape and the chemical alteration that we induce by doping and functionalization. Ideal or unmodified diamondoids of different sizes and shapes are examined to determine the impact of size and shape on the electronic and optical properties. Diamon-

doids with functional groups like thiol, carbene, and diamondoids doped with various atoms are studied to learn about the influence of different kinds of chemical modifications on transport properties of diamondoid-based molecular junctions. Quantum chemical calculations under the framework of Density Functional Theory DFT are used to help interpret and analyze the results.

The content of this thesis is the following:

In Chapter 2, the theoretical background and methodology used in this thesis is explained.

In Chapter 3, we study the stability, structural alterations as well as the effect on the electronic and optical properties of the modified (doped, single-, and double-functionalized) diamondoids with respect to the properties of ideal unmodified diamondoids. The electronic and optical properties in all cases are probed through the frontier orbitals, namely the highest occupied (HOMO) and lowest unoccupied (LUMO) molecular orbitals, as well as the electronic and optical band-gap. We also compare the structural modification, localization, and delocalization of orbitals and also look at the excited state geometry and make comparisons to the absorption spectra.

In Chapter 4, we aim to study the structural and electronic properties of carbene-functionalized diamondoid monolayers on metal surfaces. For the latter, we consider gold, silver, and platinum surfaces. We study the structural and electronic properties of the diamondoid SAMs on these surfaces, their morphology, and work function in view of their nanotechnological applications as potential electron emitters and sensors.

In Chapter 5, we study the influence of the diamondoid size, the type of dopants, and the diamondoid functionalization on the properties of molecular devices, that is a metallic break-junction in which a diamondoid is inserted and bonded through the functionalization group on the metallic surfaces. For the electrodes, two Au(111) surfaces are taken. For tetramantane, one of the isomers, the [121] tetramantane molecule was chosen. Different dopants and functional groups were chosen to separately dope and functionalize the diamondoids.

In Chapter 6, we summarize and discuss the outcomes of this work and provide an outlook on the possible future work.

Finally, in Appendix A, we probe the binding possibilities of the smallest multi-shelled concentric fullerenes, known as *carbon onions*, which is also another type of carbon-cages. We focus on the binding behavior of adjacent carbon onions and promote their binding through the addition of vacancies, as well as through doping with boron and nitrogen atoms.

Publications

The following publications are related to this thesis:

1. **Adhikari B.**, Uhlig F., Meng S., and Fyta M.– "Optical properties of modified diamondoids: influence of carbene" (*in preparation*)
2. **Adhikari B.**, Sivaraman G., Fyta M.– "Diamondoid-based molecular junctions: a computational study" *Nanotechnology* **27**, 485207, 2016
3. Natterer A., **Adhikari B.**, Fyta M.– "Complexes of carbene-functionalized diamondoids and metal atoms: Electronic properties" *J. Organomet. Chem*, pp. 8-15, 2016
4. **Adhikari B.**, Meng S., Fyta M.–"Carbene-mediated self-assembly of diamondoids on metal surfaces" *Nanoscale* **8**, 8966 - 8975, 2016
5. **Adhikari B.**, Fyta M.– "Towards double-functionalized small diamondoids: selective electronic band-gap tuning" *Nanotechnology* **26**, 035701, 2015
6. **Adhikari B.**, Muthuraman B., Mathioudakis C., Fyta M. –"Promoting assembly of carbon onions: an atomistics approach" *Phys. Status Solidi A* **211**, 277-287, 2014

Chapter 2

Computational and theoretical background

In this chapter, a brief introduction is given into the theoretical background of the electronic structure calculations and the theoretical tools that are used in this work for the interpretation of the results. In section 2.1 the basics of quantum chemical electronic structure computations along with density functional theory (DFT) are introduced. Next, we discuss the many body problems, basics of density functional theory, Born-Oppenheimer approximation, and various methods used in solving the Kohn-Sham formalism. In section 2.3, we discuss the methods implemented in the modelling of a molecular junction for the calculation of transmission spectra. Finally, in the section 2.4, we describe the computational background behind the time-dependent density functional theory calculations.

2.1 Electronic structure and DFT

Electronic structure theory has evolved a great deal in the recent past leading to the characterization of materials into insulators, semiconductors, and metals. Several methods have been proposed till date; namely the Hartree-Fock (HF) method [34], plane wave (PAW) method [35], orthogonalized plane wave (OPW) method [36], and the pseudopotential method [37] etc. Electronic structure calculations made rapid developments after the density functional theory (DFT) was introduced in 1960's. DFT is mainly based on the Hohenberg-Kohn [38] theorem which states that all the properties of a many-body system can be completely determined by the ground state charge density. Since the 1990's, electronic structure calculations based on density functional theory became more and more popular in the field of quantum calculations. Density functional theory has been by far the most widely used method to investigate the electronic properties of materials and solids. It is also referred as an *ab initio* method, because of its simplicity which allows to understand the properties of a very complex system just by providing some basic structural information as an input parameter which is usually the spatial coordinates.

Depending upon the system and the properties we would like to investigate, it has been proven time and again to be an accurate alternative to other computationally inefficient methods. On the basis of results obtained from DFT one can also make predictions of experimental properties and help further in designing and synthesizing interesting and novel materials. DFT describes the properties of condensed matter systems in an accurate manner ranging from standard bulk metals to molecules, proteins, surfaces, and interfaces. The sole idea of DFT is to describe a many-body interacting system in terms of its particle density instead of the many-body wavefunction. The efficiency of DFT is because of the fact that it reduces the $3N$ degrees of freedom of a many-body system to merely three spatial coordinates. Its basis is the well known as the Hohenberg-Kohn theorem [38], which is based on the formalism that all the properties of a system can be considered to be unique functionals of its ground state density.

The Born-Oppenheimer approximation [39] and Kohn-Sham formalism [40] combine to produce DFT calculations provided that the approximations for the exchange-correlation (XC) potential are accurate enough. However, they cannot be accurate but a good approximation. The XC potential describes two basic properties of the electrons which are namely: exchange term and the correlation term. These two terms describe the effects of the Pauli principle and the Coulomb potential of a particular system. Some of the well known approximations that have been widely used are: the local density approximation (LDA) [38], generalized gradient approximation (GGA) [41], meta generalized gradient approximation (metaGGA) [42], hybrid functionals [43], nonlocal functionals [44] etc.

LDA is one the commonly used approximations. It substitutes the XC energy density of an inhomogeneous system by a homogeneous electron gas at the local density. Generalized gradient approximation (GGA) [45] is another popularly used approximation which is a generalization of the LDA that includes also the contributions from electron density gradient. With these approximations, the results of DFT calculations for various systems usually agree quite well with the experimental data. Also, the computational efficiency with DFT has been relatively high compared to solving the many-electron wavefunction, such as the Hartree-Fock method [34, 46]. However, various shortcomings of DFT include inaccuracy in the band gap of semiconductors. It also fails to accurately describe the charge transfer [47], transition states [48], and shows inconsistencies when it comes to strongly-correlated systems because of the errors in the standard DFT approximations [49, 50].

2.1.1 The many-body problem

The basic aim of all the electronic structure methods is to solve the Schrödinger equation. The equation can be given in a general time-dependent form as follows:

$$i\hbar \frac{\partial}{\partial t} \Psi(\mathbf{r}, t) = \hat{H} \Psi(\mathbf{r}, t) \quad (2.1)$$

where $\Psi(\mathbf{r}, t)$ is the total wavefunction and \hat{H} is the Hamiltonian operator, \mathbf{r} , t are the positions and time, respectively. A general description of the Hamiltonian of a many-body system can be written as:

$$H = -\frac{\hbar^2}{2M_I} \sum_I \nabla_R^2 - \frac{\hbar^2}{2m_e} \sum_i^N \nabla_r^2 + \frac{1}{2} \sum_{I \neq J} \frac{Z_I Z_J e^2}{|\mathbf{R}_I - \mathbf{R}_J|^2} \quad (2.2)$$

$$+ \frac{e^2}{2} \sum_{i \neq j} \frac{1}{|\mathbf{r}_i - \mathbf{r}_j|^2} - e^2 Z_I \sum_{I,i} \frac{1}{|\mathbf{R}_I - \mathbf{r}_i|} \quad (2.3)$$

where the first and second terms in the above equation is the kinetic energy (KE) of the nuclei and of the electrons, the third term is the potential energy (PE) of the nucleus-nucleus Coulomb interaction, the fourth term is the PE of electron-electron Coulomb interaction and the last term is the PE of the nucleus-electron Coulomb interaction. The indices $\{I\}$, $\{J\}$ and $\{i\}$ and $\{j\}$ run over the electrons and nuclei respectively, $\{\mathbf{r}_i\}$ and $\{m_e\}$ represent the positions and the masses of electrons, $\{\mathbf{R}_I\}$ and $\{M_I\}$ are positions and masses of the nuclei and $\{Z_I\}$ is the atomic number of the nucleus and $\{e\}$ is the electronic charge. The time-independent Schrödinger equation can be written as:

$$H \Psi(\mathbf{R}_I, \mathbf{r}_i) = E \Psi(\mathbf{R}_I, \mathbf{r}_i) \quad (2.4)$$

where $\{\Psi(\mathbf{R}_I, \mathbf{r}_i)\}$ is the total wavefunction of the system. In order to simplify the solution scheme of Schrödinger equation, Born-Oppenheimer approximation was introduced by Born and Oppenheimer [39]. The nuclei are heavier and move much slower than the electrons. When we consider the movement of electrons, we consider that the positions of nuclei are fixed, the total wavefunction $\{\Psi\}$ only depends on the electronic degrees of freedom. This implies that the potential and the kinetic energy of the nuclei are constant. Taking these approximations into consideration, we can simplify 2.2 as the following:

$$H = -\frac{\hbar^2}{2m_e} \sum_i^N \nabla_r^2 + \frac{e^2}{2} \sum_{i \neq j} \frac{1}{|\mathbf{r}_i - \mathbf{r}_j|^2} + \sum_i V_{ext}(\mathbf{r}) \quad (2.5)$$

In equation 2.5, the external potential $\sum_i V_{ext}(\mathbf{r})$ can be formulated as:

$$\sum_i V_{ext}(\mathbf{r}) = - \sum_I^i \frac{e^2 Z_I}{|\mathbf{R}_I - \mathbf{r}_i|} \quad (2.6)$$

2.1.2 Hohenberg-Kohn theorem

DFT is based upon is based upon two variational Hohenberg-Kohn (HK) theorems [40] as the following;

- The first theorem states that for the ground state electron density $\{\rho(\mathbf{r})\}$, an external potential $\{V_{ext}(\mathbf{r})\}$ determines the external potential $\{V_{ext}(\mathbf{r})\}$. That is, two different potentials can generate different ground state densities. That also means the states including ground and excited states of the many-body wavefunctions can be calculated and the ground state particle density can be used to determine all the properties of the system.
- The second theorem states that the universal functional $\{F[\rho(\mathbf{r})]\}$ of the density is independent of the external potential $\{V_{ext}(\mathbf{r})\}$ acting on the interacting system in which the non-interacting particles move. The minimum of the energy functional $\{E[\rho(\mathbf{r})] = \int \rho(\mathbf{r})V_{ext}(\mathbf{r})dr + F[\rho(\mathbf{r})]\}$ is the exact ground state energy of the system and the exact ground state density $\{\rho_0(\mathbf{r})\}$ minimizes this functional. Thus, the ground state energy and density are determined by the functional $\{E[\rho(\mathbf{r})]\}$.

2.1.3 Kohn-Sham theory

The Kohn and Sham (KS) [40] theory is merely an extension of the Thomas-Fermi (TF) model [51]. In the Thomas-Fermi method, the electron density $\rho(\mathbf{r})$ is the basic variable instead of the wavefunction. As a result, the TF theory fails to describe bonding between atoms and the formation of molecules and solids. In contrast, KS method obtains the ground-state kinetic energy from a non-interacting system. A non-interacting system of reference can also be called as an auxiliary particle system or the fictitious non-interacting system. The auxiliary Hamiltonian $\{\hat{H}_S\}$ for a non-interacting particle system can be written as:

$$\hat{H}_S = T + V_S \quad (2.7)$$

where $\{V_S(\mathbf{r})\}$ is the effective Kohn-Sham single-particle potential where the interacting electrons are treated as non-interacting electrons in presence of an effective potential. Next, we can write the density functional as follows:

$$E_s[\rho] = T_s[\rho] + \int V_s(\mathbf{r})\rho(\mathbf{r})d\mathbf{r} \quad (2.8)$$

where $\rho(\mathbf{r})$ and T_s is the KE of the non-interacting electron gas of the system. Then the energy functional $\{E[\rho(\mathbf{r})]\}$ can be rewritten as:

$$E[\rho(\mathbf{r})] = T_s[\rho(\mathbf{r})] + E_H[\rho(\mathbf{r})] + E_{XC}[\rho(\mathbf{r})] \quad (2.9)$$

where for the kinetic energy term $\{T_s[\rho(\mathbf{r})]\}$ is given by:

$$T_s[\rho(\mathbf{r})] = -\frac{1}{2} \sum_{i=1}^N \int \psi_i^*(r)\nabla^2\psi_i(\mathbf{r})d\mathbf{r} \quad (2.10)$$

and $\{E_H[\rho(\mathbf{r})]\}$ is the electrostatic Hartree energy of the electrons which can be formulated as:

$$E_H[\rho(\mathbf{r})] = \frac{1}{2} \int \int \frac{\rho(\mathbf{r})\rho(\mathbf{r}')}{|\mathbf{r} - \mathbf{r}'|} d\mathbf{r}d\mathbf{r}' + \int V_{ext}(\mathbf{r})\rho(\mathbf{r})d\mathbf{r} \quad (2.11)$$

and lastly the exchange-correlation term $\{E_{XC}[\rho(\mathbf{r})]\}$ can be written as:

$$E_{XC}[\rho(\mathbf{r})] = F[\rho(\mathbf{r})] - T_s[\rho(\mathbf{r})] + E_H[\rho(\mathbf{r})] \quad (2.12)$$

Next, the ground state energy of a many-body system can be obtained by minimizing the energy functional $\{E[\rho(\mathbf{r})]\}$ through a variational approach.

Exchange-correlation functional

The Kohn-Sham theory is still an approximation because of the unknown XC energy functional $\{E_{XC}[\rho(\mathbf{r})]\}$ which can be defined as:

$$E_{XC}[\rho(\mathbf{r})] = T[\rho(\mathbf{r})] - T_s[\rho(\mathbf{r})] + E_{elec}[\rho(\mathbf{r})] - E_H[\rho(\mathbf{r})] \quad (2.13)$$

where $\{T[\rho(\mathbf{r})]\}$ and $\{E_{elec}[\rho(\mathbf{r})]\}$ are the exact kinetic and electron-electron interaction energies. The XC energy in an integral over the whole space with XC energy at $\{\mathbf{r}\}$ is considered to be the same as in a homogeneous electron gas of that electron density at the point $\{\mathbf{r}\}$. The total exchange-correlation functional $\{E_{XC}[\rho(\mathbf{r})]\}$ can be written as:

$$E_{LDA}^{XC}[\rho(\mathbf{r})] = \int \rho(\mathbf{r})\epsilon_{hom}^{XC}(\rho(\mathbf{r}))d\mathbf{r} = \int \rho(\mathbf{r}) \left[\epsilon_{hom}^X(\rho(\mathbf{r})) + \epsilon_{hom}^C(\rho(\mathbf{r})) \right] d\mathbf{r} \quad (2.14)$$

$$= E_{LDA}^X[\rho(\mathbf{r})] + E_{LDA}^C[\rho(\mathbf{r})] \quad (2.15)$$

Similarly, for a spin polarized system, it can be written in such a way:

$$E_{LSDA}^{XC}[\rho^\uparrow(\mathbf{r}), \rho^\downarrow(\mathbf{r})] = \int \rho(\mathbf{r})\epsilon_{hom}^{XC}(\rho^\uparrow(\mathbf{r}), \rho^\downarrow(\mathbf{r}))d\mathbf{r} \quad (2.16)$$

where $\{\rho(\mathbf{r})\}$ is the total electronic density at $\{\mathbf{r}\}$, $\{hom\}$ denotes the homogeneous electron gas and $\{\rho^\uparrow\}$, $\{\rho^\downarrow\}$ are the densities of electrons with up and down spins respectively. $\epsilon_{hom}^{XC}(\rho(\mathbf{r}))$ is the function of density which is further expanded into the exchange density $\epsilon_{hom}^X(\rho(\mathbf{r}))$ and the correlation density $\epsilon_{hom}^C(\rho(\mathbf{r}))$. LDA is the cheapest form of approximations in terms of computational time but it tends to underestimate the atomic ground state energies and ionization energies while overestimating binding energies. It also makes large errors in predicting the energy band gaps of some semiconductors. Its success and limitations lead to approximations of the XC energy functional

beyond the LDA, through the addition of gradient corrections to incorporate longer range gradient effects (GGA). The generalized gradient approximation (GGA) is another form of approximation used in electronic structure calculations which are simply an improvement to LDA. It includes density gradient corrections and the magnitude of the gradient of the electron density. A general form of GGA for a spin polarized case can be written as:

$$E_{GGA}^{XC}[\rho^\uparrow(\mathbf{r}), \rho_\downarrow(\mathbf{r})] = \int \rho(\mathbf{r}) \epsilon^{XC}(\rho^\uparrow(\mathbf{r}), \rho_\downarrow(\mathbf{r}), |\nabla\rho^\uparrow|, |\nabla\rho^\downarrow|) d\mathbf{r} \quad (2.17)$$

GGA has higher complexity than LDA but can lead to better results but is not always as efficient as LDA. GGA can lead to bad results where it might overestimate the lattice constants of ionic crystals. LDA performs better for covalently bonded systems and GGA for magnetic and metallic systems. However, both GGA and LDA might fail to reproduce accurate results in the case of transitions and rare earth compounds. Meta generalized gradient approximation (MGGA) [42] go beyond the regular GGAs to include additional semi-local information beyond the first-order density gradient contained in the GGA, such as higher order density gradients, or more popular is the inclusion of the kinetic energy density $\{\tau(\mathbf{r})\}$ which involves derivatives of the occupied Kohn-Sham orbitals. The hybrid functionals [43] combine the exact (Hartree-Fock) exchange with conventional GGAs, the general form as:

$$E_{XC}^{hybrid} = \alpha(E_X^{HF} - E_X^{GGA}) + E_{XC}^{GGA} \quad (2.18)$$

where $\{\alpha\}$ is the exchange mixing parameter, $\{X^{HF}\}$ is the Hartree-Fock exchange. There are other approximations such as the fully nonlocal average density approximation [44] and weighted density approximation which uses an exact density functional and directly models the exchange-correlation hole using the analytic functions. However, these functionals are not commonly used because they are computationally expensive.

Pseudopotentials

The pseudopotentials [37] are an approximation where we generate a universal pseudopotential so that the chemical properties of a particular system is determined entirely by the outermost valence electrons keeping the core electrons chemically inert. This simplification is connected with a corresponding replacement of the true valence wavefunctions with pseudo-wavefunctions that lead to a major reduction in the number of wavefunctions which have to be handled as shown in the sketch of Fig. 2.1. In the process, the core electrons are ignored and the core states are frozen. Most widely used pseudopotentials nowadays include norm-conserving pseudopotentials [52] and ultrasoft pseudopotentials [53]. There are three important aspects in pseudopotential theory.

- The pseudopotential should be consistent with the XC functionals and eigenvalues of an isolated atom should be accurately reproduced by the pseudopotential.

- The wavefunctions or also called the pseudo-wavefunctions should coincide with the valence wavefunctions.
- The pseudo-wavefunction charge within the core should be equal to the corresponding charge of the valence wavefunction, which is also called as norm-conserving pseudopotentials.

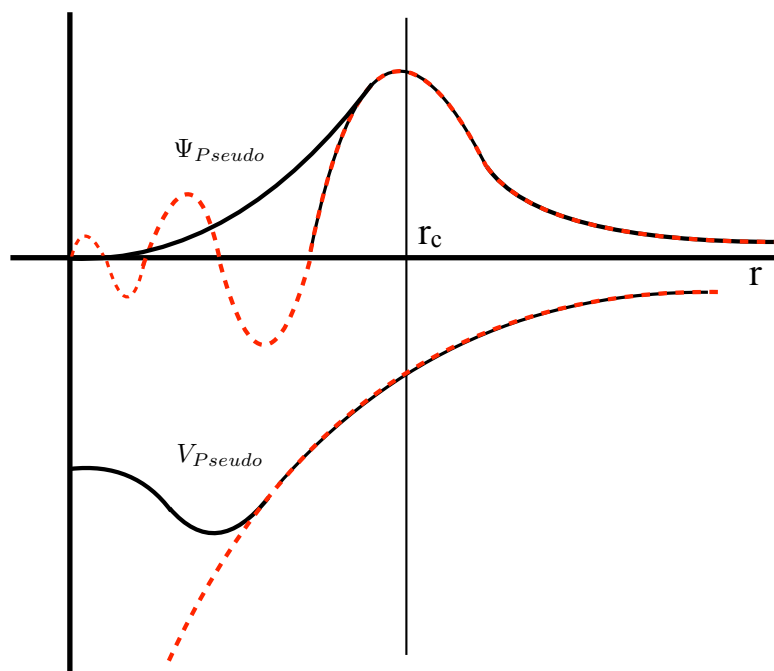


Figure 2.1: Comparison of a pseudo wavefunction (Ψ_{pseudo}) and the pseudo-potential (V_{pseudo}) is presented. The real and the pseudo wavefunction and potentials should match with each other certain cutoff radius r_c .

The equation for the pseudopotential that considers only the valence electrons is given by:

$$\left[-\frac{\hbar^2}{2m_e} \nabla^2 + V_{eff}^{pseudo} \right] \Psi_i^{pseudo} = \epsilon_i^{pseudo} \Psi_i^{pseudo} \quad (2.19)$$

here, the effective potential $\{V_{eff}\}$ and the wavefunction $\{\Psi_i\}$ is replaced by the pseudopotential $\{V_{eff}^{pseudo}\}$ and $\{\Psi_i^{pseudo}\}$. Since the core states are frozen and core electrons are ignored the valence electrons are represented by pseudo-wavefunctions which have fewer nodes resulting in lesser computation time.

2.2 Solving the Kohn-Sham equations

Solving the Kohn-Sham equations leads to the exact density and ground state energy of a system under investigation. Since the Kohn-Sham effective potential $\{V_{KS}\}$ and the electron density $\{\rho(\mathbf{r})\}$ are closely related to each

other, the equations are solved with the self-consistent field method (SCF). In the SCF method, the calculations are done iteratively where an approximate Hamiltonian is first chosen, then the Schrödinger equation is solved to obtain a more accurate set of orbitals until the results converge. In other words, this process generally starts with an initial guess of the electron density, which is usually a superposition of the atomic electron densities of the system. After that the effective Kohn-Sham potential $\{V_{KS}\}$ is calculated and the Kohn-Sham equation is solved with eigenvalues and wave functions obtained from the iterations. Next, a new electron density is calculated from the wavefunctions. After that, the self-consistency condition is analyzed, which depends on the convergence criteria. This criterion could be the change of total energy or total density or the total force acting on atoms which are usually a threshold for the successful convergence. If the self-consistency criteria are not achieved, the mixing of the electron density with electron density from previous iterations takes place to obtain a new electron density. Hence, a new iteration will start with the new electron density. This process is continued until the self-consistency criteria is reached. After the system is fully relaxed at the ground state, other quantities can also be calculated including total forces, stress tensors, eigenvalues, orbitals, the density of states, band structure, etc. Some of the methods that are used in solving the Kohn-Sham equations are discussed below. The self-consistency algorithm for solving the density functional theory is depicted in Fig. 2.2.

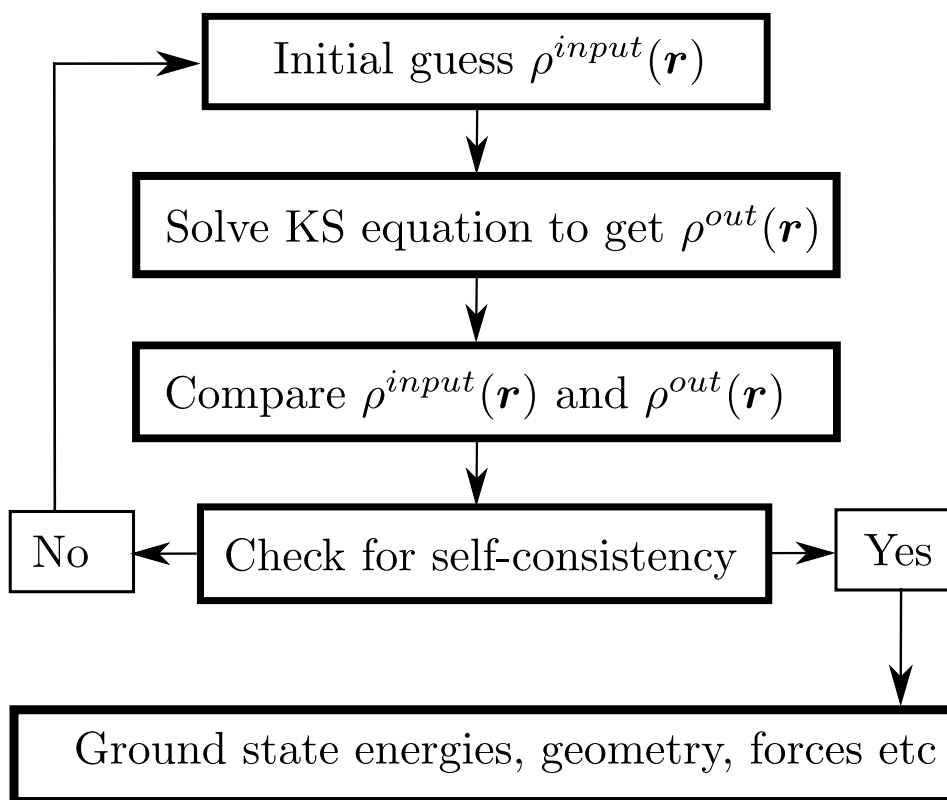


Figure 2.2: The SCF algorithm implemented in DFT.

2.2.1 Plane wave method

In this method, the wavefunctions or the eigenfunctions of the Kohn-Sham equations are expanded in a complete set of plane waves $\{e^{i\mathbf{k}\cdot\mathbf{r}}\}$. Pseudopotentials are used to replace the external potential of the nucleus. Plane waves have played an important role in the early orthogonalized plane wave calculations and are generalized to modern projector augmented wave (PAW) method [35]. In this method, forces can be easily calculated and it can be easily developed to quantum molecular dynamics simulations as well as response to external perturbations. However, results from plane wave methods using pseudopotentials are usually less accurate than results from all-electron full potential methods. Great care should be taken when one generates a pseudopotential and it should be tested to match results from all-electron calculations. The most widely used codes using plane waves and pseudopotentials are VASP [54], Quantum ESPRESSO [55], ABINIT [56], etc. By using Bloch's theorem [57] one can simplify the system from an infinite number to a finite number of electrons within a single primitive unit cell. In the case of a periodic system the expansion of the of the wave function in the form of discrete plane wave basis set in such a manner:

$$\phi_{(k,j)}(\mathbf{r}) = \sum_G C_{(j,k+G)} e^{i(k+G)\cdot\mathbf{r}} \quad (2.20)$$

where $\{G\}$ is the reciprocal lattice vector, $\{k\}$ is restricted to the first Brillouin zone [58] and $\{j\}$ is the band index. The energy cutoff is given by:

$$E_{cutoff} = \frac{\hbar^2}{2m} |K + G|^2 \quad (2.21)$$

By enlarging $\{E_{cutoff}\}$ one can control the quality of the calculations. The cutoff energy is not the only parameter which influences the convergence. Also, the size of the supercell is an important factor. The reason is that the plane wave basis set is periodic in all three space directions. If the super cell is too small neighboring molecules interact strongly with each other. Hence, a high-energy cutoff, adequate number of k-points and a large box size is required so that the system is converged.

2.2.2 Localized atomic orbital method

Plane waves are not the most effective approach when it comes to accurately describing molecular systems. The most common way to solve the problem is to the expand the one-electron wavefunctions as molecular orbitals in terms of atomic orbitals. These atomic orbitals can be represented in terms of basis functions in various functional forms. These basis functions when used in a large number improves the accuracy and hence the electronic properties. One of the most well-known methods in this category is the linear combination of atomic orbitals (LCAO). SIESTA [59] is also a band structure DFT program employing periodic boundary conditions in all three directions. It employs a

linear combination of atomic orbitals (LCAO) basis set, which in turn provides us with the information of orbitals that we are most interested in. It also provides us with the molecular orbital density of states, which contains the contributions of each of the molecular orbital to the total electronic density of states (DOS). By integrating these states up to the Fermi energy, the occupation of each orbital can be obtained. The result yields the occupation of these orbital in electrons where we can distinguish the occupied and the unoccupied orbitals from each other. It also allows the use of localized linear combinations of the occupied orbitals like the valence-bond, or Wannier-like functions [60], scaling linearly with the number of atoms making each and every calculations computationally efficient.

2.3 Electronic transport

Similar to the electronic structure calculations, the theoretical description of quantum electron transport through molecular systems is also a very complicated many-body problem to solve. Different methods and approaches have been proposed ranging from solving the exact many-body problems to semi-empirical models. Among all these available methods we use the so-called *ab initio* method, also often known as the first principle calculations that only requires the geometry of the system, to begin with. Later on, the transport properties can be calculated using the Green's functions and the DFT. In this section, we demonstrate how the transport formalism can be combined with standard electronic structure method to provide a first-principle description of electron transport in a molecular junction. The method is solely based upon the non-equilibrium Green's function (NEGF) method [61].

2.3.1 Molecular junction

A molecular junction is a geometrical setup where a finite scattering region also called as the central region is connected to two semi-infinite periodic systems or lead. Schematic diagram of a molecular junction is depicted in Fig. 2.3. Here, $\{L\}$ and $\{R\}$ are the two semi-infinite left and right metallic leads or electrodes and $\{C\}$ is the central region which comprises of the molecule. When we apply a bias voltage the charge carriers flow from the left lead to the right one through the molecule. It is very important not to have a very short molecule to avoid tunneling between the electrodes. Molecular orbitals play a very important role in transport calculations. The alignment of these molecular orbitals with respect to their Fermi level of the electrodes is important for conductance in between the electrodes. The conductance is observed as the result of the charge transfer to or from the molecule and the electrodes. The total Hamiltonian of the system usually comprises of the Hamiltonian of the central region $\{H_C\}$, of the left electrode $\{H_L\}$ and the right electrode $\{H_R\}$ and lastly the interaction of the molecule and the electrodes $\{V_{int}\}$ respectively. This is illustrated in a

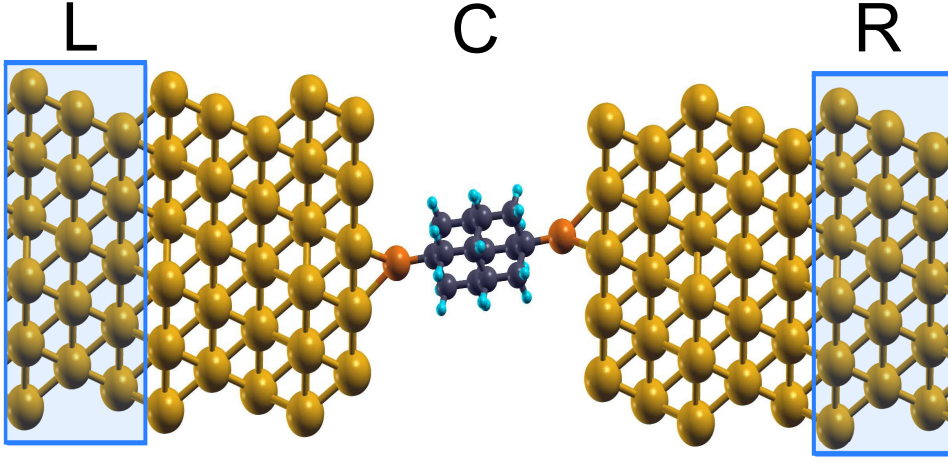


Figure 2.3: Here we show a diagram of a diamondoid based molecular junction where (C) is the central region between the two semi-infinite left (L) and right (R) leads.

form of an equation below:

$$H = H_L + H_C + H_R + V_{int} \quad (2.22)$$

We need to keep in mind that the Hamiltonian for each of the electrodes denoted by $\{H_{L/R}\}$ has infinite dimension. As a consequence, we introduce a screening approximation. In doing so, we now reduced the infinite dimension of the Hamiltonian to just the dimension of the Hamiltonian of the molecule. However, the semi-infinite behaviour of the electrode is taken into account by using self-energy. This is how we construct an effective Hamiltonian:

$$H_{eff} = \sum_L + \sum_R + H_C \quad (2.23)$$

where $\{\sum_{L/R}\}$ is the self-energy term for the left and right electrodes and $\{H_C\}$ is the Hamiltonian of the molecule.

The size and the length scale $\{L\}$ of the molecular junction plays a very important role in defining the transport regimes. Basically, the regimes depend on two different parameters namely: the mean free path $\{L_m\}$, where the electrons travel until their momentum relaxes and the other one is the phase relaxation length $\{L_\phi\}$, where the electrons travel until they achieve phase relaxation. Hence the length $\{L\}$ has to be small enough to avoid classical conductance behaviour. Various kinds of transport regimes on the basis of the length scale of L , L_ϕ , and L_m can be listed which are described below:

- If $\{L\}$ is very small than $\{L_m\}$, there is no scattering during the transport process in the device and it belongs to the ballistic transport regime. Carbon-based materials and metallic nanowires show ballistic transport behaviour.

- In the case of the short molecules where $\{L\}$ is smaller than $\{L_m\}$, the electron transport is elastically scattered. Reason being that the electron transport is quick enough to not react with other molecular vibrations. This kind of regime is known as the coherent or elastic regime.
- If we are dealing with long molecules, electron transport take long enough to interact with another electron in the system. This results in inelastic scattering and hence it is named as an incoherent or inelastic regime.

In order to describe the transport mechanism for the elastic transport regimes, one uses DFT coupled with NEGF formalism. The Hamiltonian in terms of $\{L, C, R\}$ is formulated as:

$$H = \begin{pmatrix} H_{LL} & H_{LC} & 0 \\ H_{CL} & H_{CC} & H_{CR} \\ 0 & H_{RC} & H_{RR} \end{pmatrix}. \quad (2.24)$$

Similarly, the overlap matrix $\{S\}$ is defined as:

$$S = \begin{pmatrix} S_{LL} & S_{LC} & 0 \\ S_{CL} & S_{CC} & S_{CR} \\ 0 & S_{RC} & S_{RR} \end{pmatrix}. \quad (2.25)$$

Next step is to calculate the self-energy term of the left and right electrode including the molecule. After we construct the self-energy matrix, we can substitute and obtain the effective Hamiltonian $\{H_{eff}\}$ from equation 2.23. Now the retarded Green's function $\{G^r\}$ matrix is formulated which is based upon electron density and is written as follows:

$$G^r(E) = [ES - H_{eff}] \quad (2.26)$$

where $\{H_{eff}\}$ is the effective Hamiltonian $\{S\}$ is the overlapping matrix and $\{E\}$ is the self-energy term. Finally, since the effective Hamiltonian $\{H_{eff}\}$ and the retarded Green's function $\{G^r\}$ are functional of electron density, a self-consistent calculation is performed to obtain the final electron density.

Next, using the Landauer-Buttiker [62] formula, the transmission coefficient is calculated as a function of energy and current $\{I(V)\}$ at a certain bias voltage $\{V_b\}$ which is given as follows:

$$T(E, V_b) = Tr \left[\Gamma_L(E, V_b) G^a(E, V_b) \Gamma_R(E, V_b) G^r(E, V_b) \right] \quad (2.27)$$

where $\{G^a\}$ is the advanced and $\{G^r\}$ is the retarded Green's function, $\{E\}$ is the self-energy term, $\{\Gamma_L\}$ and $\{\Gamma_R\}$ denotes the energy level broadening of the left and the right electrode, respectively. The current $\{I(V)\}$ can be written as:

$$I(V) = \frac{e}{\pi\hbar} \int \left[T(E, V_b) f_L(E, V_b) - f_R(E, V_b) \right] dE \quad (2.28)$$

$$= \frac{e}{\pi\hbar} \int T(E, V_b) \left[f_L(E, \mu_L) - f_R(E, \mu_R) \right] dE \quad (2.29)$$

where $\{f_{L/R}\}$ is the Fermi-Dirac distribution of the left and right electrodes and $\{\mu_L\}$ and $\{\mu_R\}$ are the chemical potential with respect to the left and the right electrode.

2.4 Time-dependent density functional theory

In this section, we describe an extension of DFT where the potential and the electron density of the system vary in time. We begin by introducing the Runge-Gross theorem which forms the basis of time-dependent density functional theory. Next, we discuss the application of time-dependent density functional theory (TD-DFT) to the problem of calculating electronic excitation energies of molecules.

2.4.1 Runge-Gross formalism

Runge gross theorem [63] states that for a many-body system that is evolving in time from a fixed initial state there is a one-to-one correspondence between the time-dependent external potential $\nu_{ext}(\mathbf{r}, t)$ and the electronic density $\rho(\mathbf{r}, t)$. This implies that we only need the density of a system in order to obtain an external potential which can be used to solve the time dependent Schrödinger equation. According to the Runge-Gross theorem proved that two potentials $\{\nu_1(\mathbf{r}, t)\}$ and $\{\nu_2(\mathbf{r}, t)\}$ which differ from each other by a time-dependent constant term $\{c(t)\}$ cannot produce the same time-dependent electron density $\{\rho(\mathbf{r}, t)\}$:

$$\nu_1(\mathbf{r}, t) \neq \nu_2(\mathbf{r}, t) + c(t) \quad (2.30)$$

$$\rho_1(\mathbf{r}, t) \neq \rho_2(\mathbf{r}, t) \quad (2.31)$$

As a result, with the help of the Runge-Gross theorem, we can formulate the time-dependent Kohn-Sham scheme. Similar to the time-independent case, we introduce an auxiliary system of non-interacting electrons to an external potential $\{\nu_{KS}\}$. The external potential is chosen in such a way that the density of the Kohn-Sham electrons is the same as the density of the original interacting system. Hence in this manner, with the help of Kohn-Sham and Runge-Gross theorems the time-dependent Schrödinger equation can be written as:

$$i \frac{\partial}{\partial t} \phi(\mathbf{r}, t) = \hat{H}_{KS}(\mathbf{r}, t) \phi_i(\mathbf{r}, t) \quad (2.32)$$

Now the Hamiltonian can be expressed as:

$$\hat{H}_{KS}(\mathbf{r}, t) = \frac{\nabla^2}{2} + \nu_{KS}[\rho](\mathbf{r}, t) \quad (2.33)$$

Next, we formulate the time-dependent electron density in terms of square moduli of the Kohn-Sham orbitals $\{\phi_i\}$:

$$\rho(\mathbf{r}, t) = \sum_{i=1}^N |\phi_i(\mathbf{r}, t)|^2 \quad (2.34)$$

As in the time-independent case, it breaks down into a sum of three terms:

$$\nu_{KS}[\rho](\mathbf{r}, t) = \nu_{Ext}(\mathbf{r}, t) + \nu_{Hartree}[\rho](\mathbf{r}, t) + \nu_{xc}[\rho](\mathbf{r}, t) \quad (2.35)$$

The first term $\{\nu_{Ext}(\mathbf{r}, t)\}$ on the right-hand side of equation 2.35 is the external potential acting on the electrons, which contains the electrostatic potential of the nuclei as well as the time-dependent external potential that is assumed to act on the electrons. If the time-dependent part of the external potential is subjected to the electric field component of the electromagnetic radiation, then $\{\nu_{Ext}(\mathbf{r}, t)\}$ will be given by:

$$\nu_{Ext}(\mathbf{r}, t) = Ef(t)\sin(\omega t)\mathbf{r} \cdot \boldsymbol{\alpha}' \sum_{a=1}^{N_{nuc}} \frac{Z_a}{|\mathbf{r} - \mathbf{r}_a|} \quad (2.36)$$

where $\{\boldsymbol{\alpha}'\}$ is the polarization vector of the electromagnetic wave, $\{E\}$ is the amplitude of its electric field component and $\{\omega\}$ is its frequency. $\{f(t)\}$ is an envelope function that controls the shape of the electromagnetic wave. Similarly, the second term $\{\nu_{Hartree}[\rho](\mathbf{r}, t)\}$ on the right-hand side of Eqn. 2.35 is the Hartree term $\{\nu_{Hartree}\}$ that describes the instantaneous self-interaction energy of the electron density.

$$\nu_{Hartree}[\rho](\mathbf{r}, t) = \int \frac{\rho(\mathbf{r}', t)}{|\mathbf{r} - \mathbf{r}'|} d^3 d\mathbf{r}' \quad (2.37)$$

The third term $\{\nu_{xc}[\rho](\mathbf{r}, t)\}$ is the time-dependent exchange-correlation potential. It contains the quantum-mechanical many-body effects that are missing from the Hartree term and also corrects the kinetic energy that is being calculated for the Kohn-Sham spin-orbitals which describe the auxiliary system of non-interacting electrons.

2.5 Computational tools

The **SIESTA** [59] package was used to investigate the electronic and transport properties of diamondoid-based complexes. Spanish Initiative for Electronic Simulations with Thousands of Atoms or SIESTA is a very efficient tool to execute electronic structure calculations and also an *ab initio* molecular dynamics simulations. SIESTA uses localized basis sets which scales linearly and hence can be implemented over all kinds of the system under study. A very important feature of the code is that it is very accurate and computationally efficient producing results that are of the same quality as of other approaches, such as plane-wave or all-electron methods. Some of the main characteristics of SIESTA is the use of Kohn-Sham self-consistent density functional method with LDA and GGA approximation with the inclusion of van der Waal's interaction. It uses norm-conserving pseudopotential with atomic orbitals as basis

sets.

Electronic transport calculations were performed using DFT combined with the non-equilibrium Green's functions (NEGF) formalism, as implemented in the **TranSIESTA** [64] code. TranSIESTA facilitates the modelling and simulation of electronic molecular junctions or devices. The tranSIESTA calculation usually involves three parts. First, the electronic structure of the leads is calculated with a DFT calculation and then the Hamiltonian for the infinite leads which are saved for the subsequent steps. Next, a periodic SIESTA calculation is performed for a system that includes the central region and the leads. This yields the Hamiltonian and density matrix for the central region. Next, the Hamiltonian for the leads and the central region is used to calculate the retarded Green's function. The density is calculated by integrating over the retarded Green's function using an efficient contour integration technique that requires only a few energy points. This yields a Hamiltonian for the central region. A separate self-consistent iteration for the Green's function makes it possible to calculate the electronic structure for a system with a finite bias voltage between the electrodes. Finally, the transmission calculation is performed by a utility known as TBTrans.

Vienna *ab initio* simulation package or **VASP** [54] was used under the framework of DFT in order to self-assemble the monolayer of diamondoid-based complexes over the metal surfaces. In addition to the electronic structure calculation, it also performs quantum-mechanical molecular dynamics from the first principles. Unlike SIESTA, in VASP, the one-electron orbitals, the electronic charge density, and the local potential are expressed in plane wave basis sets. The electron-electron and the ion-ion interactions are described using norm-conserving or ultrasoft pseudopotentials, or the projector-augmented-wave method. Its basic aim is to compute an approximate solution to Schrödinger equation, either with DFT by solving the Kohn-Sham equations or within the Hartree-Fock (HF) approximation.

General Atomic and Molecular Electronic Structure System or **GAMESS-US** [65] package was used to compute the excited state properties of functionalized diamondoids. GAMESS-US is a program for *ab initio* molecular quantum chemistry. Correlation corrections to the SCF wavefunctions is not only implemented by the density functional theory approximation but with additional configuration interaction (CI) [66], second order perturbation theory [67], and coupled-cluster approaches [68]. Excited states can be computed by CI or TDDFT procedures.

Chapter 3

Modified diamondoids: doping and functionalization

In this chapter, we focus on the structural alterations and the effect of doping and functionalization on the electronic and optical properties of diamondoids, from the smallest adamantane to heptamantane. In section 3.1, we present a brief introduction of diamondoids and their possible application after doping and functionalization. Next, we present the analysis of the results for doped diamondoids using boron, nitrogen, silicon, oxygen, and phosphorus as dopants. In view of the diamondoid-based devices we mainly focus on a double-functionalization of diamondoids up to heptamantane using both these atomic groups with amine and thiol groups. We discuss the higher efficiency of a double-functionalization compared to doping or a single-functionalization of diamondoids in tuning the electronic and optical properties, such as the electronic and optical band gap of modified small diamondoids in view of their novel nanotechnological applications. Finally, in section 3.4, a short discussion based on the work is presented. Some of the sections of this chapter are also the part of our published article "Bibek Adhikari and Maria Fyta 2015 Nanotechnology 26 035701 © IOP Publishing. Reproduced with permission. All rights reserved".

3.1 Introduction

The variety of sizes and modifications diamondoids can assume have shown their great potential for novel nanotechnological applications [10,13,14]. Different production methods of diamondoids exist: these can be found in petroleum [4], be organically synthesized [2] or also nucleated from energetic species [3]. Diamondoids are expected to play a significant role as suitable building blocks for functional nanostructures [15]. These nanometer-sized cages can be attached on metallic surfaces through a thiol group [18,19] and form self-assembled layers which have a negative electron affinity [10,11] and a strong monochromatic emission [10,69], being thereby promising for electronics applications. Lower diamondoids and their derivatives have been theoretically observed to self-assemble into larger interlinked nanostructures [16] also with

the possibility of self-assembly of diamondoids encapsulated inside carbon nanotubes [5–7]. Diamondoids doped with boron and nitrogen atoms can be interlinked to form functional nanostructures in carbon nanotubes [15], while lower diamondoids and their derivatives have also been theoretically found to self-assemble into larger interlinked nanostructures [16]. In view of biotechnological applications, efficient site-specific incorporation of diamondoids on DNA are possible [8], as well as the use of diamondoids as biosensors for reading-out DNA molecules [9].

The possibility of chemical modification of diamondoids [2] has opened a new dimension in nanotechnology [10]. The size, the art of doping, and functionalization of diamondoids can tune their properties, such as optical and electronic [70, 71]. Amine functionalized diamondoids have good conductance properties [16], while thiolated diamondoids attached to the gold surface show excellent electron emission properties [18]. Studies have shown that the band gap of these nano diamonds decrease with the increase in their size and push-pull doping is believed to be the most effective way to tune the band gap of these diamondoids [72]. Modified diamondoids also show alterations in their optical properties as compared to those of unmodified diamondoids [18]. Amine-derivatives [73] of the lower diamondoid, adamantane, are already in use in pharmaceutical applications [74] as anti-viral [75] and anti-Parkinsons agents [76]. These derivatives have also been found to have good conductance properties depending on their relative orientation between two metallic electrodes [77]. In view of their nanotechnological applications, these doped and functionalized diamondoids can be excellent electron emitters, better than carbon nanotubes for field-emission displays (FEDs) [10]. These diamondoid-based FEDs as electron emitters could be seen as the future of flat-panel displays, microwave telecommunications and microelectronics [10, 78–80]. Recent research has also shown that these diamondoids combined with buckyballs form to show faster and powerful device as the unimolecular rectifier [81].

We aim to extend previous studies on modified diamondoids and the alteration of their electronic properties in view of the novel nanotechnological application. Along these lines, we focus on doping and functionalization of diamondoids with five different dopants and the use of a single- and double-functionalization with atomic groups on the same diamondoid. The investigation of a pathway to selectively tune the conduction properties of the modified diamondoids is the main goal of this work. The novelty of this study is related to the double-functionalization, which to our knowledge has not been studied before. The purpose of the double-functionalization is based on the nanotechnological applications of diamondoids: the first functionalization (usually a thiol group) can be used to attach diamondoids on surfaces, while the second (the amine group) has been widely used in drug industry and can tune the electronic properties of the diamondoid-functionalized surface or promote the attachment of other species on this surface.

3.2 Electronic properties of diamondoids

We have implemented SIESTA [59] code under the framework of DFT for the analysis of the electronic properties of doped and functionalized diamondoids. Using Siesta scheme, the Kohn-Sham eigenstates are expanded using a linear combination of atomic orbitals. The local density approximation (LDA) [82] was used in modelling the exchange-correlation functional together with norm-conserving Troullier-Martin type pseudopotentials [83] a split valence double zeta polarized basis set. A mesh cutoff parameter of 200 Ry has been used for the calculations. The geometry optimization was performed using the conjugate gradient algorithm and the structure was relaxed until forces on the atoms were lower than 0.04 eV/Å.

For computational efficiency, the smaller diamondoids adamantane ($C_{10}H_{16}$) up to heptamantane ($C_{30}H_{34}$) were modelled. The ideal diamondoids include only carbon atoms which form the diamond-like cages and the hydrogen atoms which passivate the cages. Our investigation is being carried out as follows: First, we choose a diamondoid site, remove one of its carbon atoms and replace it with a dopant. As representative dopants, also due to their proximity to carbon in the periodic table, we choose boron (B), nitrogen (N), silicon (Si), phosphorous (P), and oxygen (O). At a second step, we study the selective functionalization of the lower diamondoids. We begin with a single functionalization, by replacing one of the hydrogen atoms of the diamondoid with a thiol- (SH-) or amine- (NH_2 -) atomic group. At a final step, we double functionalize the diamondoids with both the thiol- and amine groups. We use some of the dopants which have been studied before for diamondoids, in order to provide a consistent study towards the double-functionalized diamondoids, which is the main interest of this work.

Specifically, for the doped diamondoids, we have followed previous studies which indicated the dopant site [72], but also performed a "dopant-site scan" through a comparison of possible doping sites for each dopant based on an energy minimization. Accordingly, the single site for each dopant which corresponded to the minimum energy was chosen as the doping site for a further investigation of the electronic structure of the respective doped diamondoid. Note, that the dopant site is not the same for each doped diamondoid. In the single-functionalized diamondoids, the functional (amine- or thiol-) group was attached to an apical site (which is not the same for the two groups) of the diamondoid substituting the hydrogen atom at that site. We have performed simulations for three different functionalization cases: amine-, thiol-, and amine-,thiol-functionalized diamondoids. For the first two, we refer to single-functionalization, while for the last as double-functionalization. For the former, the functionalization sites were taken from the literature [18]. In the double-functionalization, the same site as in the single-functionalization was used for attaching the amine group. The thiol group functionalization site was based on a scan based on an energy minimization corresponding to struc-

tures with different functionalization sites. The two substitutional sites for the amine- and thiol groups are the opposite apical tips of a diamondoid. Along the above lines, we probe the possibilities of tuning the band gap through modifications of the diamondoids using the dopants or functional groups mentioned above.

Along these lines, we study the stability, structural alterations as well as the effect on the electronic properties of the modified (doped, single-, and double-functionalized) diamondoids with respect to the properties of ideal unmodified diamondoids. The electronic properties in all cases are probed through the electronic density of states (eDOS), the frontier orbitals, namely the highest occupied (HOMO) and lowest unoccupied molecular orbitals (LUMO), as well as the electronic band gap. The electronic band gap is defined as the difference between the HOMO and LUMO levels.

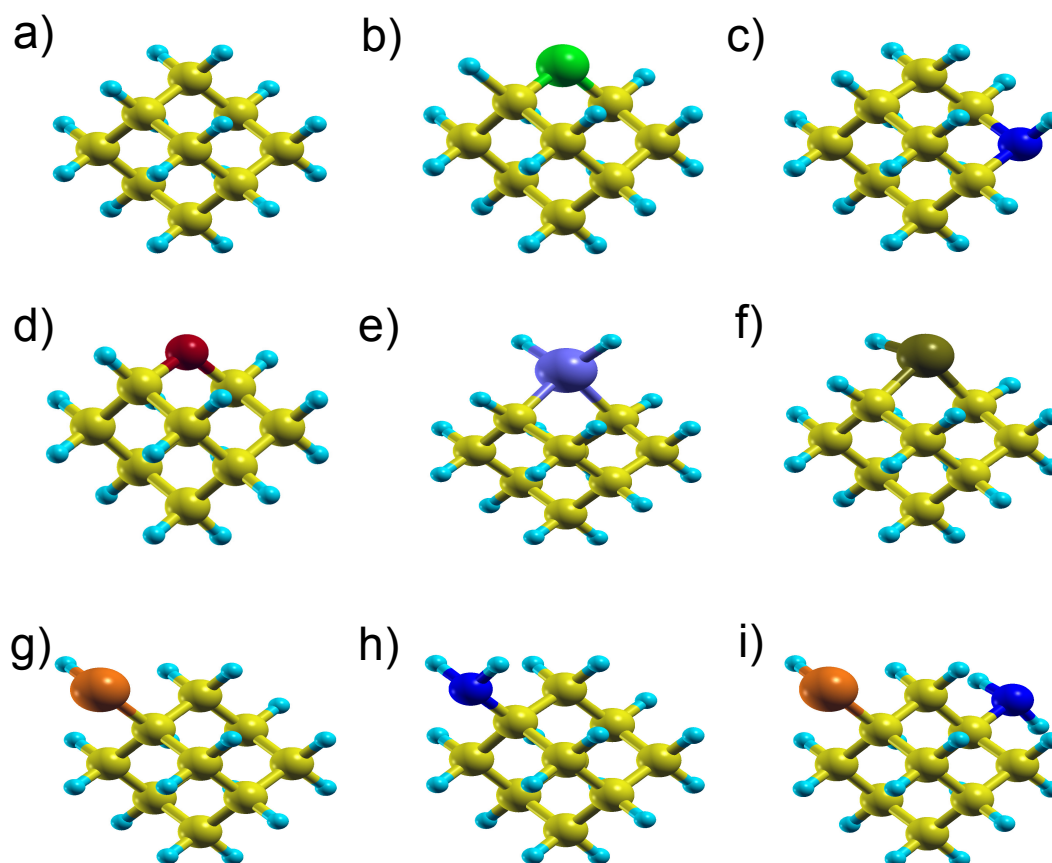


Figure 3.1: (a) Ideal adamantane. In (b)-(f) the relaxed doped structures for B-adamantane, N-adamantane, O-adamantane, Si-adamantane, and P-adamantane are shown, respectively. In (g) and (h) the single-functionalized adamantane with an amine- and a thiol- group are depicted, respectively, while in (i) the double- functionalized amine-, thiol- adamantane is sketched.

Results and Discussion

We begin our analysis with doped diamondoids and choose the lowest one, adamantane, as a representative case. The aim is to provide a proof of principles as to the effect of doping and it is expected that doping other diamondoids should show similar qualitative trends. We continue with a single- and double-functionalization of adamantane and move on to the effect of isomerization. For this, we choose the three isomers of tetramantane and double-functionalize these. In the end, we focus on the double-functionalization of the lower diamondoids up to heptamantane.

3.2.1 Adamantane

All the modified adamantane structures considered in the following analysis are depicted in Fig. 3.1 in which the ideal adamantane is also shown for comparison. In order to qualitatively evaluate this picture, the corresponding structural properties are plotted in Fig. 3.2. On the two panels of this figure, the bond-angle and bond-length variations in the doped adamantane cases are shown. A first observation is related to the deviation from the almost perfect tetrahedral arrangement in ideal adamantane. The bond lengths for Si- and P-doped adamantane have been stretched whereas for the N- and O-doped cases the bond lengths are shorter than 1.53 Å, which is the C-C bond length for ideal adamantane. This implies a stronger bonding between the C-N, C-O and C-B atom-pairs than in C-Si or C-P. Accordingly, as expected, N, B, and O are better dopants for the diamond-like cages, in terms of their structural properties and the deviation from the tetrahedral symmetry. The same trend was found in the bond-angle variation with the dopant type as evident in the lower panel of Fig. 3.2. The C-C-C bond angle in the ideal adamantane is found to be 109.7°. The bond angles in case of N- and O-doped adamantane do not change much as compared to Si -, B -, P-doped adamantane. A different trend is observed for the B-doped adamantane as the C-B-C bond-angle deviated more from the ideal case as in the Si-doped adamantane, though the reversed was observed for the respective bond lengths. In order to investigate the stability of these modified adamantanes, we calculated the substitution energy of these newly formed molecules and the energy values are shown in Fig. 3.3. The substitution energy E_s of these doped and functionalized structures was calculated by using the formula

$$E_s = E_{doped/func} + E_{subs} - E_{adamantane} - E_{added} \quad (3.1)$$

where $E_{doped/func}$ is the total energy of the doped or functionalized molecule, E_{subs} is the total energy of replaced or substituted units; CH₄ in case of doped structures and H₂; in case of functionalization, $E_{adamantane}$ is the total energy of a pure adamantane molecule, E_{added} is the total energy of the added units; namely BH₃, NH₃, OH₂, SiH₄, PH₃, H₂S for different dopants and functional groups mentioned above. In Fig. 3.3 the variation of energy with different dopants is given. A lower substitution energy according to the definition corresponds to an easier substitution reaction. In the case of doped diamondoids,

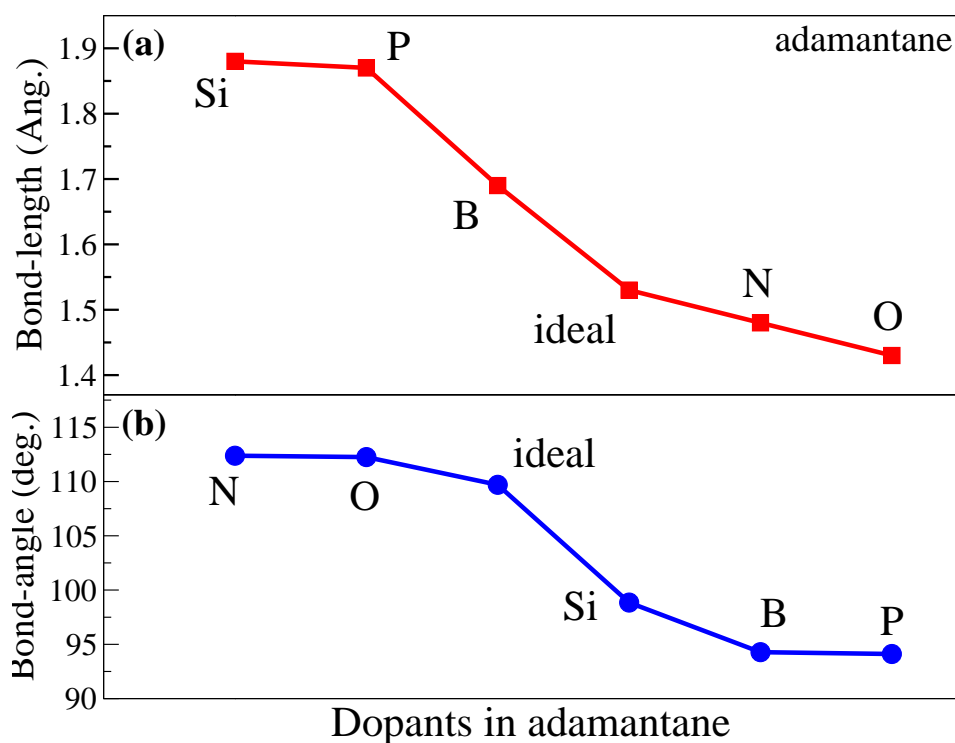


Figure 3.2: Variation of (a) the bond length and (b) bond angle with the type of dopant in adamantane.

the energy is lowest for the B-doped case with a higher negative value indicating natural substitution reaction whereas for functionalization thiols show lesser substitution energies as compared to amine and thiol plus amine functionalized cases. Next, we move on to the electronic density of states (eDOS) of the doped adamantane molecules which are sketched in the upper panel of Fig. 3.4. The eDOS of the doped structures are considerably altered by the presence of dopants as compared to the ideal adamantane. Although in most cases, the HOMO and LUMO levels are similarly occupied, the doping introduces electronic states in the band gap of the ideal case, decreasing in this way the band gap of doped-adamantane. This shrinking of the band gap is different for different dopants. Regarding the occupation of the HOMO and LUMO levels, these deviate from ideal adamantane in the P- and Si-doped adamantane, which actually shows a larger deviation in the strength of the C-dopant bond as discussed above.

In order to provide a better qualitative understanding of the differences in the electronic structure of doped-adamantane, the frontier orbitals, HOMO and LUMO are sketched in Fig. 3.5(b)-(f). In the ideal adamantane, the HOMO or the occupied states are localized over the C-C bonds whereas the unoccupied states are more delocalized and spread out over the whole molecule [13]. These orbitals become less delocalized in the doped-adamantane, in which the HOMO state becomes almost localized on the dopant site. Deviations were observed

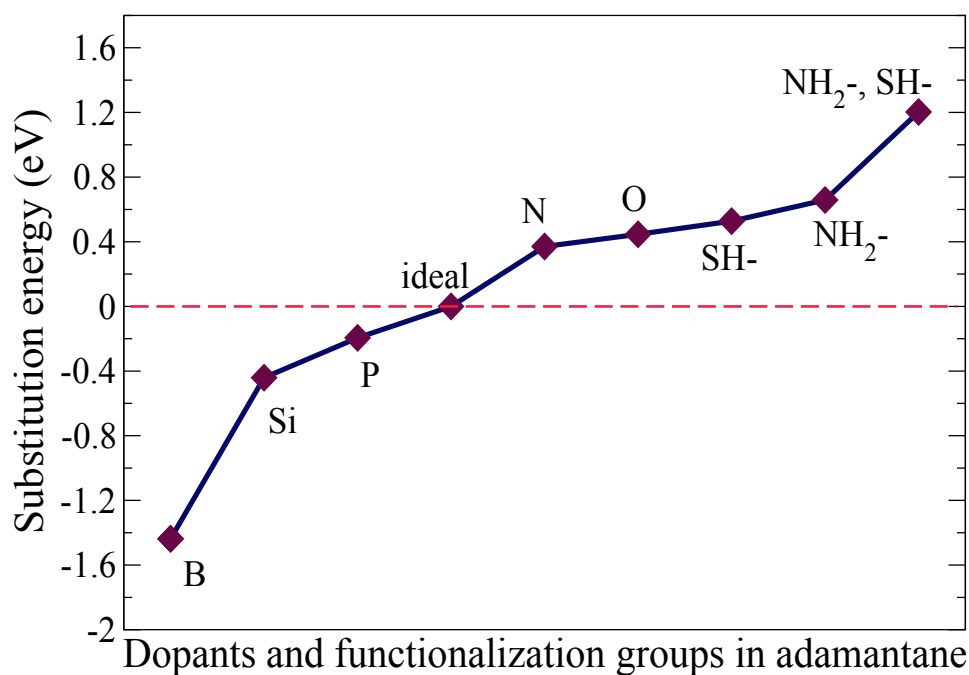


Figure 3.3: Variation of the substitution energies for doped and functionalized adamantane compared to its ideal case. Lower substitution energy values imply easier substitution reaction than the higher ones.

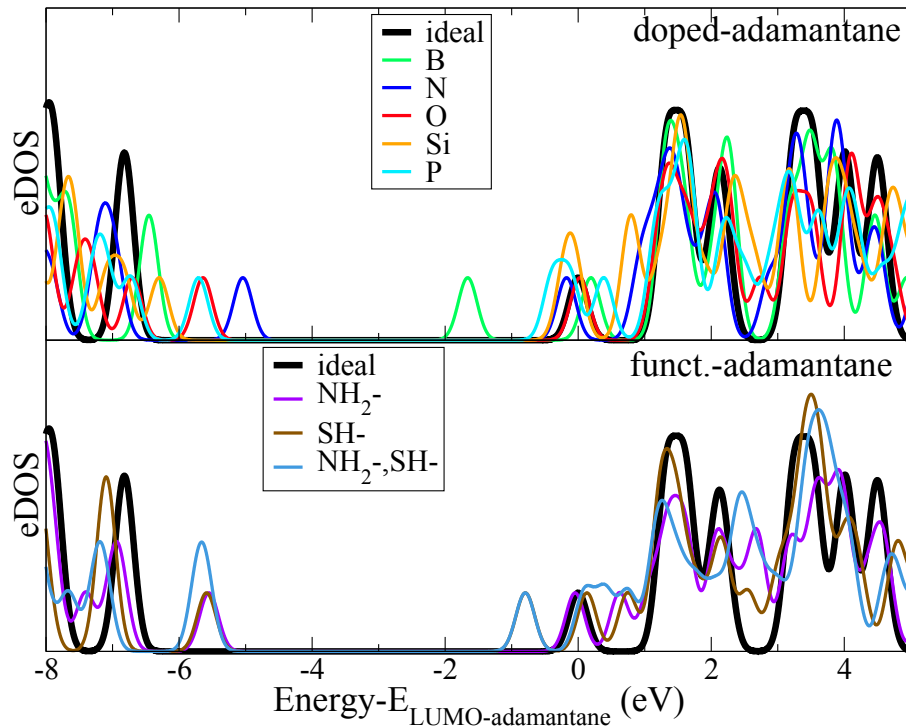


Figure 3.4: Electronic density of states (eDOS) for doped and functionalized adamantane. All data have been shifted with respect to the LUMO level of ideal adamantane, as denoted in the x-axis.

in the B-doped adamantane, while the less localized orbitals were observed in the O-doped case, though this case had shown a larger deviation from the ideal case as discussed above. The total charge density contours of the doped and functionalized adamantanes as shown in Fig. 3.6. We can clearly observe the qualitative difference in charge distribution over the surface of diamondoid with respect to different dopants and functional groups. This difference is based on the fact that these dopants possess different electro-negativities. In addition, the variation in the bonding behaviour of the dopants at the doping site also plays a significant role in the distribution of charge densities. These differences correspond to the HOMO and LUMO depicted in Fig. 3.5.

Next, we turn to single- and double-functionalized adamantane. The eDOS data of these cases with respect to ideal adamantane are shown in Fig. 3.4(lower panel). Similarly to the doped-adamantane cases, the eDOS are altered compared to the eDOS of ideal adamantane. Again, the presence of one or two functional groups is related with the addition of electronic states in the band gaps of ideal adamantane decreasing the band gap of functionalized-adamantane. The occupation of the LUMO levels is similar to the ideal case, while in the double-functionalization the occupation of the HOMO level differs. The respective HOMO and LUMO states are sketched in Fig. 3.5(g)-(i), from which it is evident that these are much more localized than in the doped-adamantane cases. Both HOMO and LUMO levels are associated and localized on the functional groups. In the double-functionalized adamantane, only the HOMO level is associated with the amine group similar to the amine-functionalized adamantane in which mainly the HOMO level is located on the functional group. In all three functionalized cases the HOMO state is more pronounced than the LUMO at the doping sites.

The variations in the electronic band gaps in both doped- and functionalized adamantane is shown in Fig. 3.7 as compared to the ideal adamantane. As evident from the previous analysis, the substitution of an atom in the ideal adamantane with another atom or atomic group, changes the band gap, hence the conducting properties, of the modified adamantane molecules. The band gap for ideal adamantane from our simulations was found equal to 6.82 eV whereas for B-doped adamantane the value decreased to 4.79 eV, which was the lowest value from all doped-adamantane cases studied here. A similar decrease in the band gaps was observed in the functionalized-adamantane. Interestingly the SH-adamantane has the same band gap as B-doped adamantane (4.79 eV), denoting that different modifications of the same molecule can result in very similar conducting properties. However, a double-functionalization of adamantane reduces the band gap even further to 4.63 eV. In this respect, an additional scanning of possible functional groups would make a further tuning of the electronic band gap of adamantane, and diamondoids in general, possible. Nevertheless, our findings underline the importance of a double-functionalization for a further shrinking of the band gap in diamondoids.

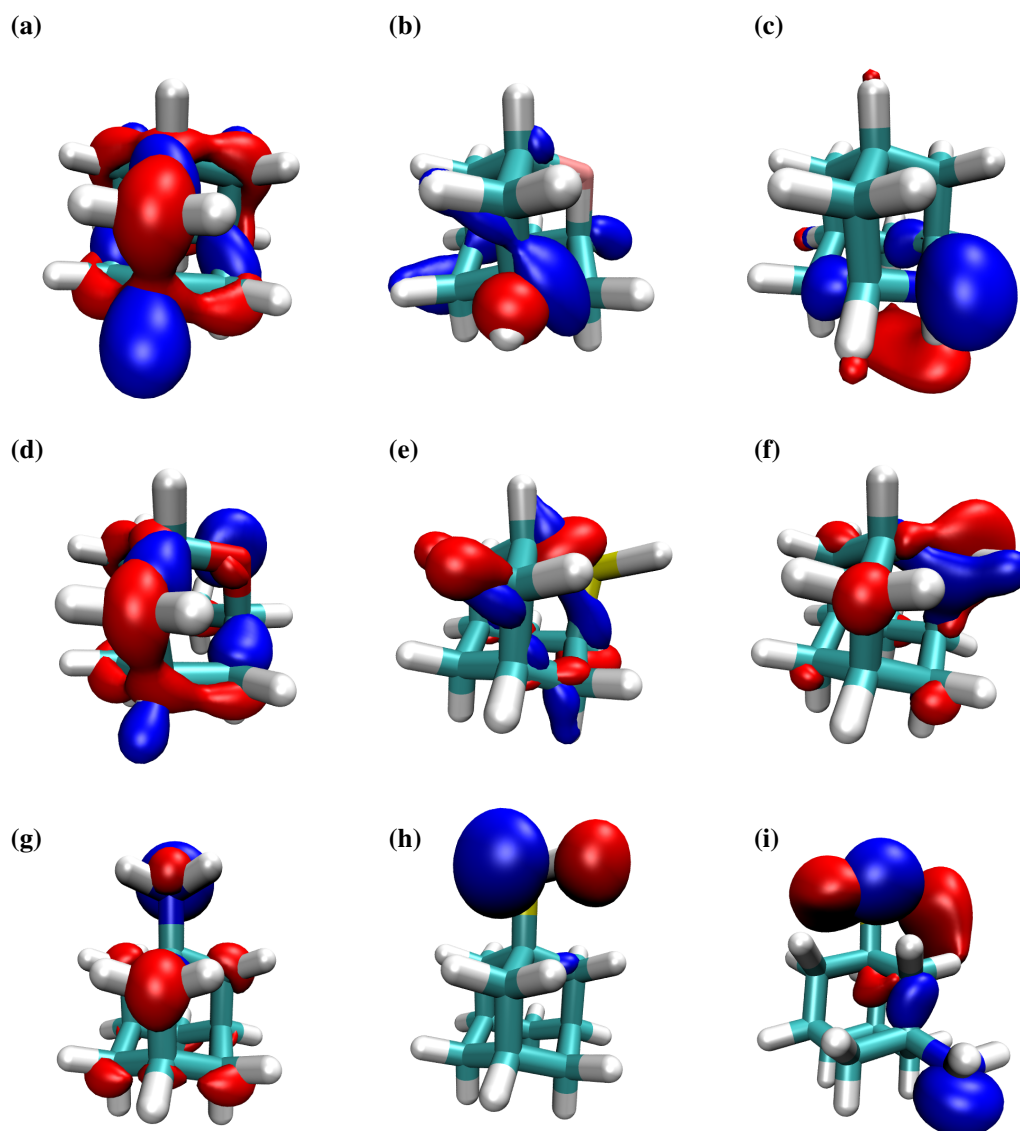


Figure 3.5: The frontier orbitals, HOMO (in blue) and LUMO (in red) for the (a) ideal and doped adamantane. In (b)-(f) these orbitals for the doped B-adamantane, N-adamantane, O-adamantane, Si-adamantane, and P-adamantane are shown, respectively. In (g) and (h) the HOMO and LUMO levels for single-functionalized adamantane with an amine- and a thiol group are depicted, respectively, while in (i) the double-functionalized amine-, thiol-adamantane is sketched.

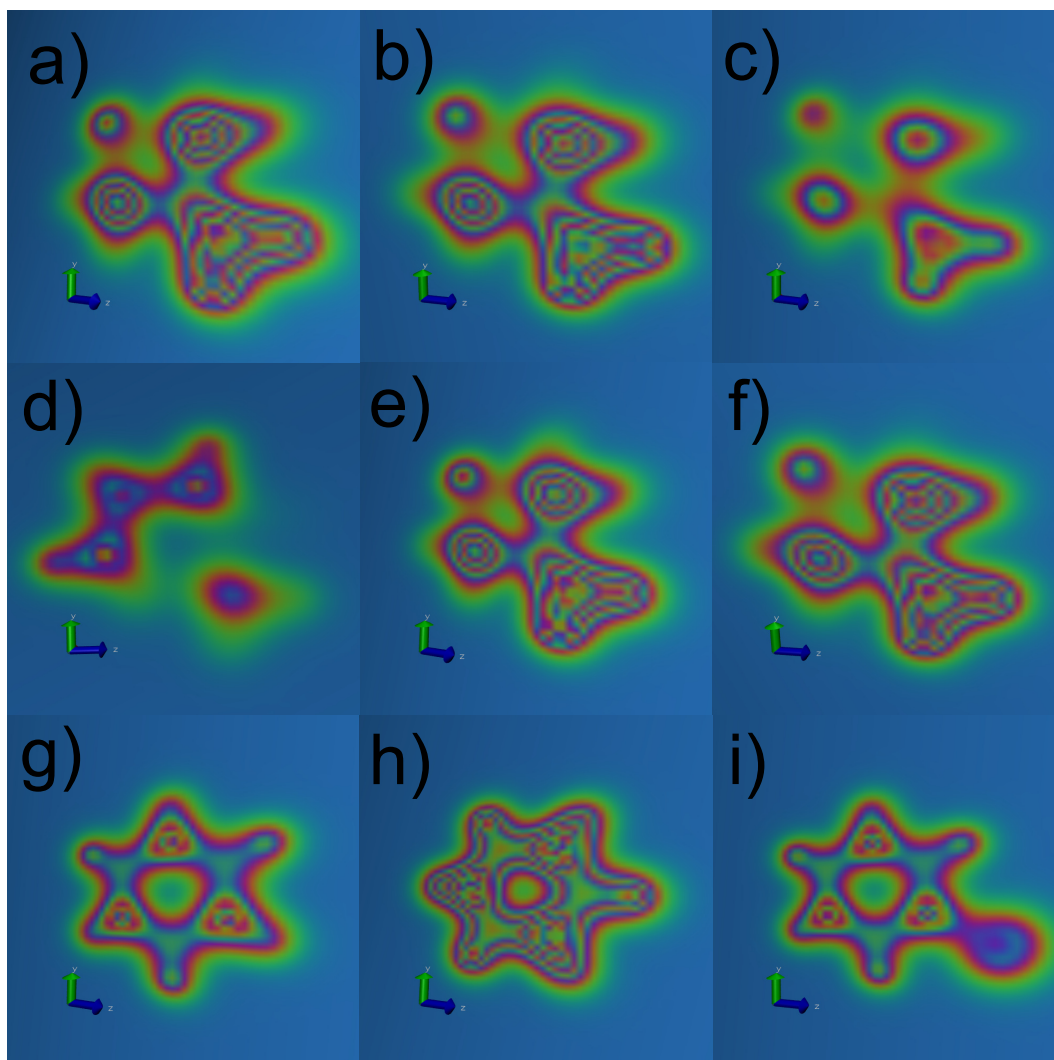


Figure 3.6: The 2-D contours are shown where the contours are sliced along X-direction for all the doped and functionalized adamantane. (a) Ideal adamantane. In (b)-(f) the charge densities contours for B-adamantane, N-adamantane, O-adamantane, Si-adamantane, and P-adamantane are shown, respectively. In (g) and (h) the single-functionalized adamantane with an amine- and a thiol- group are depicted, respectively, while in (i) the charge density of double-functionalized amine-, thiol- adamantane is sketched.

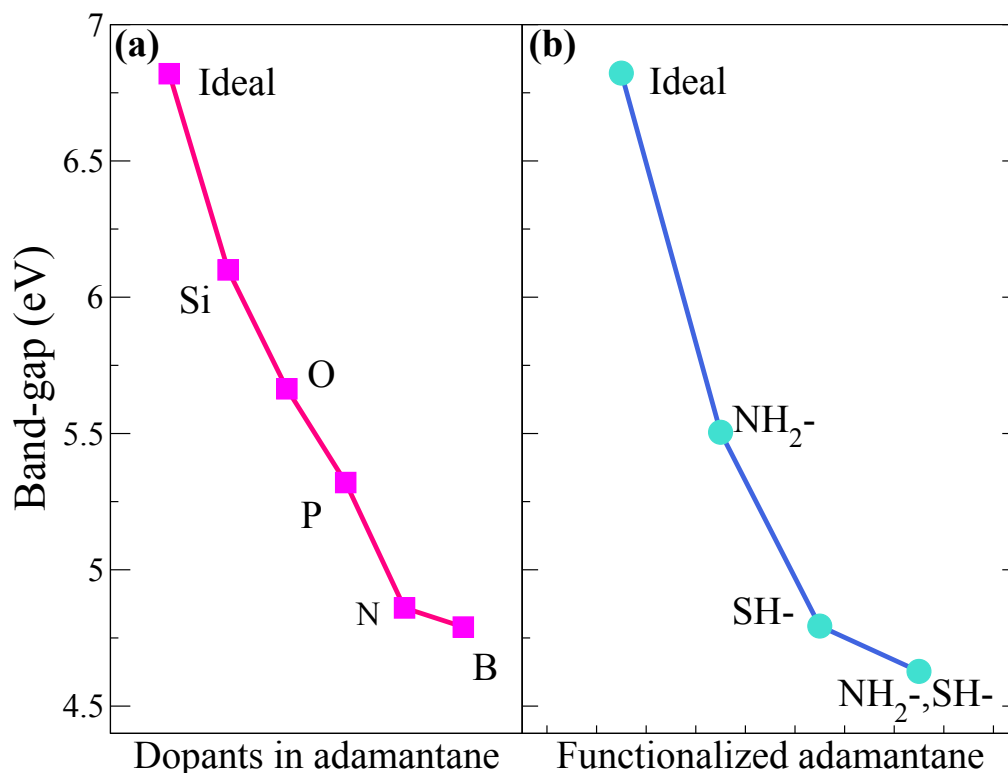


Figure 3.7: Electronic band gaps for (a) doped- and (b) single-, as well as double-functionalized adamantane.

3.2.2 Isomers of tetramantane

In the following, the effect of isomerization in double-functionalized diamondoids is being investigated. As a representative case, the four isomers of tetramantane are being considered. Diamondoids vary in size by the number of diamond cages they include. In tetramantane, four of these diamond-like cages form the diamondoid, producing thereby four different isomers. These isomers are named using the Balaban and von Schleyer notation [1]. This notation depends solely upon the orientation of the respectively bonded diamond cages along their respective axes. According to this notation, different ways of attaching a fourth diamond cage to triamantane exist, leading to the four tetramantane isomers. These isomers are classified as anti-, M skew-, P skew-, isotetramantane and named as [121] tetramantane, M[123] tetramantane, P[123] tetramantane and [1(2)3] tetramantane.

The eDOS of the double-functionalized isomers of tetramantane are summarized in Fig. 3.8 and compared to the ideal tetramantane isomer in each case. The double-functionalized tetramantane molecules include an amine- and a thiol-group as in the respective case of double-functionalized adamantane. The amine- and thiol-groups are attached on the two opposite apical sites of the tetramantane structures. The presence of the functional groups again introduces electronic states in the band gaps of the ideal cases, shrinking the band gap. The HOMO and LUMO states are similarly occupied in the

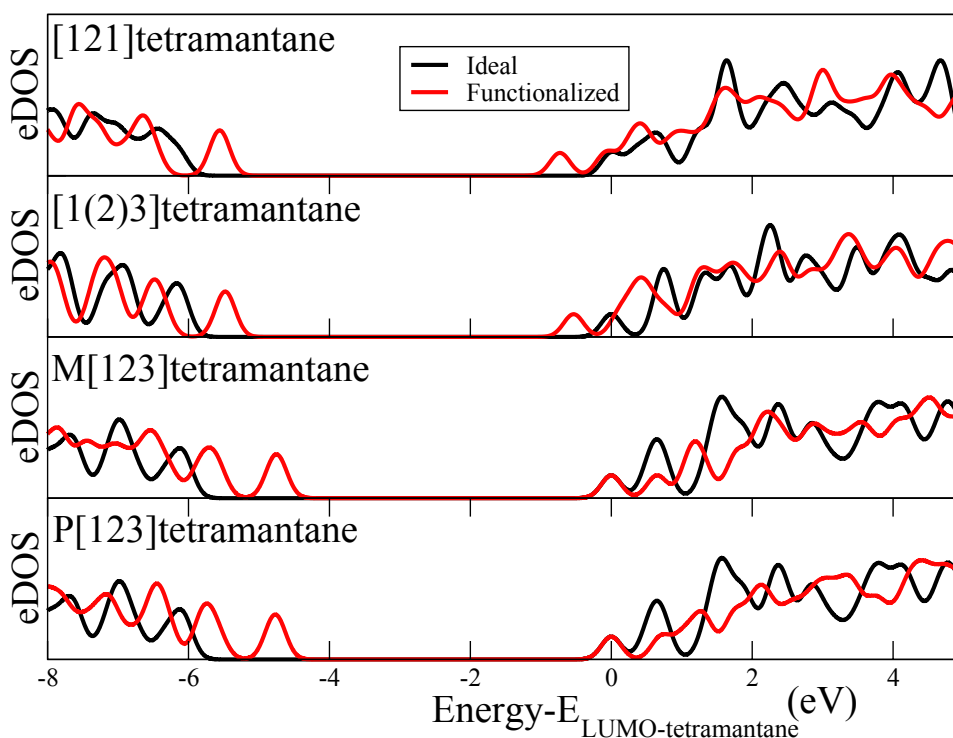


Figure 3.8: The electronic density of states (eDOS) for the ideal and double-functionalized tetramantane isomers. In all panels, the data are shifted with respect to the LUMO level of the ideal tetramantane in each panel, as denoted in the x-axis.

double-functionalized and ideal cases. As expected, the eDOS of the ideal isomers also differ leading to different band gaps for tetramantane in its different isomer structures. In this sense, the relative orientation of the diamond-like cages in these isomers plays a role in defining the band gap and the electronic structure overall. The variation in these band gaps for all isomers, ideal and double-functionalized are given in Fig. 3.9. It is clearly evident that a double functionalization can decrease the band gap approximately 20% compared to the ideal cases. Interestingly, the trend in the band gap variation of the isomers is reversed in the double-functionalized case. [1(2)3] tetramantane has a higher band gap than [121] tetramantane when these are double-functionalized. This order is reversed in the ideal tetramantane cases.

In Figure 3.10, the frontier orbitals (upper panel) and 2D contour plot (lower panel) of all four double-functionalized tetramantane isomers are sketched. These show a clear localization of the HOMO and LUMO on the functional groups denoting an increased role of the functional groups in defining the electronic properties of these structures. Both HOMO and LUMO levels are associated with the thiol group, while only the HOMO is localized at the amine site. Different behaviour of the charge re-distribution over the functionalized surface is observed in the 2D contour plots of the double functionalized tetra-

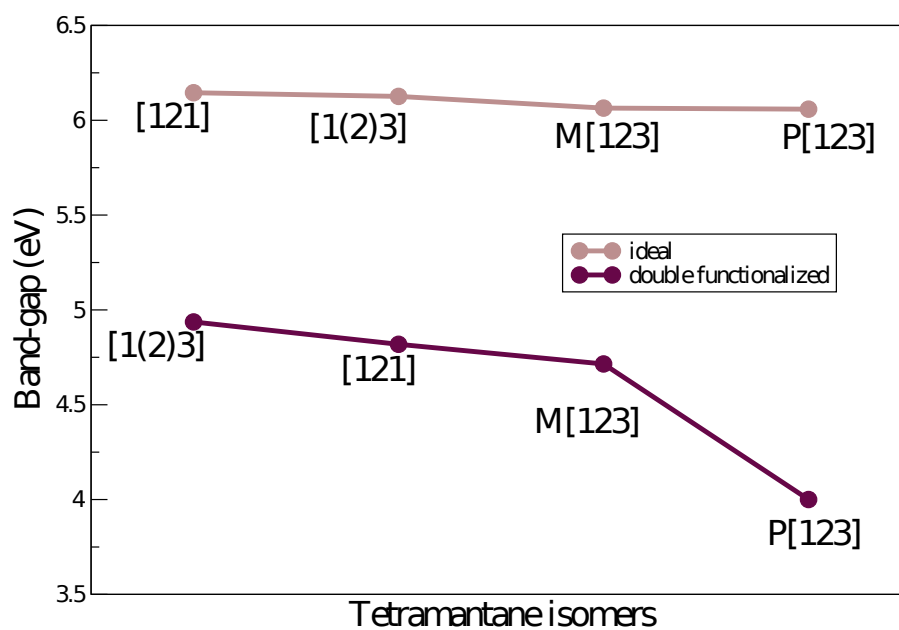


Figure 3.9: The electronic band gaps for the ideal and double-functionalized tetramantane structures as denoted by the labels in the graph.

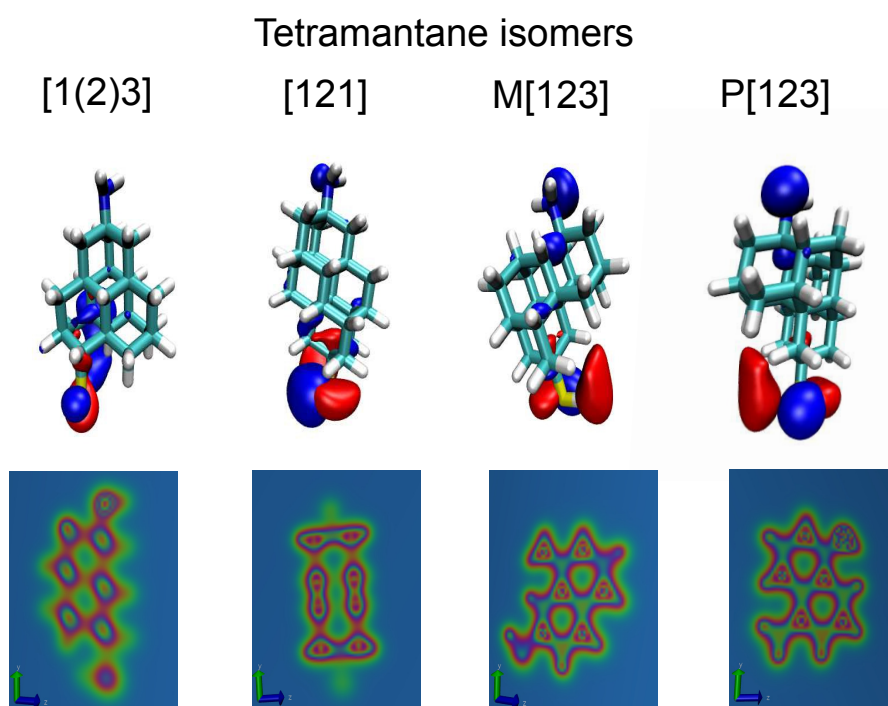


Figure 3.10: The HOMO (in blue) and LUMO (in red) levels (upper panel) and 2D contour density plot (lower panel) of four double functionalized tetramantane isomers are shown.

mantane isomers.

3.2.3 Band gap tuning

In the previous analysis, it was shown that it is possible to alter the electronic properties and tune the electronic band gap of small diamondoids through selective doping or functionalization. A double-functionalization using the amine- and thiol- atomic groups shows a larger decrease in the band gaps moving these closer to the semiconducting region. As a final case, we turn to the effect of the diamondoid size. Accordingly, double-functionalized lower diamondoids from adamantane up to heptamantane are being investigated. In the ideal cases, the band gap decreases with the size, i.e. number of diamond-like cages, as shown in the literature [72] and also confirmed through our calculations (see the upper panel in the graph in Fig.3.11). Again, at this point, the qualitative trend is important and not the exact values of the band gaps. Using a double-functionalization (with an amine- and a thiol group) of these small molecules can further decrease the band gap as evident from the lower panel of the graph in Fig. 3.11. As in the previous sections, both functional groups have substituted a hydrogen atom of the ideal diamondoids on their two opposite apical sites. A comparison of the ideal and double-functionalized cases in

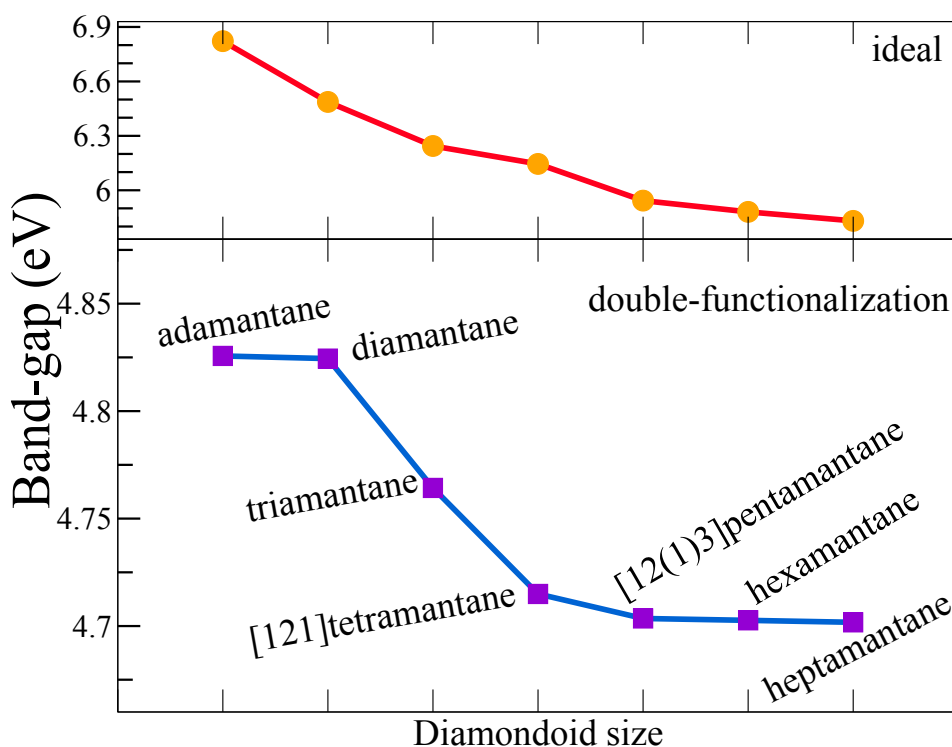


Figure 3.11: The variation of the band gaps for double-functionalized (with a thiol and an amine group) diamondoids with respect to their size (graph, lower panel). For comparison the respective variation for the ideal diamondoids is shown in the upper panel of the graph.

this graph underlines a more abrupt decrease in the latter structures. This de-

crease is more evident moving from double-functionalized diamantane to the double-functionalized pentamantane isomer. The decrease in the band gap with respect to the ideal cases is close to 15% in adamantane and almost 20% in heptamantane. In the ideal cases, the respective relative decrease is 5% and 15%. Nevertheless, the decrease in the band gap in the double-functionalized molecules becomes smoother going from pentamantane to heptamantane. An additional study of higher double-functionalized diamondoids remains to show, whether this trend saturates or not. Note, though, that the variation in the band gap of the ideal diamondoids is larger (a difference of almost 1 eV between adamantane and heptamantane) than in the double-functionalized cases (a respective difference of about 10% of the ideal cases). Finally, a sketch of

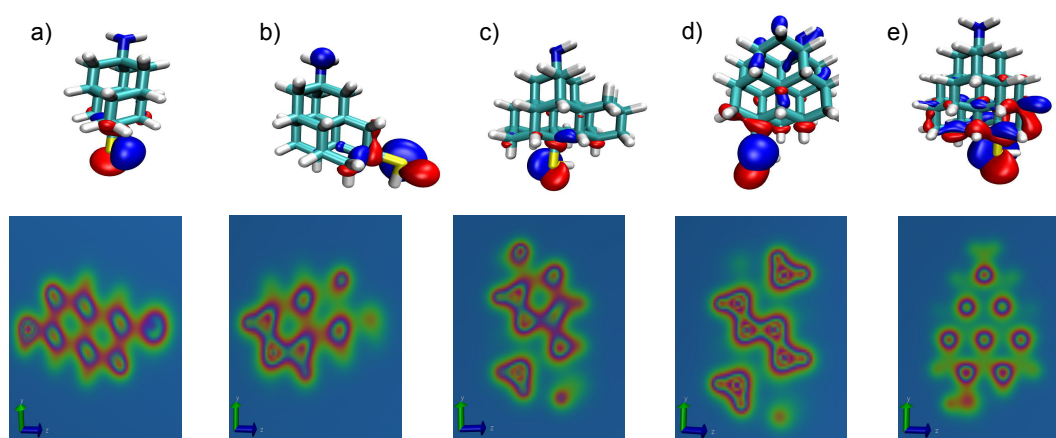


Figure 3.12: In the upper panel relaxed structures for the double-functionalized (a) diamantane, (b) triamantane, (c) [12(1)3] pentamantane, (d) hexamantane, and (e) heptamantane are shown together with their frontier orbitals (HOMO in blue, LUMO in red) are shown. In the lower panel 2D contour of the same systems are depicted.

the frontier orbitals of the double-functionalized diamondoids in Fig. 3.12 (upper panel) and 2D contour plots Fig. 3.12 (lower panel) shows a very strong localization of the HOMO and LUMO at the functionalized sites as opposed to the ideal cases, where the frontier orbitals are more delocalized. The HOMO and LUMO in most of the double-functionalized cases are mainly located on the thiol-group, while no LUMO is associated with the amine group, as also shown in the previous analysis. Accordingly, the thiol group plays a larger role in the electronic properties of these functionalized molecules and could provide a stronger binding site to other structures for practical applications. The eDOS of the double-functionalized diamondoids starting from adamantane up to heptamantane has been summarized in Fig. 3.13. The process of functionalization is the same as discussed in the previous section where the amine- and thiol- groups are attached on the opposite apical sites of the diamondoids. These functional groups influence the electronic properties by inducing electronic states in the band gaps as we increase the number of diamondoid rings. In doing so, the band gap of these higher diamondoids is reduced as compared

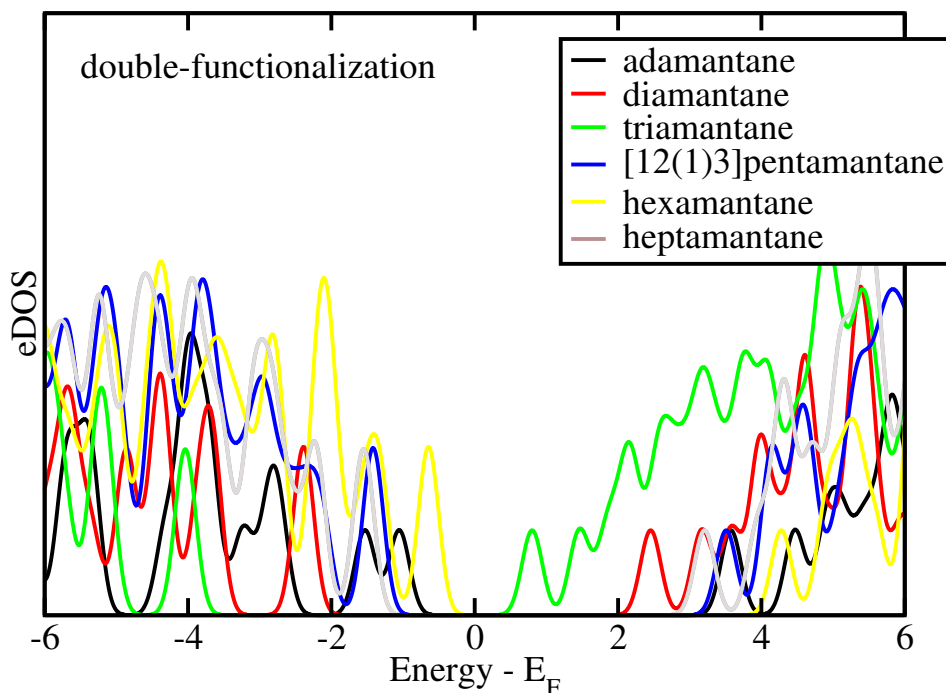


Figure 3.13: The electronic density of states (eDOS) for the double-functionalized higher diamondoids. The Fermi energy is set to zero.

to adamantane. This decrease of the band gap towards the conducting region is a very important attribute in view of its application in potential electronic devices.

3.3 Optical properties of lower diamondoids

In order to unravel the optical properties of ideal, single- and double- functionalized diamondoids, quantum chemical calculations were performed using the Gamess-US [65] quantum chemical software package. Both ground state and excited state geometry optimization were performed under the framework of DFT with a gradient convergence tolerance of 10^{-5} Hartree/Bohr. We use a hybrid functional (cam-B3LYP) [84] with 6-311+G(d,p) basis sets [85] where the diffuse *s* shells were added to hydrogens to describe the exchange-correlation. The hybrid exchange-correlation functional mentioned above uses the Coulomb-attenuation method [86], which is found to be very accurate in the description of the polarizability of long chains, excitations to Rydberg states and charge transfer excitations [87]. All the excited state calculations were performed using the Tamm/Dancoff approximation [88] which compares very well to the full TDDFT calculations.

In view of the nanotechnological applications of diamondoid based complexes, we explore the excitation properties of diamondoids. We compare the optical properties of functionalized diamondoid molecules with their pristine counter-

parts. As previously discussed, thiolated diamondoids have been proven to be promising building blocks for hybrid systems such as SAMs on metal surfaces as a highly effective electron emitting system. We move on to comparatively study the alteration in structure, absorption spectra, and the distribution of occupied and unoccupied molecular orbitals at the first excited state. Furthermore, we also investigate the trends in the optical band gap of these diamondoids as a function of their size and the effect of functionalization. In the end, we discuss the application of these diamondoid-based complexes as potential emission devices.

Results and discussion

As in the ground state S_0 calculations, smallest diamondoids adamantane ($C_{10}H_{16}$) and diamantane ($C_{14}H_{20}$) shown in Fig. 3.14 and Fig. 3.17 respectively, were chosen for functionalization. We study the optical properties as a function of selective functionalization of these two lower diamondoids. We begin with a single functionalization, by replacing one of the hydrogen atoms of the diamondoid with a thiol- (SH-) or amine- (NH_2 -) atomic group. The method of single functionalization and the choice of the site is consistent with the ground state calculations discussed above. At the next step, we double functionalize the diamondoids with both the thiol- and amine-groups. In the single-functionalized diamondoids, the functional (amine- or thiol-) group was attached to an apical site of both adamantane or diamantane substituting the hydrogen atom at that particular site. We have performed simulations for three different functionalization cases: amine-, thiol-, as well as amine-, thiol-functionalized diamondoids along with the ideal cases. For the first two, we refer to single-functionalization, while for the third as double-functionalization. The two substitutional sites for the amine- and thiol-groups are the opposite apical tips of a diamondoid.

We study the stability, structural alterations as well as the effect on the excited state properties of these modified (single-, and double-functionalized) diamondoids in comparison to the properties of ideal unmodified diamondoids as investigated previously in this chapter. The optical properties in all the cases are probed through the frontier orbitals, namely the highest occupied (HOMO) and lowest unoccupied molecular orbitals (LUMO), absorption spectra, as well as the trend in the optical band gaps. The optical band gap is simply the measure of the difference between the HOMO and the LUMO energies derived from the quantum chemical calculations at the first excited state S_1 . We also probe the possibilities of tuning the optical band gap through modifications of the diamondoids using the functional groups mentioned above.

3.3.1 Adamantane

We begin with the structural analysis of all the functionalized adamantane cases depicted in Fig. 3.14 in which the upper panel (a)-(d) represents the

fully relaxed ground state geometries and the lower panel (e)-(h) show the optimized excited state geometries obtained from TDDFT calculations. We can observe a qualitative difference in the structure of ground state and excited state geometries after relaxation. The deviation from the perfect tetrahedral structure is the result of the stretching, shrinking, and tilting of the bonds in a different manner in different systems. In the case of the ideal adamantane, substantial change of the geometry upon excitation is observed where the C-H bond on the apical top slightly deviates towards the left as seen in Fig. 3.14 (a and e).

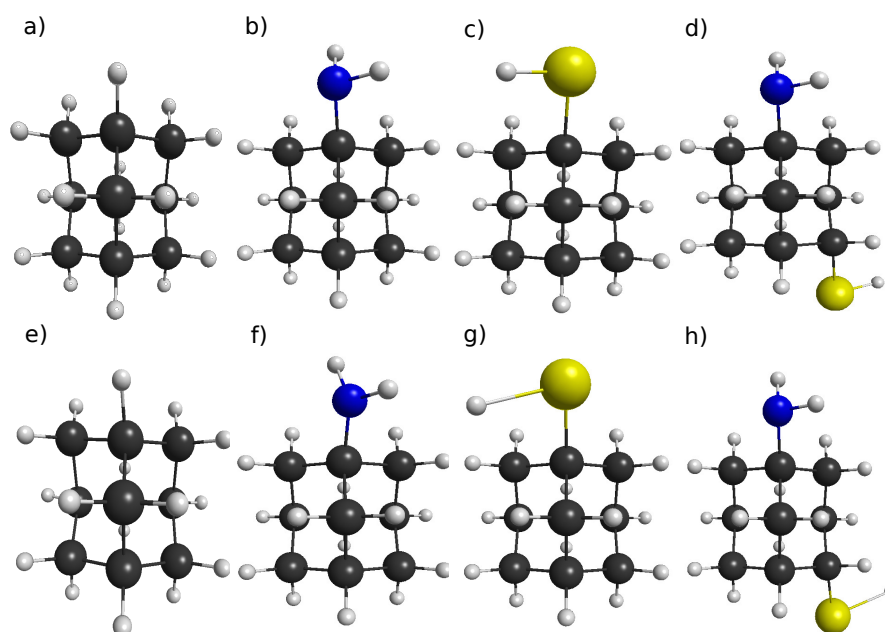


Figure 3.14: The optimized geometries at the ground state S_0 (upper panel) and excited states S_1 (lower panel). Upper panel (a-d) a view of the relaxed ideal view of the adamantane, amine-functionalized adamantane, thiol-functionalized adamantane, and amine+thiol functionalized adamantane are shown. Similarly, the lower panel (e-h) depicts the fully relaxed excited state geometries corresponding to the same system shown in the upper panel. All the simulations are performed within cam-B3LYP level of theory. The C, H, S, and N atoms are shown in black, white, yellow, and blue, respectively.

Quantitatively, the difference in terms of the bond length and bond angle at the ground state and excited state geometries are listed in Table 3.1. For the ideal case, we see that the C-H bond length and the C-C-H angle at the top apical doping site were found to be 1.09 Å and 109.59°. These numbers tend to change at the excited state where the C-H bond length is elongated to 1.13 Å and the C-C-H bond angle also changes to 113.85° which is almost a difference of 4° for the ground and the excited state. For the single functionalization case, we move on to SH- functionalization. We also find considerable changes in the geometries for the functionalized case. The C-S and S-H bonds are elongated to 1.85 Å and 1.88 Å, respectively, which also brings deviation in the H-S-C

Table 3.1: Structural properties of ideal and functionalized adamantane. Bond lengths are given in Å and angles in degrees.

Adamantane		Ground State	Excited State
Ideal	C-H	1.09	1.13
	C-C-H	109.59	113.85
SH-	C-S	1.83	1.85
	S-H	1.34	1.88
	H-S-C	96.74	88.40
	C-C-S	111.20	109.06
NH₂	C-N	1.46	1.41
	N-H	1.01	1.07
	H-N-H	106.65	120.91
	C-C-N	108.67	112.44
SH-,NH₂-	C-S	1.84	1.86
	S-H	1.34	1.88
	C-N	1.46	1.45
	N-H	1.01	1.01
	H-N-H	106.78	106.82
	C-C-N	108.78	108.83
	H-S-C	96.25	84.63
	C-C-S	109.94	114.14

and C-C-S bond angles. These elongations of the bonds at the apical site of the thiolated adamantane compares well with the literature values and indicate weaker bonds which results in lower transition energies [18, 19]. Similarly, in the case of the amine- (NH₂-) atomic group which is the second column of Fig. 3.14 (b and f) we observe the deviation in the C-N bond length decreases to 1.41 Å and the N-H bond length elongated to 1.07 Å at the excited states. H-N-H bond angle is drastically increased from 106° to 120.91° which is an increase of almost 15° as compared to its ground state geometry. In the case of the amine- and thiol- (NH₂-, SH-) atomic groups which are depicted in the two right columns of Fig. 3.14, we see that the S-H bond length has been stretched to 1.88 Å. However, we do not observe any major deviation in the bond length or the bond angle at the amine site for double-functionalization. Bond lengths of C-N, N-H, and the bond angle H-N-H are almost identical to each other on both the ground and the excited state as listed in Table 3.1.

Optical properties

Next, we move on to the optical properties of these modified adamantanes. In order to have a proper understanding of the difference in the electronic structure before and after excitation, we present the HOMO and the LUMO levels as sketched in the second and third column of Fig. 3.15 along with their structures. We know from our previous investigations, that in the ground state,

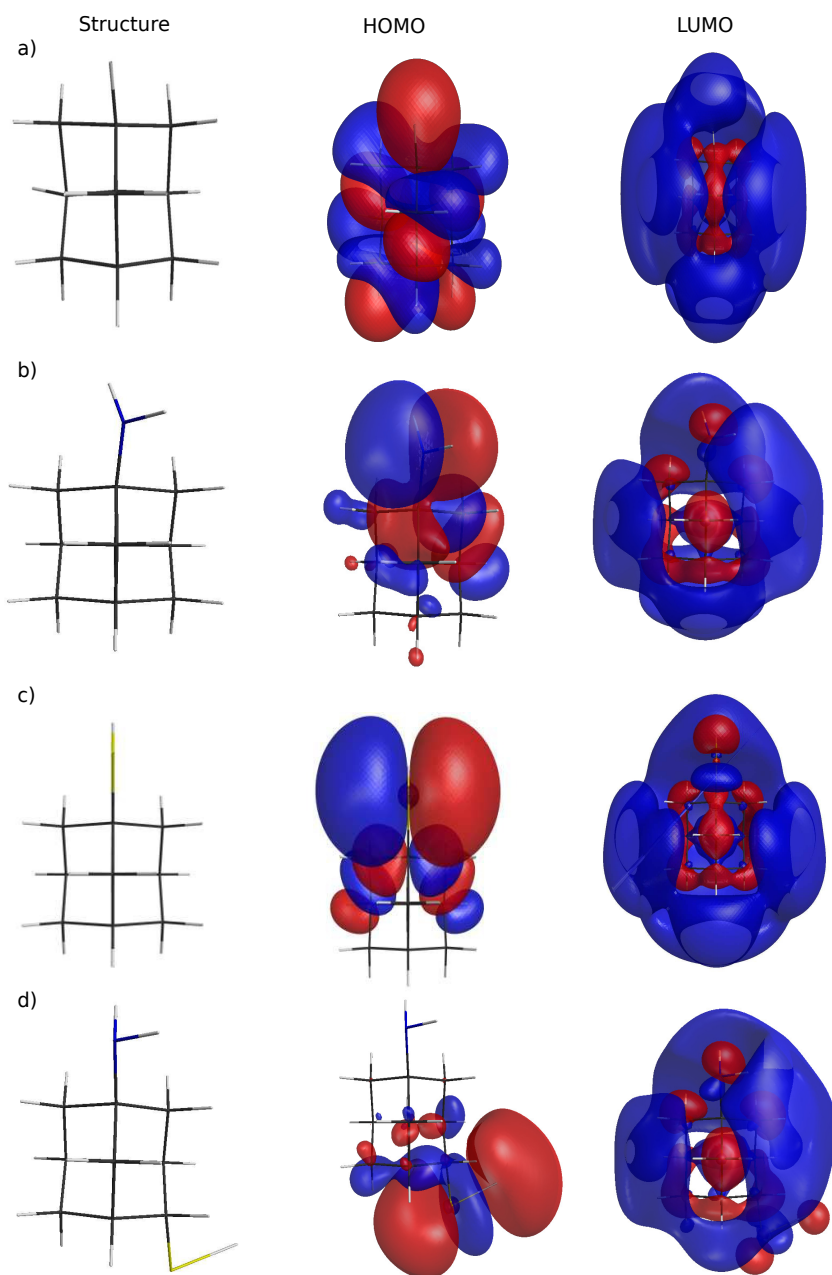


Figure 3.15: Calculated excited state geometrical structures (left column) of the ideal and doped functionalized adamantane and the corresponding iso-surfaces of the HOMO (middle column) and the LUMO (right column). The positive (in red) and negative (in blue) orbitals are shown for an isovalue of 0.013.

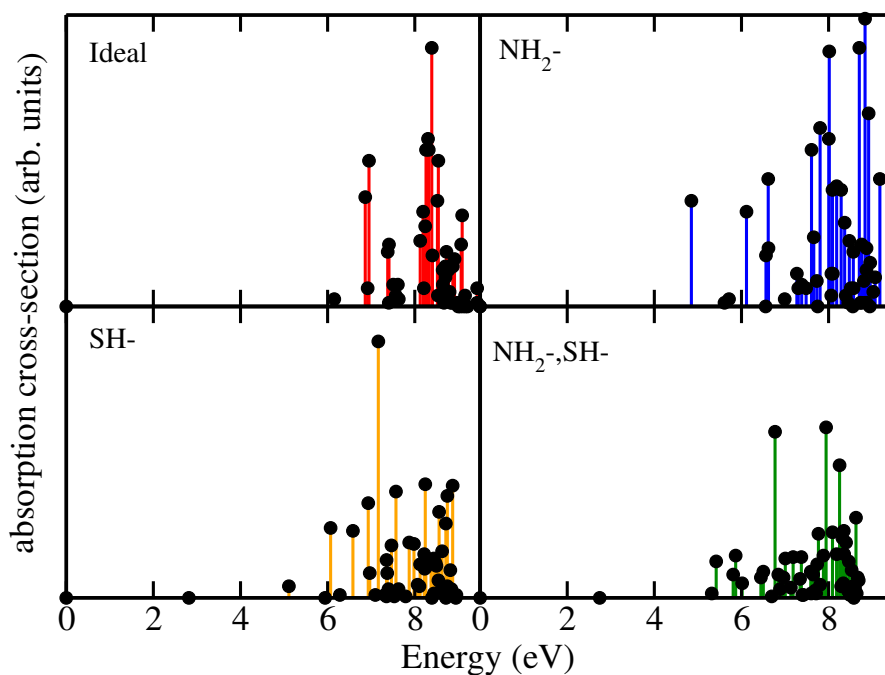


Figure 3.16: Absorption spectra for ideal adamantane (a), amine-functionalized adamantane (b), thiol-functionalized adamantane (c), and amine- and thiol- functionalized adamantane (d) are shown in red, blue, orange, and green respectively. In the x-axis, we have the excitation energies in eV obtained after the TDDFT calculations using cam-B3LYP functional and the y-axis represents the absorption cross-section or the oscillator strength in arbitrary units.

the HOMO states of the ideal adamantane are localized over the C-C bonds whereas the unoccupied states LUMO are more delocalized and spread out over the whole molecule [13]. As per our expectations, these orbitals show slightly different localization in case of the excited state. As we can see in the top-most panel of Fig. 3.15, the occupied orbitals (HOMO) are not confined to just the C-H bond and there is a significant variation in the LUMO states. In accordance with the slight deviation in the bond angle of C-H at the apical site of the ideal adamantane, the LUMOs are altered which results in a slight gap in its spread over the surface. In case of the thiol- (SH-) and amine- (NH_2 -) single functionalized cases (second and third row in Fig. 3.15), the HOMO becomes less delocalized and is concentrated only on the dopant site similar to the ground state orbitals, whereas the gap in the LUMO widens as compared to the ideal case in Fig. 3.15(c).

Similarly, in the case of the double-functionalization, the HOMO is associated with the thiol group as the orbitals are localized more on the thiol functional site than the amine site and the LUMO is associated with the amine functional group as it shows a similar LUMO pattern as seen in the last column of Fig. 3.15(b). The reason behind these differences is the excitation between

orbitals, which also provides the main contribution to the $S_0 - S_1$ transition in adamantane, where S_0 is the ground state and S_1 is the first excited state. These orbitals are symmetric in the ground state, while they get distorted at the fully relaxed excited state. In Fig. 3.16, we show the absorption spectra of the ideal, single, and double functionalized adamantane obtained from the gas phase TDDFT calculations. In the case of ideal adamantane, we can see the first excitation energy at 6.15 eV while the highest peak is at 8.32 eV. Similarly, in amine-functionalized case, the first peak is observed at 4.85 eV with the highest peak at 8.7 eV which lies in ultra-violet (UV) range. These excitation energies are found to shift drastically in case of the thiolated adamantane. In the thiol-functionalized case, the first excitation energy is found to be at 2.81 eV, which lies in the visible range, while in the double-functionalized thiol- and amine- case, it is found to be at 2.74 eV. However, it has to be noted that the first prominent peak for both of these cases are found to be at 5.11 eV and 5.31 eV. The shift in the spectra for different molecules occurs due to different excitation energies. The effect of single- and double-functionalization in the absorption spectra is clearly evident by the shift of these peak points towards the visible region from the UV region.

3.3.2 Diamantane

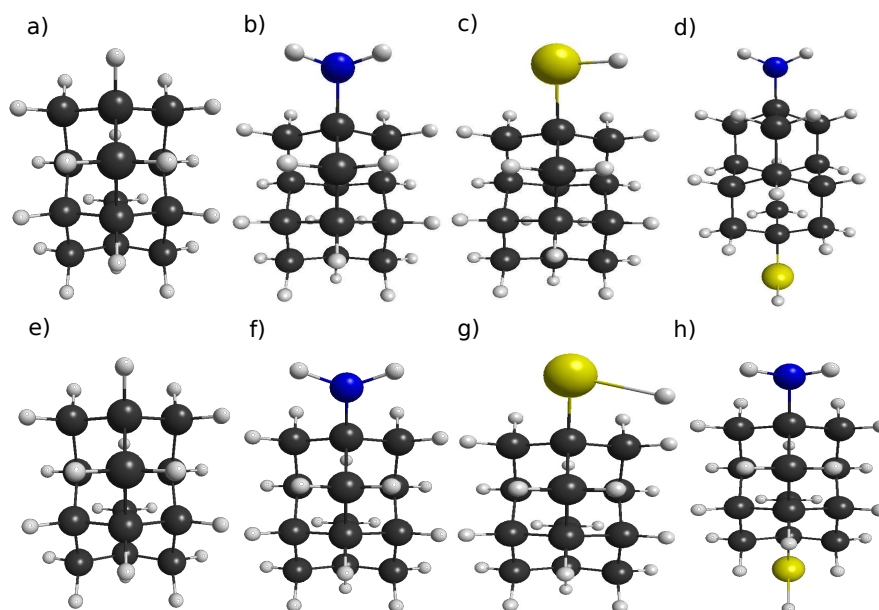


Figure 3.17: The optimized geometries at the ground state S_0 (upper panel) and excited states S_1 (lower panel). Upper panel (a-d) a view of the relaxed ideal view of the diamondane, amine-functionalized diamondane, thiol-functionalized diamondane, and amine-, thiol- functionalized diamondane are shown. Similarly, the lower panel (e-h) depicts the fully relaxed excited state geometries corresponding to the same system shown in the upper panel. All the simulations are performed within the cam-B3LYP level of theory. The C, H, S, and N atoms are shown in black, white, yellow, and blue, respectively.

Table 3.2: Structural properties of ideal and functionalized diamantane. Bond lengths are given in Å and angles in degrees.

Diamantane		Ground State	Excited State
Ideal	C-H	1.09	1.11
	C-C-H	109.70	107.84
SH-	C-S	1.83	1.85
	S-H	1.34	1.90
	H-S-C	96.55	87.70
	C-C-S	106.52	110.82
NH₂	C-N	1.45	1.41
	N-H	1.01	1.07
	H-N-H	106.11	121.00
	C-C-N	108.76	112.45
SH-,NH₂-	C-S	1.83	1.85
	S-H	1.34	1.90
	C-N	1.46	1.46
	N-H	1.01	1.01
	H-N-H	106.76	106.74
	C-C-N	108.77	108.77
	H-S-C	96.81	87.63
	C-C-S	111.40	109.14

Next, we performed TDDFT calculations with diamantane which is a slightly larger molecule than adamantane. Since diamantane comprises of two fused cages of adamantane, it is a symmetric structure resulting in a zero dipole moment. This property of diamantane would affect the excitation behaviour in its ideal state which refers to no functional groups attached to its apical tip. However, the effect of dopants would induce a dipole moment in the structure resulting in interesting characteristic features which are discussed below. First of all, the structural analysis of all the functionalized diamantane cases is depicted in Fig. 3.17 in which the upper panel (a)-(d) represents the fully relaxed ground state geometries and the lower panel (e)-(h) show the optimized excited state geometries obtained by TDDFT calculations. We can observe that there are very qualitative differences in the structure of the ground state and excited state geometries after relaxation in the case of ideal diamantane. A slight deviation in the amine- functionalized case is observed with elongation and tilting of the N-H bonds in the second column of Fig. 3.17(b and f). A substantial distortion is observed in the cases of the thiol- functionalization which is depicted in the third column of Fig. 3.17. The S-H bond length has clearly been stretched. Finally, for the double functionalized case, shown in the last column (d) in Fig. 3.17, we observed distortion in both the amine and thiol sites leading to the deviation of the hydrogen atom from its initial ground state geometry.

Similar to adamantane, we also present the quantitative differences in terms

of the bond length and bond angle at the ground state and excited state geometries for functionalized diamantane. The differences in the bond length and bond angle of the functionalized structures as listed in Table 3.2. For the ideal case, we see that the C-H bond length and the C-C-H angle at the top apical doping site were found to be 1.09 Å and 109.70°. These numbers tend to change at the excited state where the C-H bond length is elongated to 1.11 Å and the bond angle also changes to 107.84°. We notice that the excited state behaviour of diamantane in terms of C-C-H bond angle is not comparable to adamantane. In the case of ideal adamantane, the bond angle was found to be larger at the excited state while for ideal diamantane the C-C-H bond angle tend to become smaller than the ground state. We also found changes in the geometries for the single-functionalized cases. The S-H bond is elongated to 1.90 Å which while the C-S bond also elongates to 1.85 Å which also brings deviation in the H-S-C and C-C-S bond angles. These elongations result in the lower transition energies of modified diamantane [18]. Similarly, in case of the amine- (NH₂-) functionalization, we observe the deviation in the C-N bond length which decreases to 1.41 Å and the N-H bond length gets elongated to 1.07 Å at the excited states which are exactly same as in case of adamantane. H-N-H bond angle is drastically increased from 106° to 121.00° which is again the same as adamantane. In case of the amine- and thiol- (NH₂-, SH-) functionalization, which are depicted in the two right columns of Fig. 3.14, we see that the S-H bond length have been stretched to 1.90 Å. However, we do not observe any major deviation in the bond length or the bond angle at the amine site for double-functionalization. Bond lengths of C-N, N-H, and the bond angle H-N-H are almost identical to each other on both the ground and the excited state.

Optical properties

Next, we move on to the optical properties of modified diamantane molecules. We present the HOMO and the LUMO levels as sketched in Fig. 3.18. Similar to the adamantane cases, the HOMO states of the ideal diamantane are localized over the C-C bonds whereas the unoccupied states LUMO are more delocalized and spread out over the whole molecule [13]. However, in contrast to adamantane, these orbitals do not show any different behaviour in case of the excited state properties. The reason behind this is the zero dipole moment of diamantane, which results in very less distortion of the molecular structure leading to an identical spread of the frontier orbitals in both the ground and excited states. As we can see in the top-most panel of Fig. 3.18, the occupied orbitals HOMO are confined to the C-H bond and the LUMO states spread all over the surface showing no difference between the ground state or the excited state properties. In the case of the thiol- (SH-) and amine- (NH₂-) single functionalized cases (second and third row in Fig. 3.18), the HOMO becomes less delocalized and is concentrated only on the dopant sites, whereas the spread of the LUMO differs from its ideal counterpart in Fig. 3.18(c). Similarly, in the case of the double-functionalization, the HOMO is mostly associated with

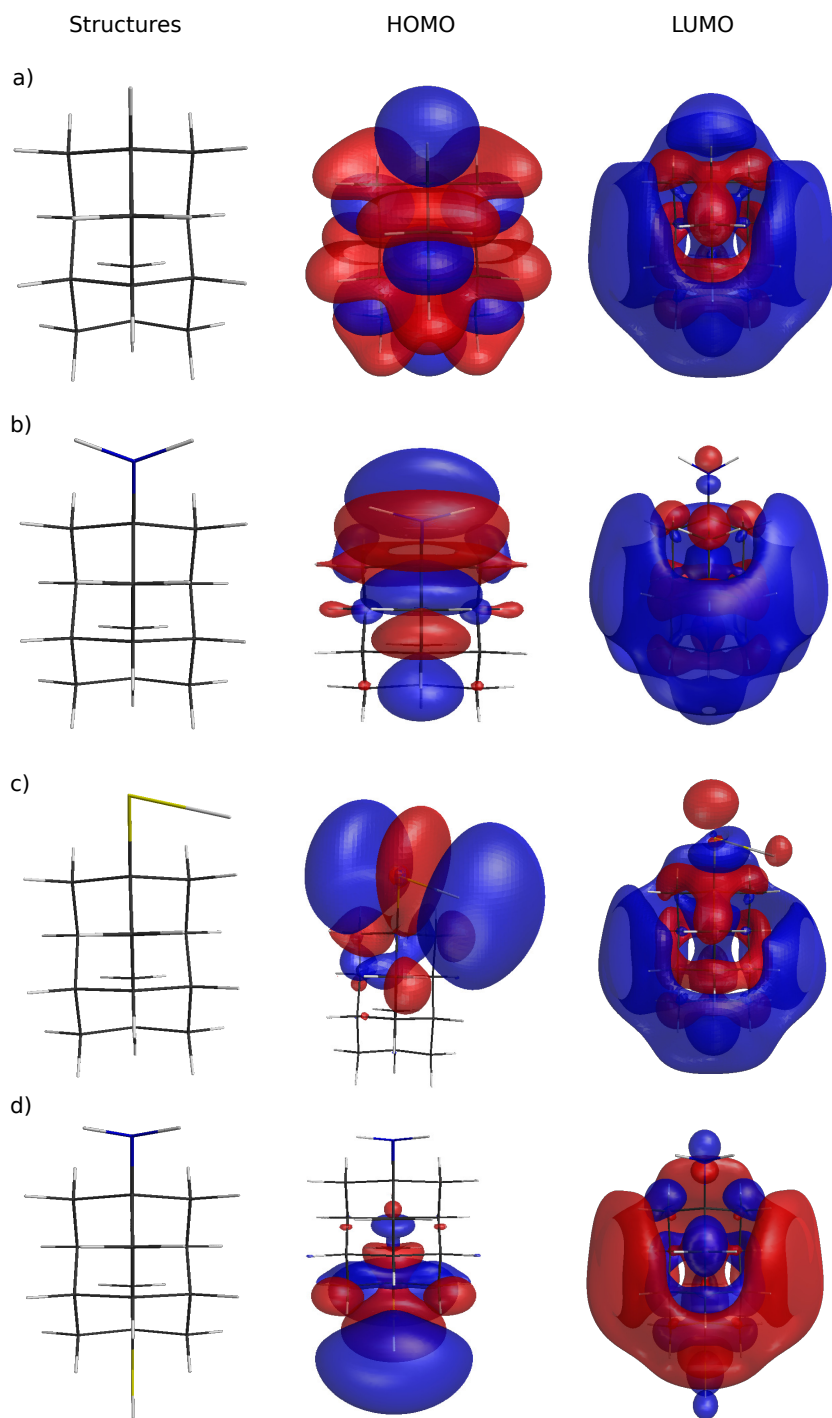


Figure 3.18: Calculated excited state geometrical structure (left column) of ideal and double functionalized diamantane and the corresponding iso-surfaces of the HOMO (middle column) and the LUMO (right column). The positive (in red) and negative (in blue) orbitals are shown for an isovalue of 0.013.

the thiol group as the orbitals are localized mostly close to that. Interestingly, the LUMO pattern in Fig. 3.18(c) is abruptly different as compared to the other single functionalized cases. We can observe the difference in the orbital where the positive (in red) have a larger surface area where the negative (in blue) is diminished. Note that we implemented the same level of theory and methodology for all cases. The reason behind these differences is the excitation between these orbitals which also provides the main contribution to the $S_0 - S_1$ transition in diamantane. These orbitals are symmetric in the ground state while they get distorted at the fully relaxed excited state.

In the next step, we show the absorption spectra of the ideal, single- and double- functionalized diamantane in Fig. 3.19 as obtained from the gas phase TDDFT calculations. In the case of ideal diamantane, we can see the first excitation energy at 6.99 eV. Similarly, in the amine-functionalized case, the first peak is observed at 4.87 eV with the highest peak at 7.8 eV which lies in the UV range. As in the case of adamantane, these excitation energies are found to shift drastically in case of the thiolated diamantane. In the thiol-functionalized case, the first excitation energy is found at 2.78 eV and in the double-functionalized case, the first excitation energy lies at 2.77 eV, which is also in the visible range. However, as observed in the case of adamantane, the first prominent peak for the thiol-functionalized case and the double-functionalized case is observed at 5.03 eV and 5.08 eV, respectively. The shift in the spectra for different molecules is because of the different excitation energies. These results suggest the effect of single- or double- functionalization in the absorption spectra clearly evident by the shift of these peak positions towards the visible region. These results show the other possible functional groups could be used to shift the spectra from the deep UV region towards the visible region.

3.3.3 Optical band gap

In our previous analysis, it was shown that it is possible to alter the electronic properties and tune the electronic band gap of small diamondoids through selective doping or functionalization. As a result, double-functionalization using the amine- and thiol- atomic groups showed a larger decrease in the band gaps moving these closer to the semiconducting region. Similar to that, in this section, we compare the optical band gap of single- and double-functionalized-adamantane and diamantane to its ideal case. The electronic and optical band gap decreases with the size for the ideal cases in both the ground state and excited state cases with the increasing number of cages. The optical band gap corresponds to the energies from $S_0 - S_1$ transitions. For ideal adamantane and diamantane S_1 was found to be 6.15 eV and 6.99 eV, respectively as seen in Fig. 3.20. Note that the optical band gap is generally lower than the electronic band gap (refer to [89, 90]). Although, the increase in the optical band gap of ideal diamantane within the framework of TDDFT has also been observed in the literature [91]. Again, at this point, the qualitative trend is important

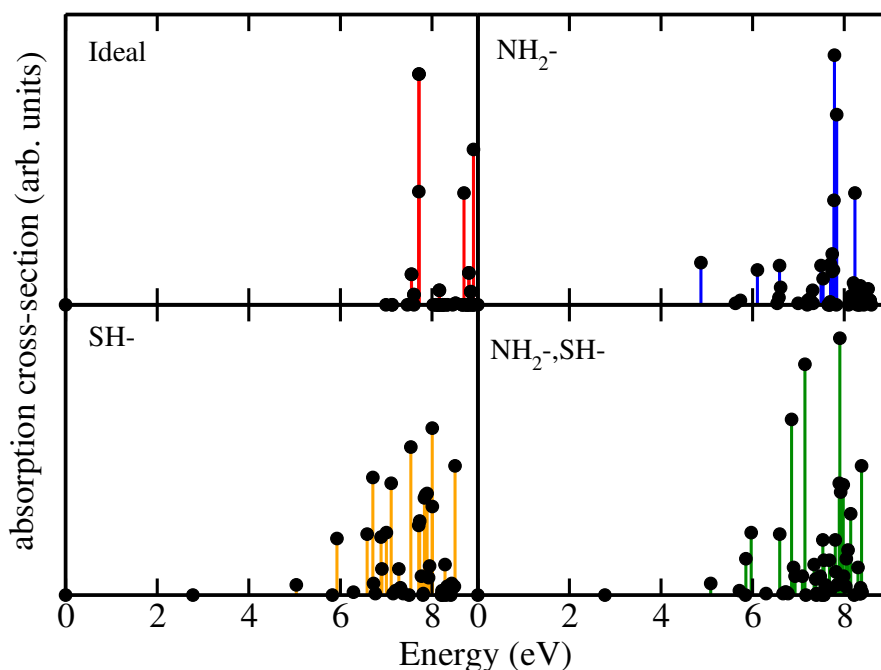


Figure 3.19: Absorption spectra for ideal diamantane (a), amine-functionalized diamantane (b), thiol-functionalized diamantane (c), and amine- and thiol-functionalized diamantane (d) are shown in red, blue, orange, and green respectively. In the x-axis, we have the excitation energies in eV obtained after the TDDFT calculations under the theory of cam-B3LYP functional and the y-axis represents the absorption cross-section or the oscillator strength in arbitrary units.

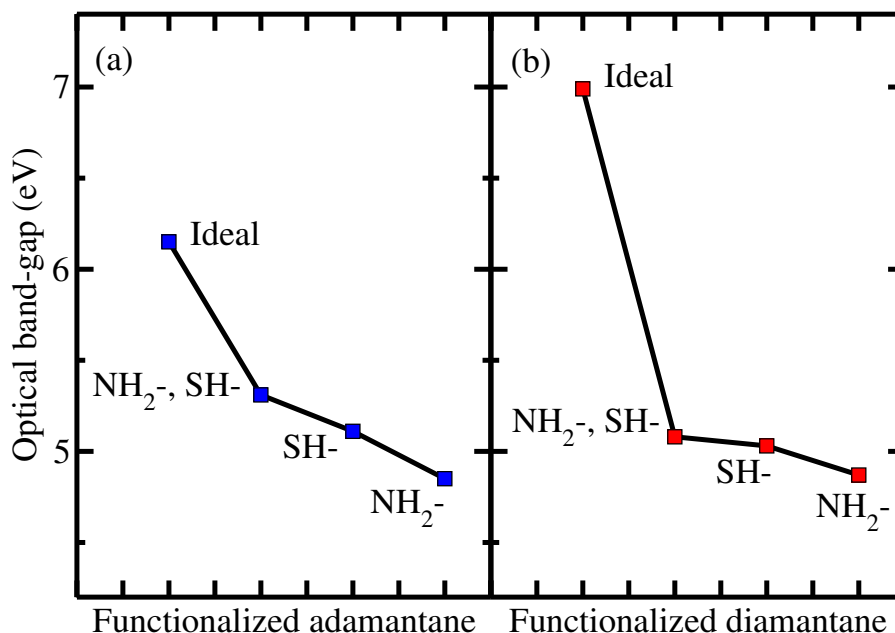


Figure 3.20: The variation of the optical band gaps for single and double-functionalized (with a thiol and an amine group) diamondoids with respect to their ideal cases.

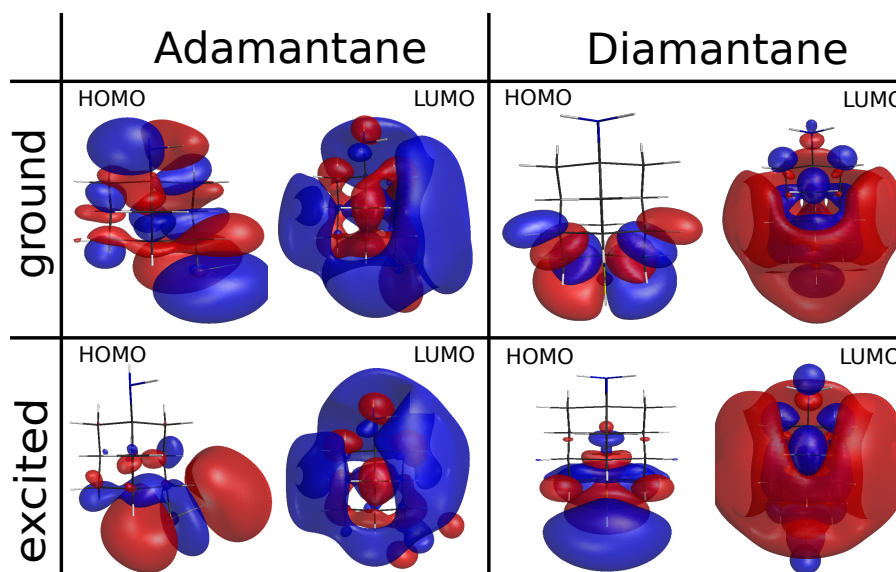


Figure 3.21: Comparison of the frontier orbitals at the ground state and excited state of the double-functionalized adamantane and diamantane. All the simulations are performed within cam-B3LYP level of theory. The positive (in red) and negative (in blue) orbitals are shown for an isovalue of 0.013.

and not the exact values of the band gaps which are quantitatively not well reproduced with the method used. Using a double-functionalization (with an amine- and a thiol-group) of these small molecules can further decrease of the optical band gap.

As evident from the previous analysis, the substitution of an atom in the ideal adamantane with another atom or atomic-group, changes the optical band gap, hence the optical properties, of the functionalized diamondoid molecules. Interestingly, the NH_2 -adamantane and NH_2 -diamantane has an almost same optical band gap (approx. 4.85 eV), which relates to the similar optical properties for both the molecules. For the SH-adamantane and SH-diamantane cases, the optical band gap was found to be 5.11 eV and 5.03 eV which is in reasonable agreement with the experimental optical band gap of thiolated adamantane, i.e 5.85 eV [19]. The double-functionalization also lowers the optical band gap as compared with the ideal cases to 5.31 eV and 5.08 eV. However, these values are higher than the single-functionalized cases. In this respect, an additional functional group would make it possible to further tune the optical band gap of diamondoids in general. Nevertheless, our findings underline the importance of a functionalization for a further shifting of the optical band gap towards the visible region. In Fig. 3.21, we show the frontier orbitals of the ground state and excited state of double- functionalized adamantane and diamantane. As we already know that the localization and delocalization of the HOMO and LUMO over the surface of the molecule plays a very important role in defining their optical properties. As seen in Fig. 3.21, the HOMOs are mostly localized to the thiol group which is at the bottom tip of the functionalized diamantane

while the LUMO spreads all over the surface. We also found out that the interesting functional properties of both the diamondoid molecules are mainly induced by the functional groups rather than the size of diamondoids [18].

3.4 Conclusions

Overall, we have shown the possibility to selectively tune the electronic and optical properties of modified diamondoids through single- and double- functionalization. We found out that different dopants and functional groups lead to different electronic and optical properties. Double-functionalization as compared to a single-functionalization decreases even further the electronic band gap towards conducting region and the optical band gap towards the visible region. Selectively synthesizing diamondoid complexes of a specific size and modification has the potential to tune their electronic and optical properties as molecular devices. In order to probe the possibilities of constructing diamondoid based devices, we discuss the self-assembly of diamondoid based complexes over different metal surfaces in the next chapter.

Chapter 4

Self-assembled monolayers

In this chapter, we analyze the electronic properties of self-assembly of diamondoids on metal surfaces. In section 4.1, we introduce N-heterocyclic carbenes (NHC)s which are emerging as an alternative class of molecules to thiol-based self-assembled monolayers (SAMs), making carbene-based SAMs much more stable in harsh environmental conditions. Next, we present the results and analysis where we have functionalized tiny diamondoids using NHCs in order to prepare highly stable carbene-mediated diamondoid SAMs on metal substrates. We focus on binding characteristics, stability, and adsorption of the NHC mediated diamondoid SAMs on the metal surfaces. The surface morphology of all NHC-based diamondoid SAMs was revealed through simulated STM images, which show characteristic features for each surface. The conclusion of this work is summarized in the final section 4.3. Some of the sections of this chapter are also the part of our published article "B. Adhikari, S. Meng and M. Fyta, *Nanoscale*, 2016, 8, 8966 - Reproduced by permission of The Royal Society of Chemistry. All rights reserved".

4.1 NHC mediated diamondoids

N-heterocyclic carbenes [92] are the ring-like structures made up of carbon and nitrogen. One of the simplest forms of carbene is Imidazolyliene which is shown in Fig. 4.1. Unlike typical carbene molecules, which are highly reactive and have very limited stability, NHCs usually have two hetero-atoms adjacent to the carbene carbon. The partial aromaticity at the backbone of the carbene ring is another reason for its high stability. In addition, NHCs can be prepared on the industrial scale, can be crystallized, distilled, and stored for long period of time in order to become commercially available reagents [93–95]. Bulky NHC ligands have also theoretically been shown to stabilize the main group compounds [96]. In the past, thiol-based SAMs on metal surfaces have led to significant applications in the field of surface emission, sensing, electrochemistry, drug delivery, and microelectronics [21–25]. However, thermal instability of these thiol-based SAMs on gold in harsh environmental conditions has been a huge hindrance in using them for industrial purposes [26–30]. Thiol-based SAMs are found to be stable only when stored in an ultra high

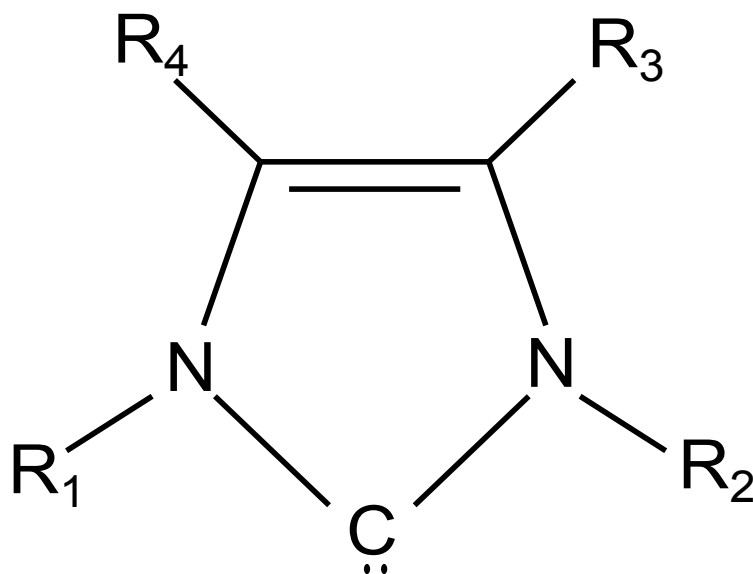


Figure 4.1: General structural formula of imidazolylidene-structures

vacuum in the absence of light but tend to degrade after few weeks at room temperature [31–33]. Accordingly, an alternative molecule which mediates the formation of diamondoid SAMs on substrates is needed. For this, we propose the use of N-hetero-cyclic carbene (NHC) molecules to promote binding of diamondoids on metal surfaces. This feature increases the NHC stability. In this work, we aim to study the structural and electronic properties of carbene-functionalized diamondoid monolayers on metal surfaces. For the latter, we consider gold, silver, and platinum surfaces. We also study their morphology and work function in view of their nanotechnological applications as potential electron emitters and sensors.

4.2 Diamondoid mediated SAMs

The smallest diamondoid adamantane ($C_{10}H_{16}$) was chosen to model a free radical self-assembled monolayer absorbed on the metal substrates. Two variations of carbene molecules were chosen and attached to adamantane to prepare two different diamondoid SAMs, namely ($C_{13}N_2H_{18}$) and ($C_{23}O_1N_2H_{32}$) [97]. To these, we refer in the following as NHC1, and NHC2, respectively. The former is chosen on a purely theoretical basis, while the latter has already been used in experiments. We chose both as representative carbene candidates in order to extend the search for potential carbene-mediated diamondoid-based SAMs. ($C_{23}O_1N_2H_{32}$) has been investigated experimentally and ($C_{13}N_2H_{18}$) is a molecule with less complexity and could be easier manipulated. Before structural relaxation, the NHC-mediated diamondoid-SAMs were placed on the on-top site of the surfaces and at a distance larger than 2.20 Å. Preferential site binding of the NHC2 on the surfaces is not considered in this work taking into account the experimental evidence that the lowest carbene-C atom (for NHC2) is bonded on the on-top site on an Au(111) surface [97]. Our

initial calculations also showed that the on top site is also preferred by the NHC1-mediated adamantane. Two different molecules chosen to self-assemble on the metal surfaces are shown in Fig. 4.2. The figure shows adamantane functionalized with the carbene molecules NHC1 and NHC2. In the following, we refer to these functionalized diamondoids as NHC1-ada and NHC2-ada, respectively. The notation NHC-ada/metal (or modified metal surfaces) refers to the NHC-mediated adamantane SAMs on one of the metal surfaces.

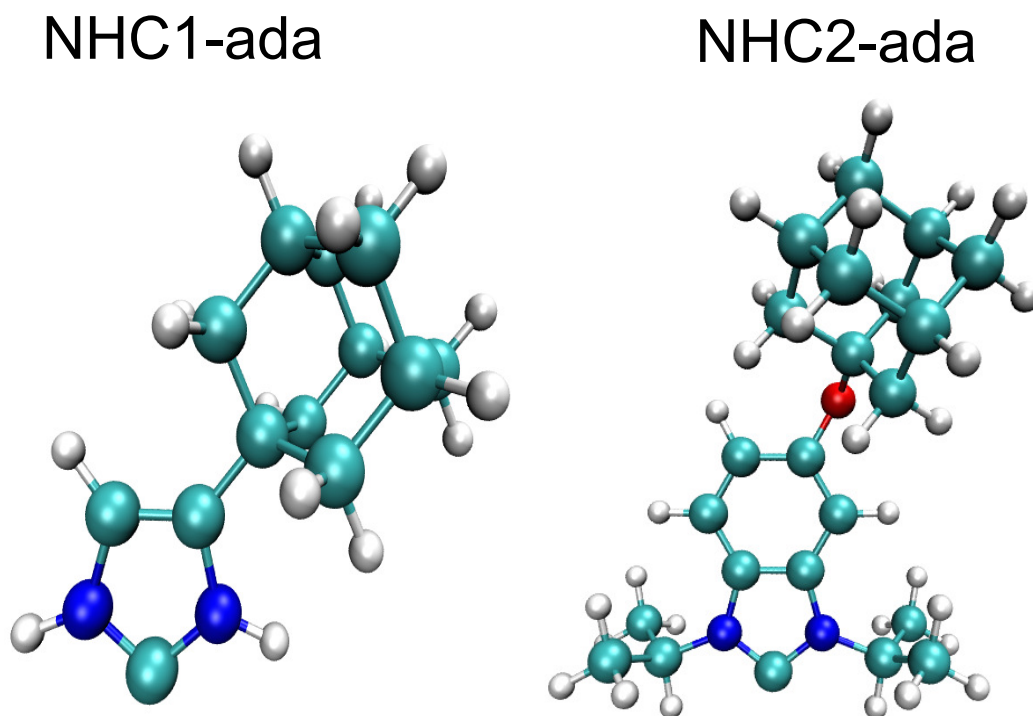


Figure 4.2: The NHC1-functionalized adamantane (left) and the NHC2-functionalized adamantane (right).

4.2.1 Structural analysis

We begin the discussion with the analysis of the structural characteristics of all carbene-mediated diamondoid surfaces. All structurally relaxed SAMs are depicted in Fig. 4.3. The distance of the carbene-functionalized diamondoid from the surface is also denoted by the arrows which is calculated based on the bond-length of the lowest carbon atom of the carbene-functionalized diamondoid to the closest metal atom of the surface. We observe a variability in the 'C-metal' bond-length for the different molecules and metal surfaces in the range of 1.97 - 2.28 Å. An overall closer arrangement is evident for the diamondoid-SAMs on Pt(111), followed in trend by the diamondoid-SAMs on Au(111) evident due to the shorter bond (1.97 Å for the NHC1-ada case and 2.02 Å for the NHC2-ada case) of the functionalized diamondoid with the Pt surface. For the Au(111) surface, these values are 2.08 Å for NHC1-ada and 2.12 Å for NHC2-ada. As discussed in the literature [97], despite various

NHC structures are available, the C/N ratios for the films and nanoparticles investigated using X-ray photoelectron spectroscopy (XPS) were compared to previous experimental studies and were found to be optimal for the NHC with the C_3H_7 ligand. The NHC coverage for this case was also found dense enough to prevent other impurities from binding to other sites not covered by the NHC. This is the same molecule (NHC2) we chose in our investigations due to the previous experimental evidence. As implied in the introduction, the family of NHC molecules can assume a number of variations, other than the C_3H_7 . Additional ligands have not been investigated here. The aim of this work was not an extensive study of such ligands and NHC members, rather provide a proof of principles of the efficiency of such molecules in promoting the binding of diamondoids on metal surfaces in order to form self-assembled layers of diamondoids. The larger bond-length in both Ag SAMs is an indication of a less stable SAM, which will be further evaluated in the following. For the Ag surface, the respective bond lengths are 2.19 Å for NHC1-ada and 2.28 Å for the NHC2-ada case. The shorter bonds of the diamondoid-SAMs on Au(111) and Pt(111) denote a stronger bonding compared to the Ag(111) surfaces. In

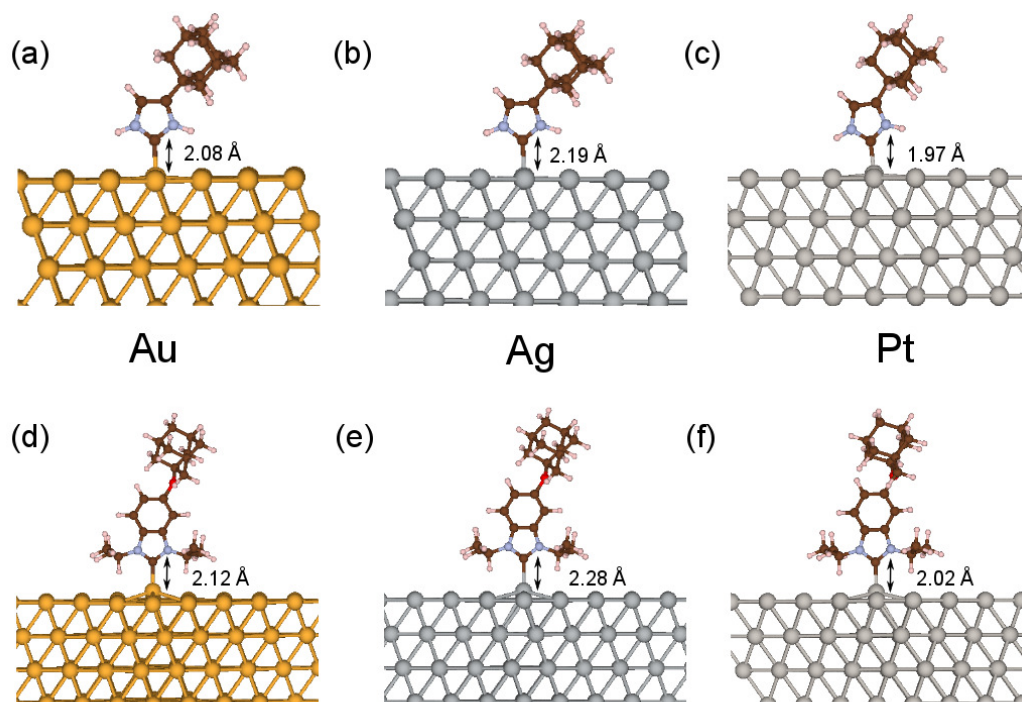


Figure 4.3: (a)-(c): adsorption of the NHC1-mediated adamantane SAMs on Au(111), Ag(111), and Pt(111), respectively. (d)-(f): adsorption of the NHC2-mediated adamantane SAMs on the same surfaces. The black arrows indicate the C-metal bond-lengths in each case.

the case of NHC2-ada, two of the hydrogen atoms of the carbene molecule come close to the metal surfaces. Note, that these H atoms are all bonded to secondary C atoms in the ligand. One of these secondary C atoms is bonded to the N atom of the carbene ring. The distance of the H atom bonded to

the secondary C atom (close to the nitrogen) and the metal surface was found to be 2.86, 2.80, and 2.05 Å for the Au, Ag, and Pt surfaces, respectively. In the case of Pt(111), these distances are quite small indicating that two of the hydrogen atoms attached to a secondary carbon atom of the carbene C₃H₇ ligands could also bind to the metal surface. This will be confirmed by the HOMO re-distribution analysis below. The distance of the H atoms bonded to the other two secondary C atoms in the ligand which is closest to the metal is 3.18, 3.22 and 3.11 Å for H-Au, H-Ag, H-Pt, respectively. For the NHC1-ada case, the distances of the lowest hydrogen atoms of the carbene ring are 3.32, 3.16, and 2.75 Å for H-Au, H-Ag, and H-Pt, respectively. Another important structural detail is the relative orientation of the adsorbed NHC-adamantane with respect to the metal surfaces. Close inspection of all structures in Fig. 4.3 reveals that for each NHC-ada its vertical arrangement with respect to all three surfaces is almost the same. In order to prove this, we have calculated the angle between the carbene carbon atom which is closer to the surface (the one involved in the 'C-metal' bond mentioned above), the closest metal atom and one of its nearest neighbors. These angles lie in the range 93-96° for NHC1-ada and 100-106° for NHC2-ada for all three surfaces. The values denote an orthonormal arrangement of the carbene-mediated adamantane-SAMs on the metal surfaces which is observed for both NHC1-ada and NHC2-ada. In the latter case, though, and for all three metal surfaces, the metal atom bonded to the carbene-functionalized adamantane was slightly pulled off the metal surface in order to stronger bond to the molecule. Hence, the respective angles are about 10° larger than for NHC1-ada. This higher "attraction" of the closest metal atom from the NHC2-ada was also reported in a relevant experimental work [97]. This behavior was not observed for the NHC1-ada case on any of the surfaces. The most important structural characteristics for the NHC-mediated adamantane-SAMs investigated here are summarized in Table 4.1.

4.2.2 Adsorption Energies

In order to assess the quality of the SAM binding on the metal surfaces, we investigate adsorption energies. The adsorption energy E_{ads} , for a molecule adsorbed on a surface is the difference between the total energy of the molecule/metal system (E_{total}) and the sum of the total energies of the two components. This sum includes the total energy of the clean metal surface (E_{clean}) and the total energy of the isolated molecule (E_{mol}). The following equation holds for the adsorption energy:

$$E_{ads} = E_{total} - E_{clean} - E_{mol} \quad (4.1)$$

The adsorption energies for both NHC-ada on the gold and platinum surfaces are found in the range -1.70 to -1.92 eV. Accordingly, no significant qualitative difference in their stability can be inferred for these cases. For the silver surfaces, these energies are about 30-45% higher compared to the NHC-ada adsorption on gold and platinum. In this respect, the SAMs can be easily formed

Table 4.1: Structural properties and adsorption energies (E_{ads}) for the carbene-mediated diamondoid SAMs on metal surfaces depicted in Fig. 4.3. Energies are given in eV, angles in degrees, and bond-lengths in Å.

SAMs		NHC1-ada	NHC2-ada
Gold (111)	E_{ads}	-1.819	-1.700
	C-Au	2.08	2.12
	C-Au-Au	95	103
	H-Au	3.32	2.86
Silver (111)	E_{ads}	-1.190	-1.067
	C-Au	2.19	2.28
	C-Au-Au	96	105
	H-Au	3.16	2.80
Platinum (111)	E_{ads}	-1.843	-1.921
	C-Au	1.97	2.02
	C-Au-Au	93	100
	H-Au	2.75	2.05

on Au(111) and Pt(111) than on Ag(111). The fact that for the same metal surface, both SAMs lead to similar adsorption energies, can be understood as a similar efficiency of the metal surface in adsorbing both the NHC1- and the NHC2-functionalized adamantane. This similarity is evident despite the fact that NHC1-ada does not contain the C_3H_7 ligand attached to nitrogen as in the NHC2-ada case. The stability of NHC2-ada has already been observed experimentally revealing the practical interest of NHC2-ada SAMs [97]. Accordingly, due to the similarity in the adsorption energies, we can argue that the theoretical molecule NHC1-ada considered here could be an additional potential candidate in forming carbene-mediated SAMs on metal surfaces. All adsorption energies as calculated through Eq.4.1 are summarized in Table. 4.1. According to the above analysis, the bonding of the carbene-mediated diamondoid-SAMs on metal surfaces is stronger compared to thiol-mediated diamondoid-SAMs on the same surfaces. Specifically, our calculations lead to longer bonds in the latter case. For thiol-functionalized adamantane molecules, the S-Au, S-Ag, S-Pt bond-lengths (which correspond to the SAM-surface bonding) were found to be 2.56, 2.55, and 2.33 Å, respectively. The respective adsorption energies are -2.16, -2.18, and -3.15 eV, respectively. At a first sight, these denote a better adsorption of sulfur-bonded adamantane on the metal surfaces. For thiol, the preferred adsorption site on the metal surfaces is the fcc site, while for the NHC-ada the preferred adsorption site is the on-top site. This is confirmed by our initial calculations and experiments [98].

According to recent theoretical investigations, DFT simulations with common GGA functionals incorrectly favor adsorption sites with a high coordination, such as the fcc site, rather than a low coordination site, such as the on top site [99]. Note, that though the fcc site for thiol-mediated adsorption is preferred in the experiments [98], the DFT-derived adsorption energies for the fcc site

have not always been in good agreement with experiments. This was evident in the case of CO adsorption on Pt(111) [100]. Due to this possible discrepancy between experimental and theoretical data on the preferable binding sites, we focus on the comparison of bond lengths rather than binding sites. Accordingly, we compare the bond lengths between the S-mediated and NHC-mediated SAM adsorption on the metal surfaces. These bond lengths are significantly shorter in the latter case and differ about 11-19% between the two cases. This finding indicates a stronger bonding of the NHC-diamondoid SAMs than thiol-diamondoid SAMs on the metal substrates.

4.2.3 Isolated NHC-functionalized adamantane

For the analysis of the electronic properties of the structures studied here, we begin with the projected electronic density of states (PDOS) and the frontier orbitals of the free-standing (no metal surface) carbene-functionalized adamantane. The latter are the highest occupied (HOMO) and lowest unoccupied molecular orbitals, HOMO and LUMO, respectively. The charge density of the frontier orbitals of the free standing SAMs was sketched in Fig. 4.4. We observe that the charge density for the HOMO is quite delocalized over the whole molecule, including the adamantane and NHC parts (for both NHC1 and NHC2). On the other hand, the charge density for the LUMO is more localized on the carbene ring and the lower N-C-N atoms, the tip of the carbene ligand. This ligand promotes binding of the molecule to the metal surface. These features differ from the ideal adamantane case, as expected. For the ideal adamantane, the charge density for the HOMO is localized in between the carbon-hydrogen bonds and the charge density for the LUMO is delocalized and spread out over the molecule's surface [101]. The respective PDOS of the isolated NHC-ada molecules shown in Fig. 4.5 are considerably altered by the presence of the carbene as compared to the ideal adamantane [101]. For both molecules, the s-orbitals contribute more to the electronic density of states in both the HOMO and the LUMO levels. A comparison of both carbene variations, NHC1 and NHC2, reveals that the s- and p- distributions in the PDOS are similarly broad. The functionalization introduces electronic states in the band gap of the ideal adamantane, decreasing in this way the electronic band gap of carbene-functionalized adamantane. This band gap reaches 3.62 eV for NHC1-ada and 3.37 eV for NHC2-ada which is a decrease of almost 50 % compared to the value for ideal adamantane [101]. Note, that the results for the electronic band gaps were obtained with DFT without any correction for the band gap calculation. Accordingly, these values are expected to be off with respect to experimental values. However, our simulations can capture the trends in the modification of the electronic band gap due to the carbene-functionalization and this trend is of interest here.

Adamantane modified metal surfaces

The adsorption of the NHC-ada molecules on the metal surfaces alters the electronic properties of the clean surfaces and the isolated NHC-ada. The

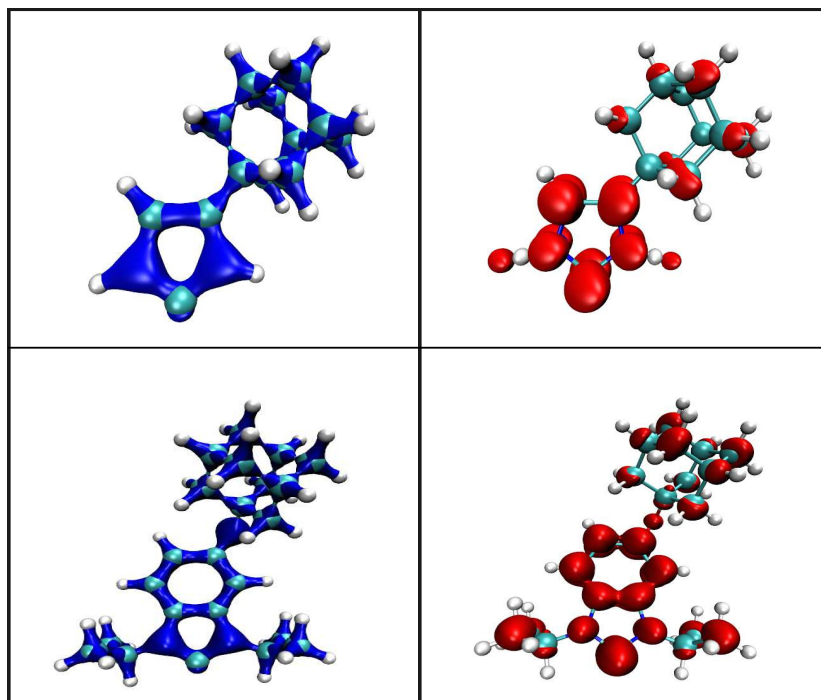


Figure 4.4: The charge density of its highest occupied molecular orbital (HOMO) (top-left; in blue), and the charge density of the lowest unoccupied molecular orbital (LUMO) (top-right; in red) are shown. Charge density of the HOMO (bottom-left; in blue), and that for the LUMO (bottom-right; in red) are also given.

electronic features of the adsorbed SAMs mapped through the PDOS are shown in Fig. 4.6 and reveal the qualitative influence of the SAM adsorption of the surfaces. For all substrates, we observe that the HOMO of the molecule is slightly shifted towards the Fermi energy which indicates the bonding to the surface. The occupied levels become more spread out. The unoccupied levels become less peaked and slightly more broad for the adsorbed molecules. The trend in the height of the peaks in the p-orbital contribution for the occupied electronic levels is altered in the adsorbed cases, as the third peak before the Fermi energy is more pronounced compared to the fourth peak in the non-adsorbed cases. This again denotes the tendency to 'move' the electronic levels in order to promote binding to the surface. According to the total density of states shown in Fig 4.7, all occupied electronic levels enter the band gap region of the free standing carbene-functionalized adamantane before adsorption. In order to reveal the binding characteristics and the reactivity of the metal surfaces, we calculated the PDOS of the first layer of the metal substrates and the PDOS of the carbon atom of the carbene ring which is the closest and binds to the surface. For a better qualitative understanding of the nature of bonding and the hybridization of the electrons, the contributions with respect to the angular momentum (s-,p-, and d-orbitals) in the PDOS are plotted in Fig. 4.8. A covalent bond between the molecule and the surface can be formed when d-orbitals are contributing more to the density of states

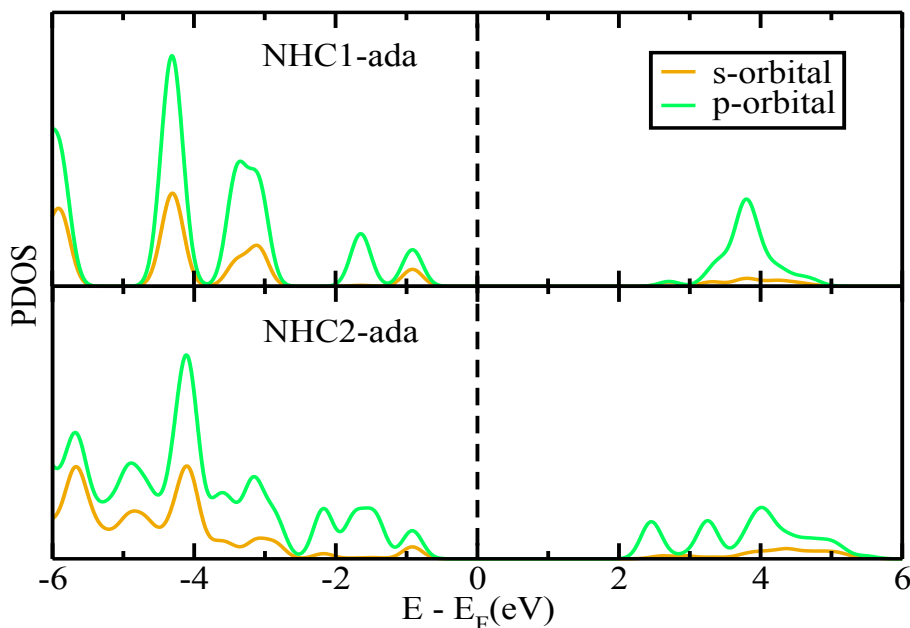


Figure 4.5: Projected density of states (PDOS) for both carbene-functionalized adamantane molecules before adsorption. The contributions from the s- and p-orbitals are depicted in black and red, respectively. The Fermi energy in each case was shifted to 0 eV.

near the Fermi energy. In such a case, the p-electrons of the molecules can coordinate with the hybrid orbitals of the metal surface and promote bonding of the two structures. Inspection of the left panels in this figure reveals that the contribution of the d-orbitals in the PDOS for the first layer of the Au and Pt surfaces at the Fermi level is very large compared to the respective contributions of the s- and p-orbitals. The contributions of the carbene carbon atom in the PDOS (right graphs in each panel of Fig. 4.8) reveals a peak in the p-orbital contributions around the Fermi energy. Accordingly, the p-orbitals of the lowest carbene atom are available to overlap with the d-orbitals of the metal and share electrons to form bonds. The overlapping is not so evident in Ag(111); a difference possibly assigned to its higher reactivity compared to gold and platinum. Since the p-orbital contribution to the PDOS for the NHC1-ada/Au and the NHC2-ada/Pt is more peaked at the Fermi level, it can be inferred that the bonding in these two cases should be slightly stronger compared to NHC2-ada/Au and NHC1-ada/Pt. For the latter structures, the p-orbital contribution of the carbene-C atom is slightly off the Fermi level. This is in agreement with the shorter C-Au bond for NHC1-ada/Au compared to NHC2-ada/Au in Table 4.1. For Pt(111), though, we see a reverse behavior: the p-orbital contribution for NHC2-ada/Pt is peaked exactly at the Fermi level, but the C-Pt bond according to Table 4.1 is 2% longer than in NHC1-ada/Pt for which the p-orbital contribution in the PDOS shows a peak slightly off the Fermi level. Nevertheless, the adsorption energy for NHC2-ada/Pt is 4% higher than in NHC1-ada/Pt, denoting stronger adsorption in the former case. A possible explanation lies in the existence of the C_3H_7 ligand in NHC2-ada and

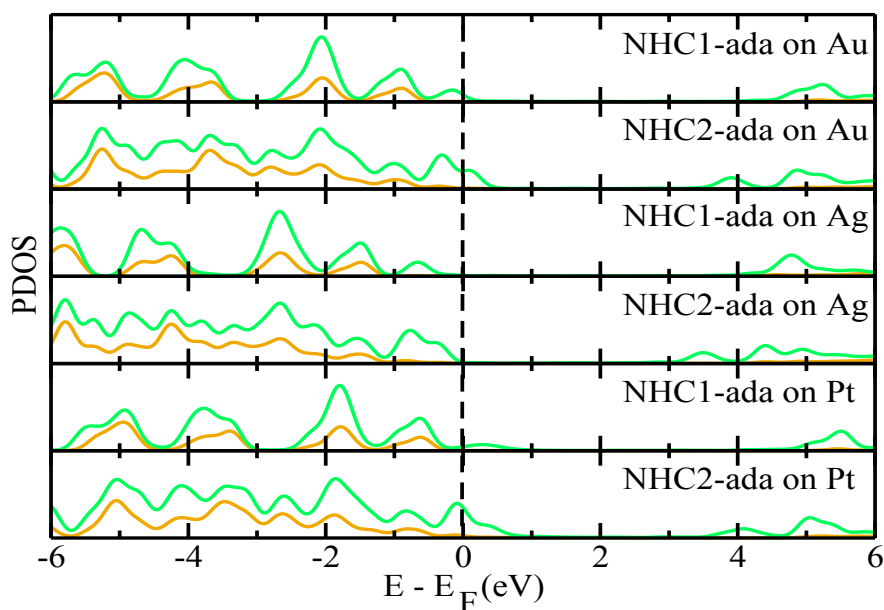


Figure 4.6: Projected density of states (PDOS) for both carbene-functionalized adamantane molecules after adsorption. The contributions from the s- and p-orbitals are depicted in black and red, respectively. The Fermi energy in each case was shifted to 0 eV.

the attraction of the nearest hydrogen atoms on Pt(111) as will be revealed through the analysis of the surface morphologies in the next sections. The calculated dipole moments of the NHC-ada/metal structures were extracted from our calculations. The x- and y-coordinates of the dipole moments of all six structures was zero. Only the z-component of the dipole moments was found nonzero, and are for the NHC1-ada/metal on Au(111), Ag(111), and Pt(111), -6.532, -5.519, -6.340 Debye, respectively. For NHC2/ada on the same metals, the dipole moment values are -7.224, -5.735, -6.912 Debye, respectively. Note, that the z-axis was taken normal to the modified surfaces. All dipole moments are negative indicating that in all cases, the dipole moment vector points from the adsorbed molecule towards the metal surface. Overall, the modified gold substrates show higher dipole moments. The NHC2-mediated adamantane SAM also corresponds to a larger dipole moment compared to the NHC1-ada adsorbed structures.

4.2.4 Work function

As a measure of the efficiency of carbene-mediated adamantane SAMs on metal surfaces for practical applications, we performed the analysis of their work functions Φ . We expect these to be modulated with respect to the work function of the clean metal surfaces, in a way that charge transfer from the modified surfaces becomes more efficient. This feature would be valuable for potential electronics applications of the NHC-ada/metals. An adsorbate layer contributes to the charge transfer in the adsorption procedure, significantly

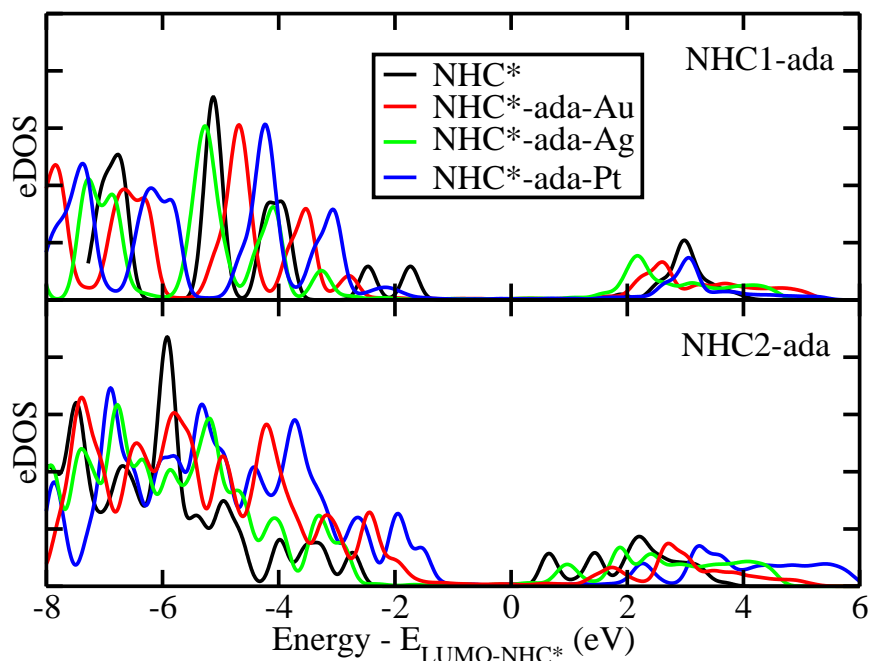


Figure 4.7: Total density of states (TDOS) of the NHC1 molecules (upper panel) and NHC2 molecules (lower panel) before and after adsorption over the metal surfaces. The energy has been shifted to LUMO level of the respective NHCs in all the cases. The color black denotes NHCs without adamantane attached to its apical region while red, green and blue represents the NHCs after adsorption over Au, Ag, and Pt respectively. The symbol * denotes either NHC1 or NHC2 molecule.

modulating the work function of the metal surface. The electrons leaving the metal surface will have to pass through the interface dipole layer. The orientation of the dipole influences the efficiency in the removal of electrons. The electrostatic potential at each point of the unit cell in our simulations is used to create an electrostatic profile along the z -direction normal to the surface. The work function is obtained from the electrostatic profile value in the vacuum area. The relationship of the work function and the surface dipole moment is given by:

$$\Delta\Phi = -\frac{e}{\epsilon_0} (\mu_z - \mu_{z,0}) = -\frac{e}{\epsilon_0} \Delta\mu \quad (4.2)$$

where μ_0 is the surface dipole per unit area, μ_z is the surface-normal dipole per unit area for the SAM adsorbed surface, e is the charge, and ϵ_0 is the dielectric constant. A positive value of μ indicates a dipole that is pointing away from the bulk, which leads to a decrease of the work function. A negative value of μ corresponds to a dipole pointing to the bulk, thus increasing the work function and hindering the charge transfer. The calculated work functions of

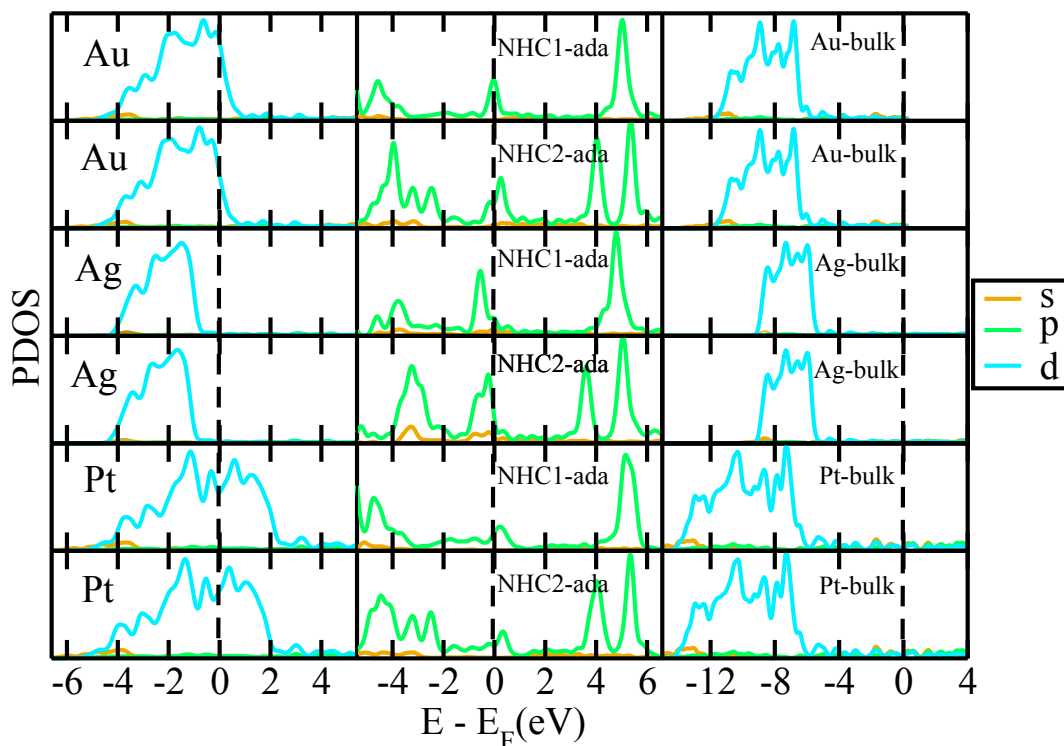


Figure 4.8: The contributions of the s-, p-, and d-orbitals to the PDOS of the metal surfaces are depicted for the first layer of the metal surface for Au(111), Ag(111), and Pt(111) on the left. For the same surfaces, the middle graphs depict the PDOS contribution of the s- and p-orbitals of the carbene carbon atom which is closest and binds to the metal surface. The right panels depict the PDOS for the bulk metals before adsorption. The Fermi energy has been shifted to 0 eV in all cases. The contributions of the s-, p-, and d-orbitals are shown in black, red, and blue, respectively.

the clean Au(111), Ag(111), and Pt(111) surfaces according to our calculations are 5.25, 4.5, and 5.73 eV, respectively. We have found that the adsorption of the NHC-ada SAMs lowers the work function considerably. To assess the two contributions from the molecule and the metal surface, we must consider two additional systems. We first remove the molecular layer and compute the electrostatic profile of the relaxed free gold surface. At a second step, we remove the gold surface and compute the electrostatic profile of the free radical SAM. We then superpose the electrostatic profile of these two systems after aligning the vacuum level on the right part as shown in Fig. 4.9. In this figure, the modulation of the work function due to the adsorption of the carbene-mediated adamantane monolayers is reported. The work function of the metal surface modified with the NHC1-functionalized adamantane was found to be 3.80 eV for Au(111), 3.26 eV for Ag(111), and 4.18 eV for Pt(111), respectively. For the NHC2-ada molecule, the work function was 3.82 eV for Au(111), 3.30 eV for Ag(111), and 4.30 eV for Pt(111), respectively. For both SAMs, we find a significant decrease in the work function of the order 37-38 % for Au(111), 36-38% for Ag(111), and 33-37 % for Pt(111). Overall, the work functions

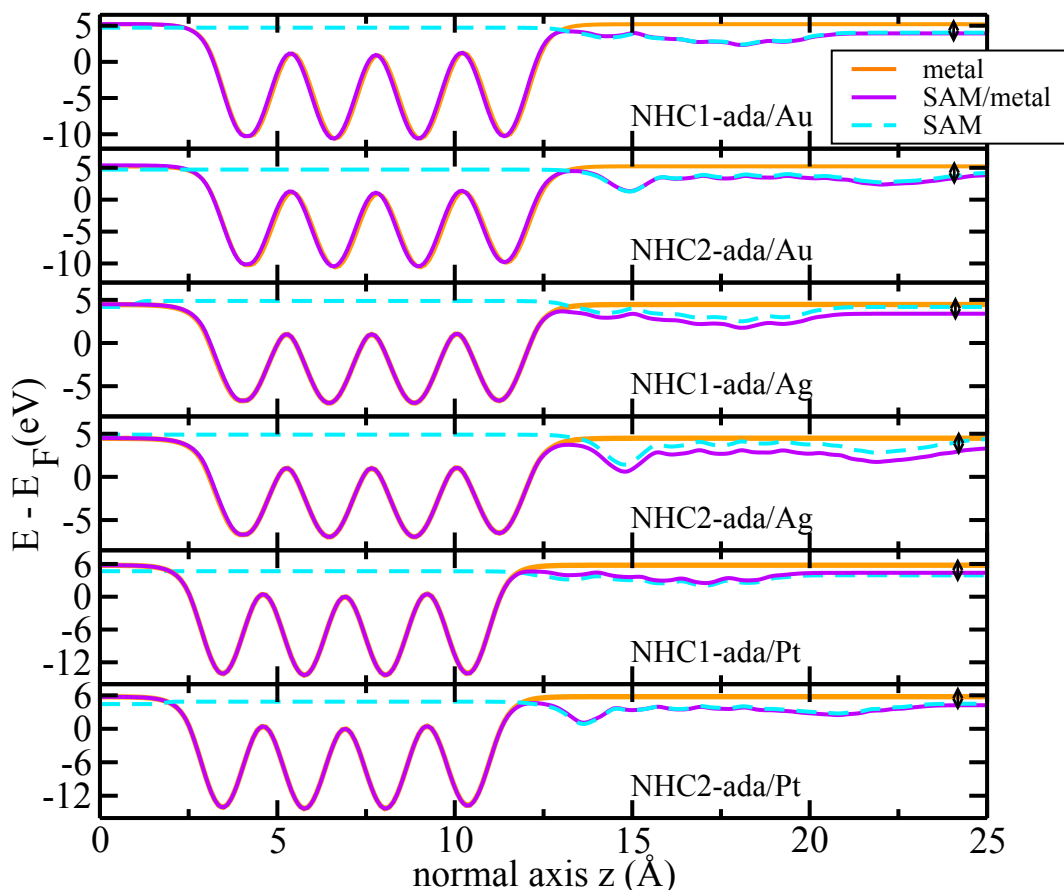


Figure 4.9: Plane averaged electrostatic profiles of the two different configurations of carbene-functionalized adamantane SAMs on all three surfaces. The labels denote the specifically modified surface for each panel. The zero energy is set at the Fermi level of each system. In orange, pink, and cyan are shown the electrostatic potentials of the bare metal substrate, the free molecule SAM, and the whole system, respectively. The black arrows between the cyan and the orange lines point to the work function shifts after adsorption.

for both SAMs and all three surfaces are very similar and differ only about 1-3%. For the NHC2-ada/metals the work functions are slightly higher and can presumably be assigned to the presence of the additional two C_3H_7 ligands in NHC2.

4.2.5 Surface morphology

In order to reveal the electronic and structural morphology of the metal surfaces, we looked into two additional features, the localization of the highest occupied orbitals close to the surface and the simulated scanning tunneling microscope (STM) images. In Fig. 4.11, the charge density distributions for the HOMO after adsorption reveal the re-arrangement of the total electronic charge due to the adsorption of the NHC-ada SAMs on the metal substrates. From this figure, it is clearly evident that the occupied orbitals after adsorp-

Table 4.2: Bader charge analysis comparing the charges on the SAM and the metal surfaces before and after adsorption. The first line denotes the modified system. All values are given in electrons.

SAMs	NHC1-ada			NHC2-ada		
	Au	Ag	Pt	Au	Ag	Pt
NHC-ada	+0.47	+0.31	+0.52	+0.48	+0.26	+0.51
metal	-0.28	-0.10	-0.34	-0.25	-0.03	-0.31

tion are mostly localized next to the bonding sites of the carbene lower tip and the surface of the metal. Qualitatively, no significant differences in the orbitals for the Au and Ag modified surfaces were found. Nevertheless, the orbitals tend to occupy the upper part of the carbene ring close to the adamantane in the case of the modified Pt(111). We also observe that the charge in the case of Pt(111) is spread over the whole carbene ring, which is not the case in the modified Au(111) and Ag(111) surfaces. In the latter two cases, the charge re-arrangement occurs mainly around the carbene atoms which are closer to the metal surface and are involved in the bonding.

A Bader charge analysis was performed in order to reveal the effect of SAM adsorption on the modified surfaces [102]. Specifically, we calculate the change in the total charge in the molecule and the surface after the adsorption of the molecule on the metal surfaces, compared to its total charge before adsorption. All results are summarized in Table 4.2. The changes in the total charge due to adsorption are given separately for the adsorbed molecule only ('NHC-ada' in the Table) and the substrate only ('metal' in the Table). Overall, the surfaces have a negative change in their charge after adsorption, while the NHC-ada molecules a positive change. This finding indicates that the charge re-arrangement in the NHC-ada/metal structures is being done in a way to move charge towards the molecule, an important property towards applications like field-emission displays.

STM images

The application of a bias voltage between the tip and the NHC-ada/metal when these are brought close to each other at a distance of a few angstroms will enable the electrons to tunnel through the vacuum space between the two surfaces. The electron flow is usually referred as tunneling current and is dependent on three parameters: the distance of vacuum between the surfaces, the applied bias voltage, and the local density of states. We keep the distance of an STM tip at about 10 Å above the NHC-ada/metal surface along the normal z-axis while scanning with the tip the XY-plane of this surface to produce a constant current. We consider a negative surface bias of -1 V in order to sample all occupied surface states from this energy value up to the Fermi level. This enables the measurement of the topography of the NHC-ada SAM surfaces and reveals the STM images of all modified metal surfaces studied here. In Fig. 4.10, we show the simulated STM images of all SAM-modified

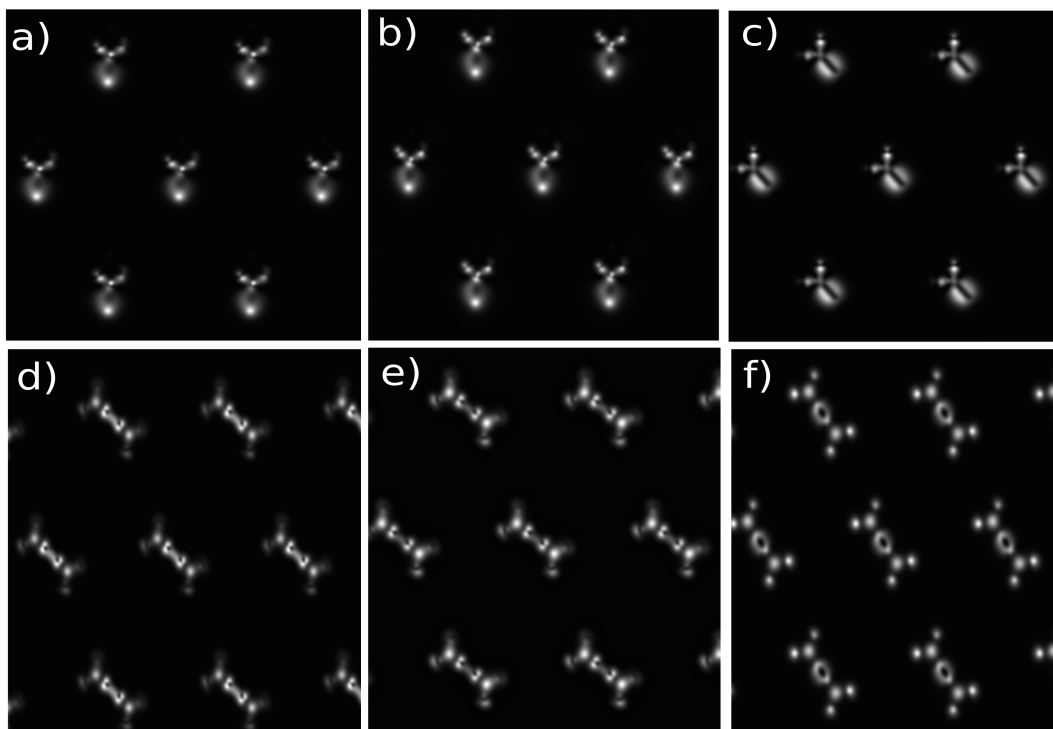


Figure 4.10: In (a)-(c) the simulated STM images of the systems after adsorption of NHC1 on Au(111), Ag(111), and Pt(111), respectively are shown. Panels (d)-(f) correspond to the simulated STM images of the NHC2 on Au(111), Ag(111), and Pt(111), respectively. For the STM simulations, a negative bias of -1 V was applied to the surface at a height of 10 Å above the surface.

metal surfaces. These images are produced by calculating the contour plots of the tunneling current density on the plane parallel to the surface. From this analysis, distinct bright spots corresponding to the carbene-functionalized adamantane adsorbed to the surface are seen. A brighter spot is observed in all STM panels on the atoms which are more involved in the bonding to the surface. A similar behaviour to the charge re-distributions is evident in Fig. 4.11 in terms of the molecular orientation of the carbene-functionalized adamantane on the metal substrate.

The more extensive structure of the NHC2-ada is clear in the lower panels of Fig 4.10. This feature is based on the additional C_3H_7 ligand in NHC2. A slightly different orientation of both NHC1-ada and NHC2-ada on Pt(111) compared to their orientation on the gold and silver surfaces is evident. Note, that before structural relaxation all NHC-ada SAMs were placed with the same orientation on all metal surfaces. Small differences in the bright spots in the case of Pt(111) also denote different binding characteristics compared to the Au(111) and Ag(111) cases. This is in agreement with the observation we made based on Fig. 4.11(c) and (f), that the charge on Pt(111) involves the whole carbene ring and not only the lower N-C-N atoms closer to the surface as in the modified gold and silver surfaces. The different charge re-distribution

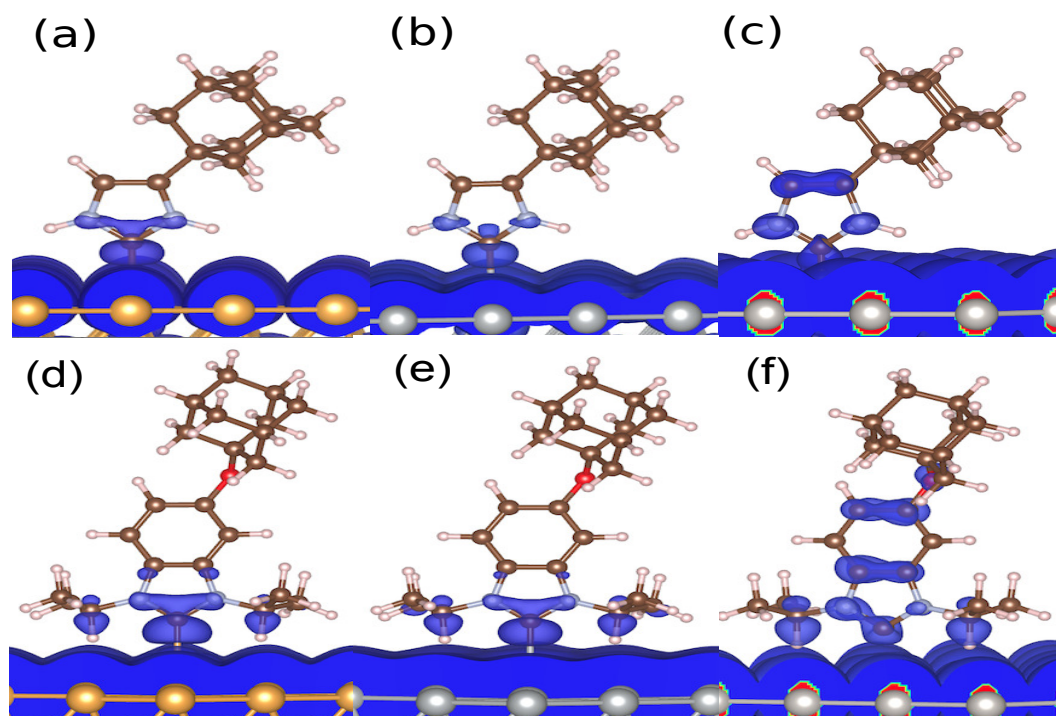


Figure 4.11: In upper panel (a)-(c) the re-distribution of the charge density of the HOMO after adsorption of NHC1 on the metal surfaces Au(111), Ag(111), and Pt(111), respectively are shown. Lower panels (d)-(f) depict the charge re-distribution of the HOMO after adsorption of NHC2 on Au(111), Ag(111), and Pt(111), respectively.

of the molecule on Pt(111) is also clear by comparing panel (f) to panels (d) and (e) of Fig. 4.11. The shorter distance of the H atoms of the NHC2 ligand to Pt(111) surface given in Table 4.1, link to a bonding of these H atoms to the Pt surface. The adsorbate (NHC2-ada) orientation on Pt(111) changes in order to facilitate this bonding. This is not the case in NHC1-ada/Pt for which we also observe a different orientation with respect to NHC1-ada/Au and NHC1-ada/Ag. The difference here is based on the observation in Fig. 4.11(c) that the charge re-distribution in NHC1-ada/Pt involves the whole carbene ring. Accordingly, the charge of the whole ring promotes (or is involved) in the bonding and again the NHC1-ada needs to re-orient to account for this additional attraction.

4.3 Discussion

In summary, we have successfully modelled the adsorption behaviour of carbene-functionalized diamondoids on different metal surfaces. Au(111) and Pt(111) were found to be the most efficient metal surfaces for adsorbing carbene-mediated diamondoid SAMs than the Ag(111) surfaces. The weaker bonding of Ag(111) was justified by the non-availability of the d-orbital of the metallic first layer of the surface around the Fermi level. By comparing the molecular

adsorption energies on reconstructed Au(111), Ag(111), and Pt(111) surfaces, we conclude that these geometries are stable and of practical interest. Nevertheless, carbene molecules have proven to be a better alternative to the thiol-based bonding of diamondoids on metallic surfaces, opening up the path for more stable and efficient SAMs/metal devices. Dynamic tuning of the work function was easily achieved in NHC-ada/metal devices for organic electronic applications. Finally, in this chapter we have demonstrated the possibility to use small diamondoids to coat metal surfaces and assessed the search for optimal anchoring of molecules on surfaces. Based on these findings and in view of its electronic applications, we present a theoretical study of the diamondoid-based molecular device in the next chapter.

Chapter 5

Diamondoid-based molecular junction

In this chapter, we deal with the computational investigation of diamondoid-based molecular conductance junctions and their electronic transport properties. A small diamondoid is placed between the two gold electrodes of the junction and is covalently bonded to the gold electrodes through two different molecules, a thiol group, and an N-heterocyclic carbene molecule. In section 5.2.2, the transport properties of these devices and the influence on these of different functionalizations, dopants, and diamondoid sizes are discussed. Next, we perform a comparative study of various devices based on their electronic transport properties. We also present their structural and electronic characteristics. In the end, we discuss the implications of our results on novel nanotechnological applications of diamondoid-based molecular devices. Some of the sections of this chapter are also the part of our published article "Bibek Adhikari et al 2016 Nanotechnology 27 485207 © IOP Publishing. Reproduced with permission. All rights reserved".

5.1 Molecular junction

A molecular junction is simply defined as a system where a molecule or a collection of molecules is embedded in between two probes or electrodes [103] as sketched in Fig. 5.1. The major component of a particular junction is the molecule that is embedded in between. The stability, conductance, transmission, and efficiency of the junction depends on the properties of molecules. These molecules affect the bulk properties of the whole system. The fact that diamondoids are used as building blocks and can be efficiently attached on metal surfaces can naturally suggest their use in molecular conductance junctions [2, 104–106]. The field of molecular electronics was introduced four decades ago with the proposal of using a single organic molecule as a rectifier [107]. Since then, the idea that a molecule sandwiched between a metal junction could be used as a sub-nanometer electronic component has been vigorously pursued with the hope of replacing the existing silicon technology in electronics applications as they approach device scaling limits [108–113].

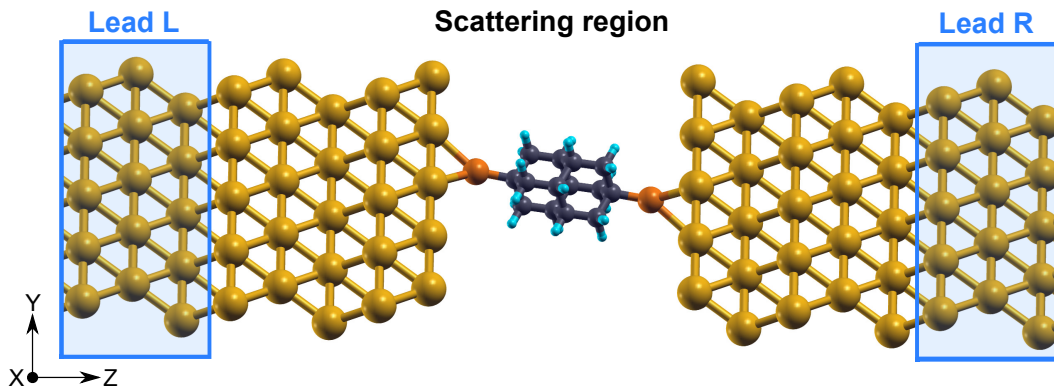


Figure 5.1: The setup for the transport calculations: the dithiol-diamantane and the inner ten layers of the Au(111) (five on each side of the molecule along the z-direction) determine the scattering region. This is in turn coupled to semi-infinite leads (made of 3 layers of gold) on both sides. Electronic transport occurs along the z-direction.

Doping and functionalization using boron and nitrogen have always been used in the past to tune the electronic properties of such devices [114–118]. The alteration and modification of transmission spectra are mainly due to the shift in the energy levels of the electrode which resulted in the rectifying behavior with respect to the applied source and drain voltage. [119–125] In our investigation, we study the influence of two different diamondoids (diamantane and tetramantane), the type of dopants, and the diamondoid functionalization on the properties of a metallic break-junction [126]. In such a device, a diamondoid is inserted and bonded through the functionalization groups on the metallic surfaces. For the electrodes, two Au(111) surfaces are taken. In order to evaluate the effects mentioned above, we pick two representative lower diamondoid cases, diamantane, and tetramantane to vary the diamondoid size. For tetramantane, one of the isomers, the [121]-tetramantane molecule was chosen [1]. Boron (B), nitrogen (N) and boron with nitrogen (BN) are chosen to separately dope the diamondoids. Accordingly, in the doping cases, one of the carbon atoms of the diamondoid cages are replaced by one of the dopants. For the functionalization molecules, we have used (a) a thiol group (commonly used to attach diamondoids on a metal surface) and (b) the N-hetero-cyclic carbene (NHC) molecule, a member of the carbene family [127].

Overall, we have considered a set of sixteen different diamondoid-based devices, which differ in the diamondoid size (2 variations), the doping (4 variations - 3 doped and one undoped case), and the functionalization molecules (2 variations). These functionalized diamondoids chosen to be placed within the gold junction are shown in Figs. 5.2,5.3. In the following, we use the notation 'diam' and 'tetra' for diamantane and (121)-tetramantane, respectively. 'X-doped', with X=B, N, and BN, denotes the doping of the diamondoid, while the term 'undoped' is used for the undoped diamondoids. Note, that the diamondoids are functionalized on both sides in order to bind to the Au(111) surfaces on

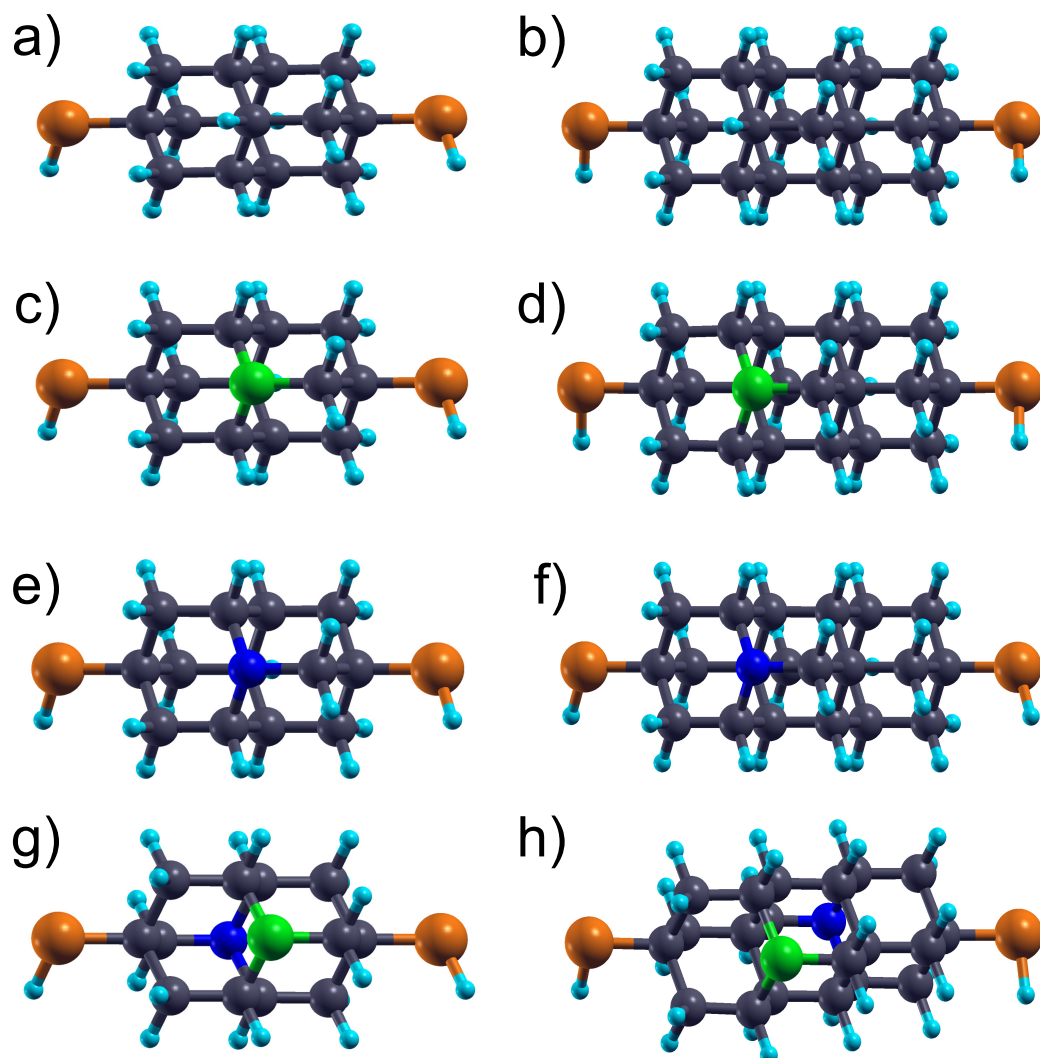


Figure 5.2: The relaxed atomic structures of the dithiol-molecules which will be inserted in the gold nano gap. (a) dithiol diamantane, (b) dithiol tetramantane, (c) dithiol B-doped diamantane (d) dithiol B-doped tetramantane (e) dithiol N-doped diamantane (f) dithiol N-doped tetramantane (g) dithiol BN-doped diamantane (h) dithiol BN-doped tetramantane. The color coding for the atoms is set as follows: carbon(grey), hydrogen(cyan), nitrogen(blue), boron(green), and sulphur(orange). This color coding will be used in the following.

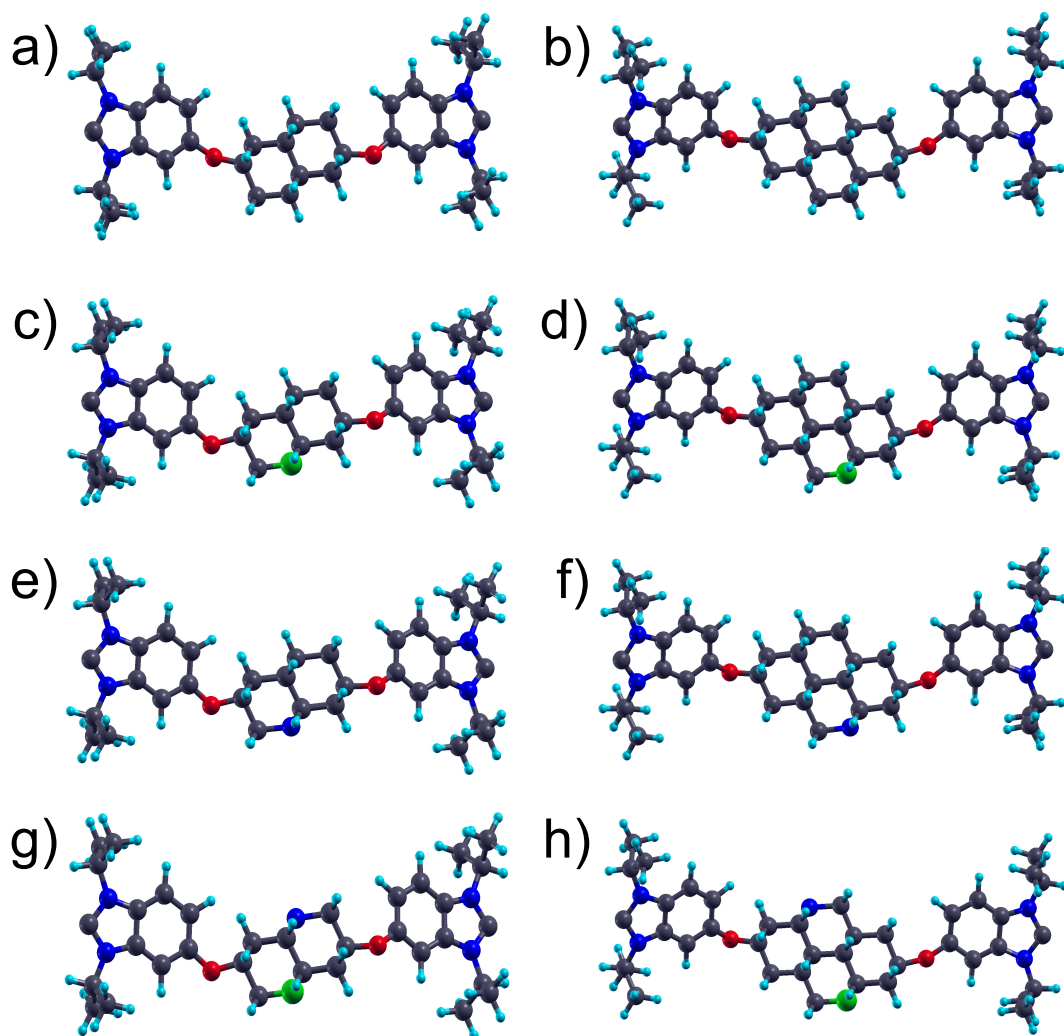


Figure 5.3: The relaxed atomic structures of the dicarbene-molecules which will be inserted in the gold nano gap. (a) diNHC diamantane, (b) diNHC tetramantane, (c) diNHC B-doped diamantane, (d) diNHC B-doped tetramantane (e) diNHC N-doped diamantane (f) diNHC N-doped tetramantane (g) diNHC BN-doped diamantane (h) diNHC BN-doped tetramantane. The color coding for the atoms is set as follows: carbon(grey), hydrogen(cyan), nitrogen(blue), boron(green), and oxygen(red).

each side of the nano gap. Accordingly, the notations 'dithiol', and 'diNHC' denote the double functionalization using a thiol or a carbene (NHC) group. The molecules are placed within the Au(111) junction and then relaxed. Five 5×5 Au(111) layers are used as the screening layer at each side of the surface between the electrode and the molecule as depicted in Fig. 5.1. These Au(111) surfaces together with the inserted molecule consist the scattering region (device). The device is coupled on either side to three outer layers of Au(111) which form the semi-infinite leads. For the device relaxation, two inner atomic layers of the Au(111) surface on either side of the molecules was also allowed to relax to enable preferential binding. The other three outer layer of the device Au(111) were fixed at their bulk positions. Finally, for the fully relaxed devices, electronic transport calculations were performed by means of coupling to semi-infinite leads on either side, the results of which are discussed in the next section. There is no direct tunneling across the Au(111) nano gaps for a capacitor distance of 6 Å or more [128].

5.2 Diamondoid within a gold nano gap

Simulations based on the density functional theory (DFT) [129, 130] as implemented in the code SIESTA [59] were carried out. We have used the generalized gradient approximation of Perdew-Burke-Erzerhof (PBE-GGA) [45], and the norm-conserving Troullier-Martins pseudopotentials [52]. For the basis set, we have considered a double- ζ with polarization basis set (DZP) for the molecules, and a single- ζ with polarization (SZP) for the gold atoms ($5d^{10}$, $6s^1$) which has been proven efficient for similar setup [128]. An energy shift of 0.01 Ry with a real space sampling grid (mesh cutoff) of 200 Ry. A Monkhorst-Pack k-points mesh of $5 \times 5 \times 1$ for the scattering region and $5 \times 5 \times 40$ for the semi-infinite leads were used. The Au(111) unit cell was fully relaxed and we obtained the lattice constant of 4.186 Å which compares well with the data reported in literature [58]. The geometry optimization of the length of the scattering region was performed using the conjugate gradient algorithm and the structure was relaxed until the net forces on each component were lower than 0.01 eV/Å. The electronic transport calculations are performed using DFT combined with the non-equilibrium Green's functions (NEGF) formalism, as implemented in the TranSIESTA [64] code. Bias dependent self-consistent calculations were performed to obtain the current-voltage characteristics ranging from -0.9 V to $+0.9$ V in steps of 0.1 V. The current (I) through the scattering region at a bias (V_b) is calculated by integration of the transmission spectrum using the Landauer-Büttiker formula [62]:

$$I(V_b) = \frac{2e}{h} \int_{-\mu_R}^{\mu_L} T(E, V_b) [f_L(E - \mu_L) - f_R(E - \mu_R)] dE \quad (5.1)$$

where $T(E, V_b)$ is the bias dependent transmission probability of an electron with energy E , and $f_L(E - \mu_L)$, $f_R(E - \mu_R)$ are the Fermi-Dirac distribution for the left and right electrode, respectively. The electrochemical potential for

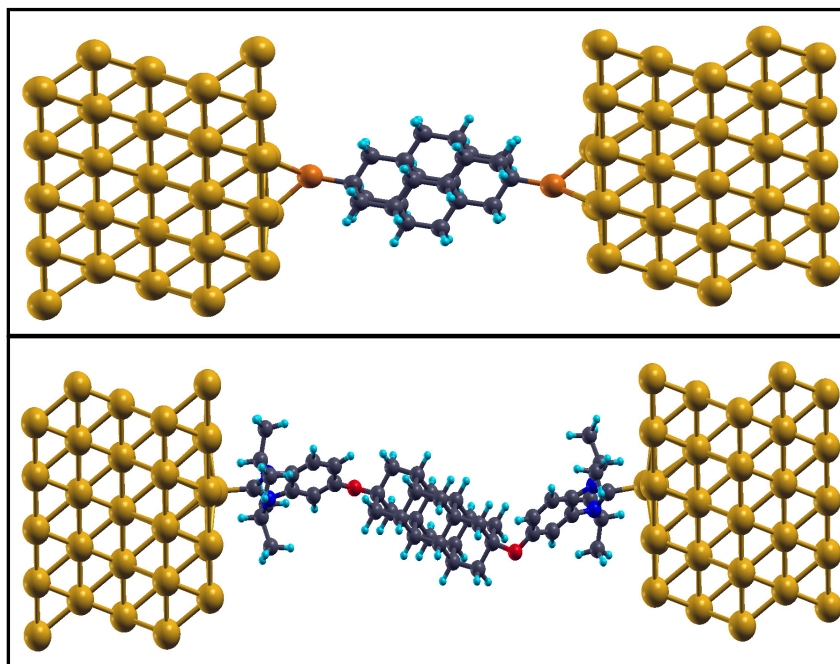


Figure 5.4: Final relaxed structure for: (top panel) a dithiol-tetramantane and (bottom panel) a diNHC-tetramantane in between Au(111) layers.

the left electrode is given as $\mu_L = E_F + V_b/2$ and $\mu_R = E_F - V_b/2$ for the right electrode. The Fermi energy E_F is shifted to zero.

5.2.1 Structural Characteristics

We begin our analysis with the structural details of the various diamondoids in the gold nano gap. Representative devices are depicted in Fig. 5.4 for dithiol- and dicarbene-diamondoid devices. In all devices studied here, the diamondoids are bonded to both electrodes through the mediating molecules (thiol group or carbene). In Fig. 5.4 bottom panel), the molecules are attached to the surface only through the lower carbon atom of the carbene ring. Two of the H atoms of the NHC molecule (on both electrodes) are very close (≈ 2.80 Å) to the gold surface and interact weakly with the surface. The bond length of the molecule to the surfaces is in the range of $(2.64 - 2.90)$ Å for the dithiol-diamantane and $(2.61 - 2.92)$ Å for the dithiol-tetramantane cases, respectively and corresponds to the S-Au distance. In the diNHC-diamantane and tetramantane cases, the C-Au distance for both electrodes is in the range of $(2.19 - 2.20)$ Å and $(2.19 - 2.21)$ Å, respectively. The dithiol-diamondoids are less flexible within the junction compared to the diNHC-diamondoids, hence the difference in the bonding behavior to the metal surface. This is also qualitatively observed through the orientation of the molecules with respect to the setups before structural relaxation.

In the dithiol cases, the preferred bonding site for S-Au is on the fcc center bonded with three gold atoms. In the NHC cases, the on-top site is preferred

for the C-Au bond. We have observed that the gold atom bonded to the NHC moves closer (and out of the surface) to the lower carbon atom of the carbene ring as reported in previous studies [97,127]. This is slightly visible in (Fig. 5.4 bottom panel). The flexibility of the C-O-C bond between NHC and diamondoid allows for additional conformational variability during relaxation. Here, though only a certain conformation will be examined for simplicity. Note, that a slight off-lattice movement of the Au atom bonded to the sulfur atom also in the dithiol cases was evident (see Fig. 5.4 top panel). Regarding the doped diamondoids, very small changes of about 2 – 4% in the bond lengths at the vicinity of the dopants were observed with respect to the undoped diamondoid cases. However, since B and N are typical dopants for carbon materials and have electronic configurations very close to C, no significant alterations in the structures have been observed. These small changes, though, have a higher impact in the electronic and transport properties as will be shown next. Note, that according to our simulations, the electronic band gaps for the isolated dithiol diamantane, dithiol tetramantane, diNHC diamantane, and diNHC tetramantane molecules are 5.29, 5.36, 3.19 and 3.24 eV, respectively.

5.2.2 Electronic properties

We next probe the electronic properties of the diamondoid gold-junction devices through the electronic density of states (eDOS) as obtained from our transport calculations. Although, DFT does not lead to accurate values for electronic band gaps, a qualitative comparison of the respective properties of the different nano gaps studied here is possible. All systems show a metallic behavior arising from the contribution of the gold electrodes and can accommodate the flow of electronic current across these devices. In Fig. 5.5, the partial density of states (PDOS) for representative functionalized tetramantane molecules within the gold junction is shown. The results are shown for the energy range $[-3.0, -2.0]$ eV, as actually all the interesting characteristics are found in this range. In the graphs, the contributions of the gold electrodes and the different elements in the molecules are depicted. Clear peaks in the PDOS are visible. Focus on the dithiol-tetramantane device in Fig. 5.5(a) shows very sharp peaks in the total DOS, which are related to peaks in the contributions from the diamondoid (C and H atoms). The baseline of the total DOS is associated with the contribution of the gold electrodes as in all cases. The thiol groups have also a small contribution in the total DOS in the cases of the dithiol-diamondoids. For dithiol-tetramantane doped with nitrogen, the role of the dopant is also underlined by characteristic peaks. Very close to the Fermi level (at -0.4578 eV), the N dopant defines the total eDOS (inset of Fig. 5.5(b)). In this energy range, the eDOS in the ideal case is rather flat manifesting the additional electronic states nitrogen is adding to the system. The next peak close to -2.2 eV coincides with electronic states coming from the diamondoid and its carbon atoms.

The eDOS characteristics for the carbene functionalization differ qualitatively.

All peaks in the PDOS are associated with the presence of the nitrogen and oxygen atoms in the carbene molecule as evident from Fig. 5.5(c) for the ideal diNHC-tetramantane device. Compared to the ideal dithiol-tetramantane electrodes, more peaks in the total eDOS are seen in the respective carbene case. The additional electronic states are related to the presence of the carbene molecules, while the contribution of the diamondoid, mainly through its carbon atoms is quite smaller. Specifically, the N and O atoms in the carbene molecules are responsible for the additional features in the eDOS. Characteristic electronic states arising from the nitrogen atoms are the ones closer to the Fermi level (set at 0 eV) than the other peaks. These coincide with states from the carbon atoms but are more pronounced. Again, the metallic behaviour in the eDOS arises from the gold electrodes. For the nitrogen doped diNHC-tetramantane electrodes in Fig. 5.5(d), the peaks are lower compared to the ideal case. The addition of the nitrogen dopant does not significantly change the eDOS features, as this atom is only an excess N to the already existing four N atoms of the carbene molecule. In this respect, the electronic states corresponding to N are already characteristic of the eDOS in the ideal case. Actually, the ideal and nitrogen doped diNHC-tetramantane cases have the first peaks in their eDOS at lower energies (-1.70 and -1.23 eV, respectively). These peaks are dominated by the contributions from the N and O atoms of the carbene molecule and the C atoms of the tetramantane. The doping with nitrogen shifts the first DOS peak about 0.5 eV towards the Fermi level. In this first peak for the N-doped diNHC-tetramantane, the O atoms do not play a significant role. Their role is rather manifested in the second peak. This second peak is shifted about -0.12 eV lower than in the undoped diNHC-tetramantane case.

5.2.3 Electronic transport

Next, the electronic transport across the diamondoid junctions are analyzed. The quantum transport calculations lead to the calculated zero-bias transmission functions, $T(E, V = 0)$ summarized in Fig. 5.6 for all cases studied here. The electronic transport across the molecule is strongly influenced by the choice of the functionalizing group through which the molecule is attached to metal. We begin by investigating the effect of different functionalization groups: the dithiol (Fig. 5.6 top panel) and diNHC cases (Fig. 5.6 bottom panel) for undoped diamondoids on the transmission function. The first observation is that the transmission at the Fermi level for all dithiol diamondoids is at least six orders of magnitude higher in comparison to their diNHC counterpart. The zero bias conductance ($G = \frac{2e^2}{h}T(E_F)$) for undoped di-thiol diamondoids is summarized in Table 5.1 and are comparable to the values reported for π -conjugated organic compounds [131]. Consequently, with an applied bias voltage, a dithiolated diamondoid is expected to lead to a higher current flow in comparison to the diNHC counterpart. In all the undoped cases, the first transmission peak (HOMO) is found to be further away from the Fermi level. The HOMO levels are at -2.53 eV, -2.10 eV, -3.21 eV and -2.87 eV

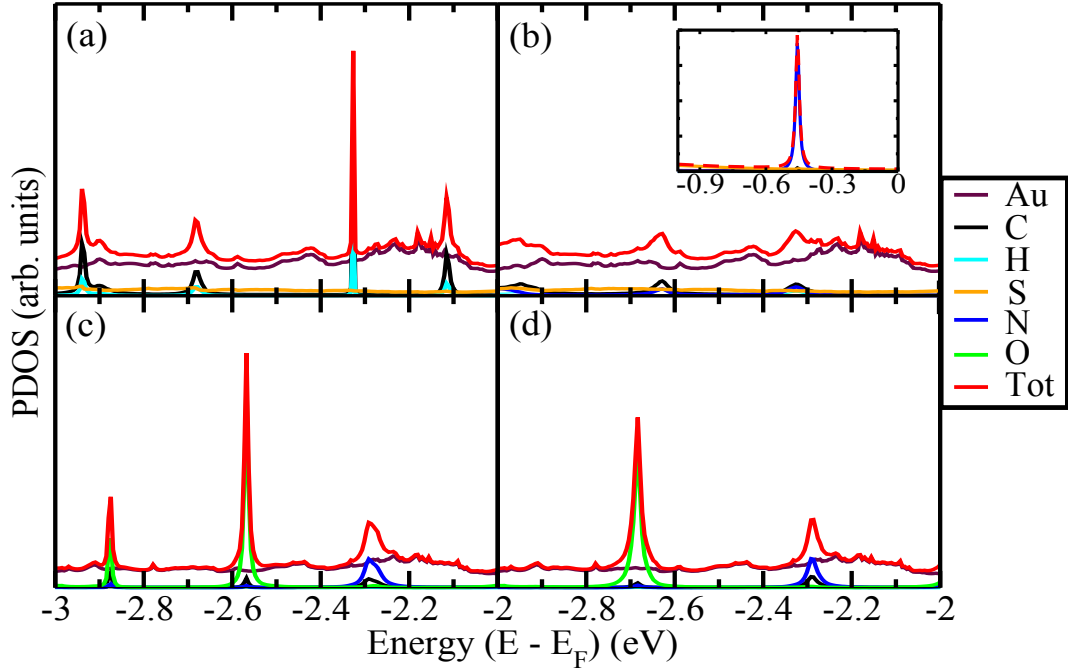


Figure 5.5: Partial density of states (PDOS) are given for the following molecular junctions: (a-b) dithiol- tetramantane and (c-d) dithiol N-doped tetramantane. The contributions of the molecule, the electrodes, and the dopants are shown together with the total DOS. The Fermi level is set at 0 eV.

for dithiol-diamantane, dithiol-tetramantane, diNHC-diamantane and diNHC-tetramantane, respectively. The effect of dopants on the zero-bias transmission function can also be seen in Fig. 5.6. The diNHC-based doped diamondoid junctions have resonance peaks (Fig. 5.6 bottom panel) far below the Fermi level (beyond the range of a practical bias voltage window) similar to the undoped case. This is not the case with the dithiol-based doped junctions. In all dithiol cases, the transmission is higher for the N-doped diamondoids, which is not the case in the diNHC cases. In order to understand this further, we turn to the nitrogen doping on dithiol-based tetramantane junctions (Fig. 5.6 top right panel). The first transmission peak below the Fermi level (HOMO) in this case is found at around -0.45 eV. The calculations revealed that the resonance peak (at -0.4578 eV) in the projected density of states (PDOS) corresponds to a density of states contribution from nitrogen doping. The lowest unoccupied molecular orbital (LUMO) is far from the Fermi level in all the cases. We only observe prominent peaks of the LUMO beyond 2.5 eV for the dithiol cases and beyond 2.0 eV for the diNHC cases respectively. In this respect, the LUMO level is not of high importance to the conduction within a bias window practically accessible in experiments. BN and B doping does not lead to any improvement in the zero bias conductance of dithiol junctions as also easily observed in Table 5.1. Interestingly, the B-doped diNHC-tetra junctions show the highest zero bias conductance compared to all the diNHC-tetra cases. However, all zero bias conductance values for all diNHC-diamondoid electrodes are at least five orders of magnitude lower than the respective dithiol-diamondoid

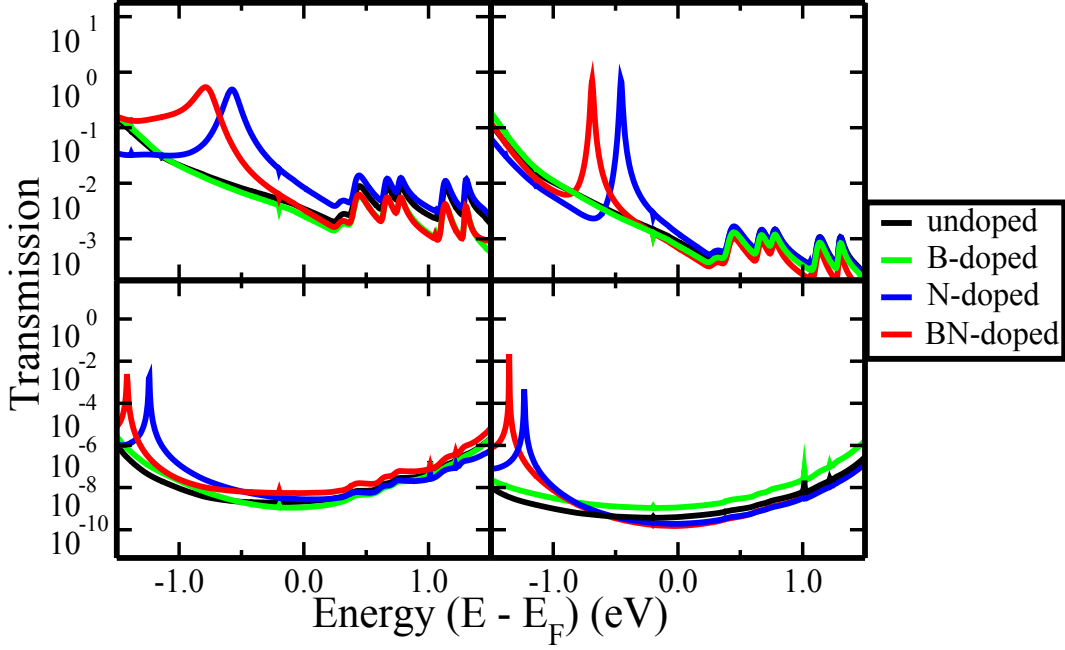


Figure 5.6: The zero-bias transmission function is plotted on a semi-log scale for all diamondoid-based devices studied in this work. In the top panel, data for the dithiol diamantane (left) and dithiol tetramantane (right) based devices are depicted. In the bottom panel, data for the diNHC diamantane (left) and diNHC (right) tetramantane devices are shown. The colors in the legends denote whether the diamondoids are doped or undoped.

cases. The respective values for the zero bias conductance at the Fermi level for all nano gaps studied here are summarized in the bar charts of Fig. 5.7.

The results are shown as a relative conductance using two different references: (a) the case of the undoped diamondoid for each type of the device and (b) the N-doped dithiol tetramantane nano gap, which is the 'best' transmission case showing the highest transmission closer to the Fermi level. Negative values correspond to a lower transmission with respect to the reference device. In case (a), the significance of doping with nitrogen is high for both the dithiol- and diNHC-diamondoid electrodes considered here (left panel of Fig. 5.7). Doping with boron shows a much larger conductance at the Fermi level only

Table 5.1: Conductance in units of $2e^2/h$ at zero bias for the modified diamondoid junction at the Fermi level. The higher transmission for each junction is given in boldface text.

type	dithiol-diam	dithiol-tetra	diNHC-diam	diNHC-tetra
undoped	6.94×10^{-3}	1.77×10^{-3}	4.34×10^{-9}	8.00×10^{-10}
B-doped	5.11×10^{-3}	1.50×10^{-3}	2.29×10^{-9}	2.29×10^{-9}
N-doped	1.67×10^{-2}	2.49×10^{-3}	5.55×10^{-9}	3.81×10^{-10}
BN-doped	6.65×10^{-3}	1.36×10^{-3}	1.10×10^{-8}	3.02×10^{-10}

for diNHC-tetramantane, while doping with BN shows a much higher transmission for the diNHC-diamantane device. In case (b), the behavior of all devices is similar (right panel of Fig. 5.7). The decrease in the conductance shows a very clear trend, moving from the undoped diamondoids to B-, N- and BN-doping with respect to the dithiol N-doped diamantane. All diamondoid-based electrodes at the Fermi level have a much lower conductance, with a decrease up to 400% for the BN-doped diNHC-tetramantane case. The lowest decrease in the conductance was found for all the ideal undoped diamondoids, followed by the B-doped cases. The size of the diamondoid also seems to affect

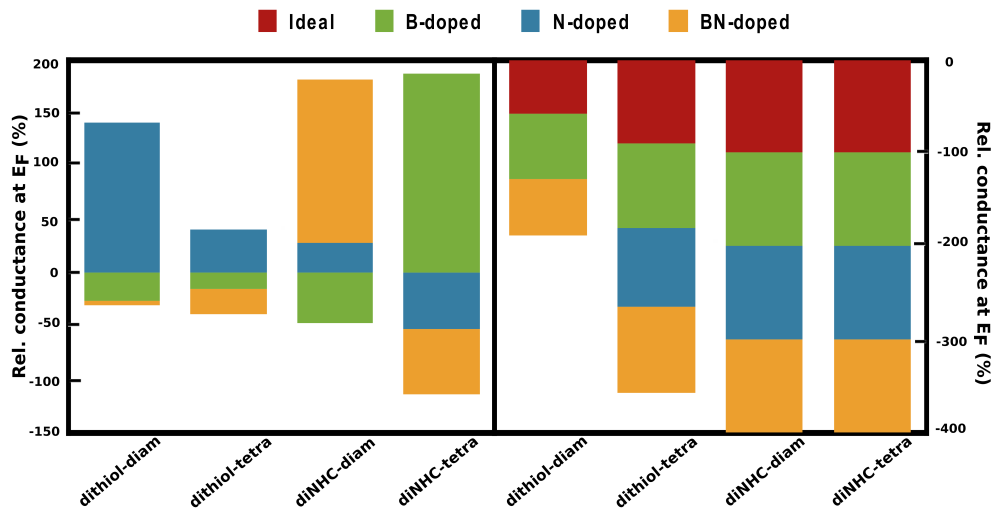


Figure 5.7: Bar charts of the conductance at zero bias for the modified-diamondoid nano gaps at the Fermi level compared to reference cases. In (a) the undoped diamondoid device for each functionalized-diamondoid is taken as the reference. The energy of all the ideal cases has been shifted to zero. In (b) the N-doped dithiol diamantane case with a transmission value of 1.67×10^{-2} was taken as the reference. The energy for the dithiol N-doped tetramantane electrodes has been shifted to zero.

the transmission. This is evident in the dithiol cases, in which the larger diamondoid (tetramantane) shows sharper transmission peaks (below the Fermi level) for the N- and BN-doped cases compared to the smaller diamantane, as seen in the top panel of Fig. 5.6. Nevertheless, in the diNHC cases, the transmission peaks are similarly sharp for both diamondoid sizes (lower panel of the same figure). In the latter cases, the transmission peaks of the N- and BN-doped diamantane are much broader, though almost at the same energies as in the respective tetramantane cases. The different features for the diamondoid sizes indicate that the increment in the size of diamondoids has an effect on the localization of the HOMO resonance peak close to the Fermi level. Overall, though the thiol-diamondoid devices show a larger transmission closer to the Fermi level, there are energy ranges in which the diNHC devices can better accommodate the flow of current. This happens, for example, lower than -1.5 eV in the diNHC B-doped tetramantane devices, as compared to the

respective dithiol case. The zero bias conductance values presented in Table 5.1 imply that the conductance across the two dithiol-diamondoid junctions is of the same order of magnitude, but slightly larger for the smaller diamantane. Both the N-doped dithiol diamantane and N-doped dithiol tetramantane cases show the zero bias conductance of $1.67 \times 10^{-2} G_0$ and $2.49 \times 10^{-3} G_0$, which is comparatively higher with respect to the previously investigated systems [109]. The respective value for the N-doped tetramantane case, though, is still higher than the values of the other tetramantane cases. This suggests that diamondoids could be used as a molecular conductance junction in the design of highly functional devices. In order to further understand the undoped vs doping among the dithiol-tetramantane junctions, we have plotted the eigenchannel wavefunctions (EWF) [132]. For the undoped, N-doped and BN-doped dithiol-tetramantane cases, these are plotted in Fig. 5.8, each at two different energies. The EWF plotted correspond to the Fermi level at 0 eV and the first transmission peak below the Fermi level i.e. at -2.10 , -0.45 and -0.68 eV for the undoped, N-, and BN-doped cases respectively. At the Fermi level, due to finite transmission (of the order of 10^{-3} according to Fig. 5.6), the EWF are localized towards the left of the device and then decay off in the transport direction. The peaks in the transmission across the doped dithiol-tetramantane junctions in Fig. 5.6 (top panel) correspond to a strong electronic coupling between the two electrodes as depicted in Fig. 5.8. For both the doped dithiol-tetramantane junctions, the EWFs spread out across the whole device region. In the undoped case, the molecular orbital corresponding to strong electronic coupling is far below the Fermi level. Hence, doping shifts transmission peaks closer to the Fermi level, which might contribute to conductance in a practically accessible bias voltage region. A further comparison of the dithiol N-doped tetramantane to the B-doped tetramantane and the respective doped diNHC-tetramantane cases is given in Fig. 5.9.

The energy (-0.4578 eV) corresponding to the first transmission peak for the dithiol N-doped tetramantane junction Fig. 5.6(b) is taken. At this energy, the transmission curves of the other cases in Fig. 5.9 are very low. Hence, a strong coupling of the electrodes in the dithiol N-doped tetramantane is evident as the EWFs are spread out across the electrode surfaces and the functionalized tetramantane. At this energy, the EWFs of the diNHC doped cases are associated with the left electrode with a small contribution coming from the left carbene molecule. No electronic current is flowing through these devices at the specific energy. In the dithiol B-doped tetramantane electrodes, the EWFs are more extended over the thiol group and half of the diamondoid, but no coupling of the two electrodes is observed, thus no current flow can occur. Finally, we observe a qualitative difference in the electronic coupling of the dithiol and diNHC cases. For example, in the dithiol B-doped tetramantane case, the wavefunctions are more spread-out, covering half of the diamondoid. This is not the case in diNHC B-doped tetramantane, in which the EWFs are spread-out only up to the first carbene molecule and its oxygen atom. The same is observed in the respective diNHC N-doped case. These features,

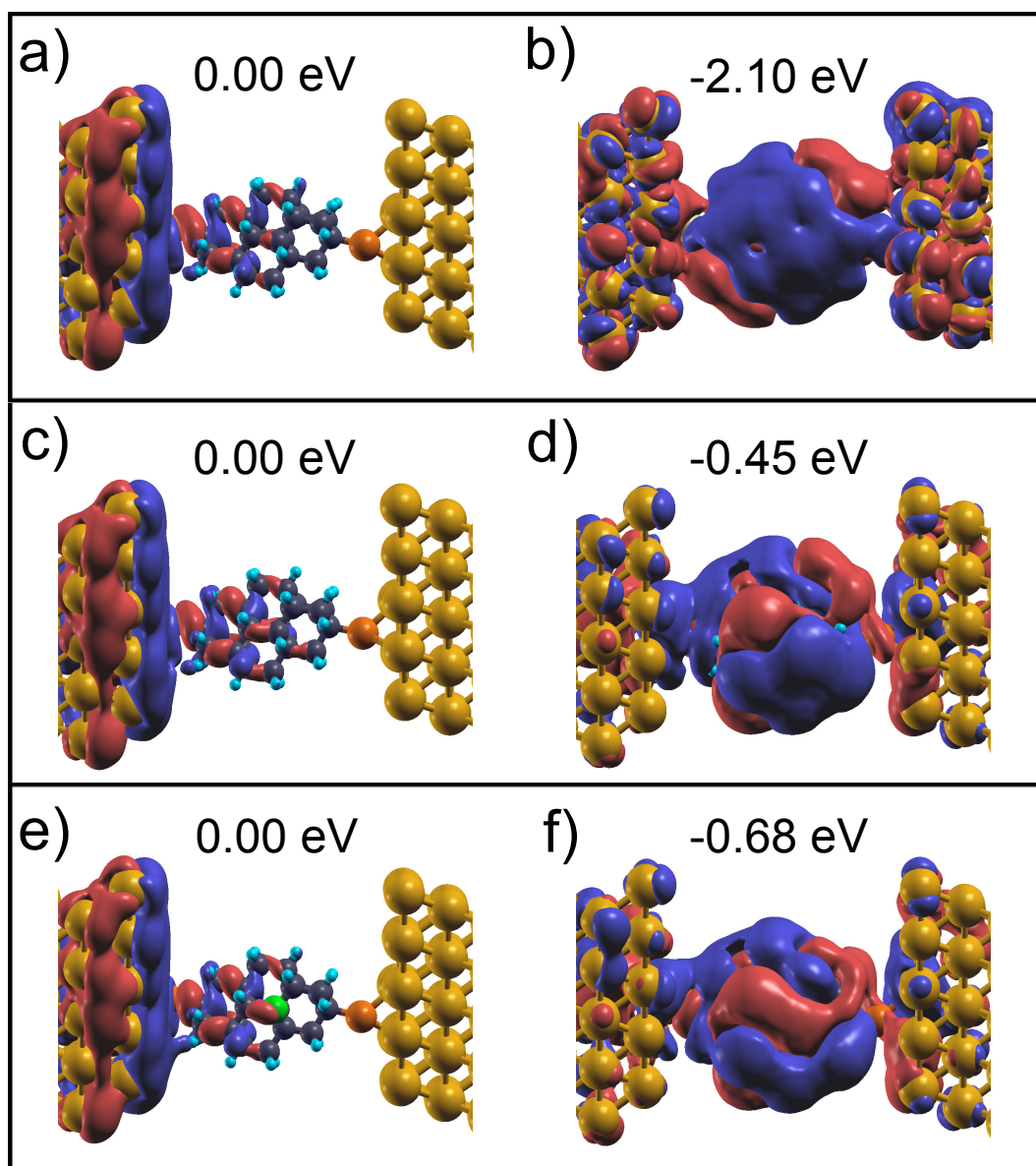


Figure 5.8: Eigenchannel wavefunctions for the dithiol-tetramantane devices: (a-b) undoped dithiol tetramantane, (c-d) N-doped dithiol tetramantane and (e-f) BN-doped dithiol tetramantane each shown at the energy given in the label. '0.00' eV corresponds to the Fermi level. The plots in the right panels correspond to the first transmission peaks (HOMO) below the Fermi level for each setup. For clarity, all wavefunctions are plotted for the same isovalues. Positive values of the wavefunctions are in red and negative in blue.

again manifest, the importance of the different structural characteristics of the molecules on the transport details of the devices. Our results suggest, that a careful choice of the molecule and the gating voltage in the experiments can tune the current flow through such a diamondoid-based molecular device.

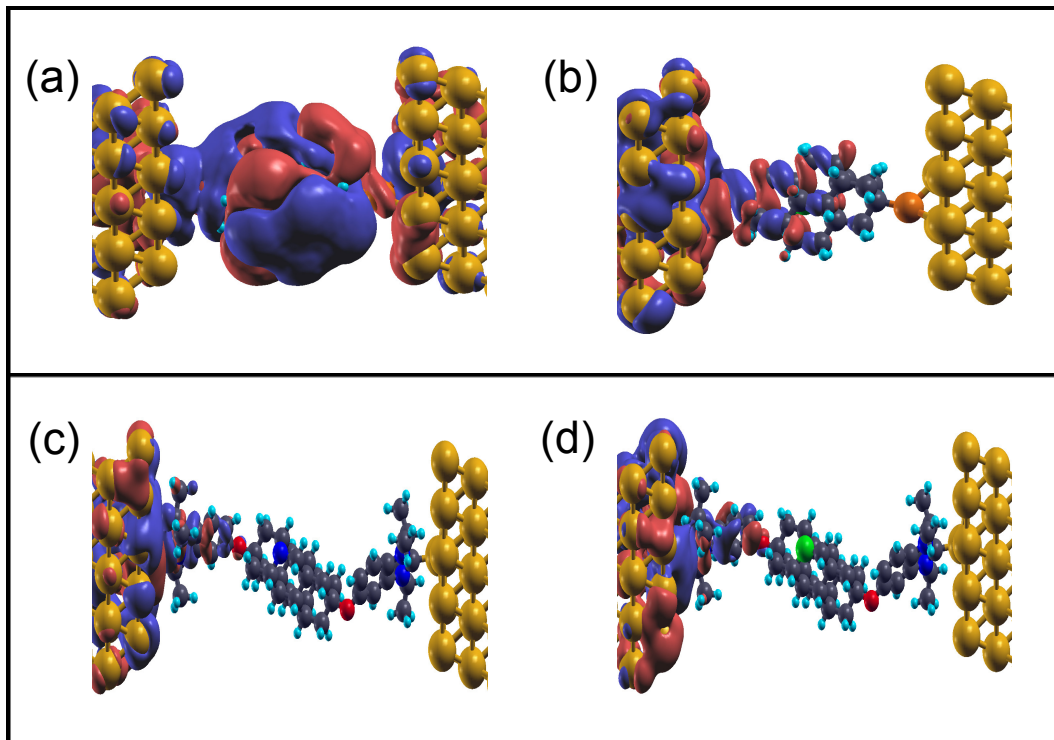


Figure 5.9: Eigenchannel wavefunctions comparing the doped dithiol-tetramantane and doped diNHC-tetramantane cases at the energy (-0.4578 eV) corresponding to the first peak in the transmission of the dithiol N-doped tetramantane. The (a) dithiol N-doped tetramantane, (b) dithiol B-doped tetramantane, (c) diNHC N-doped tetramantane, (d) diNHC B-doped tetramantane are depicted. For clarity, all wavefunctions are plotted for the same isovalues (0.01 eV). Positive values of the wavefunctions are red and negative in blue.

5.3 Current-Voltage Characteristics

As a further analysis to understand the effect of doping, we report on the I-V curve for undoped and N-doped dithiol-tetramantane junctions. We focus on the bias-dependent transport properties of the junctions. We will also report on the shift of the zero-bias 'reference' transmission peak at -0.45 eV seen in (Fig. 5.6 top right panel) with respect to applied voltage bias. The current-voltage (I-V) curves for two different cases a) dithiol tetramantane and b) N-doped dithiol tetramantane are shown in Fig. 5.10. The asymmetric behavior of the current at positive and negative bias in the range $[-0.9, +0.9]$ V for both the junctions, investigated in our work is evident from the I-V characteristic

depicted in the upper panel of Fig. 5.10. The current in both the undoped and doped cases seems to increase with the application of higher bias. There is a clear distinction in the current for the undoped and doped cases. The distinction being that the current in doped case is even more pronounced, when we increase the bias in both positive and negative direction. For the undoped case the current increases and reaches up to a maximum of $\pm 0.087 \mu\text{A}$ for the applied bias voltages. However in the doped case, the current was found to be $-0.124 \mu\text{A}$ for -0.9 V and $0.128 \mu\text{A}$ for $+0.9 \text{ V}$. In order

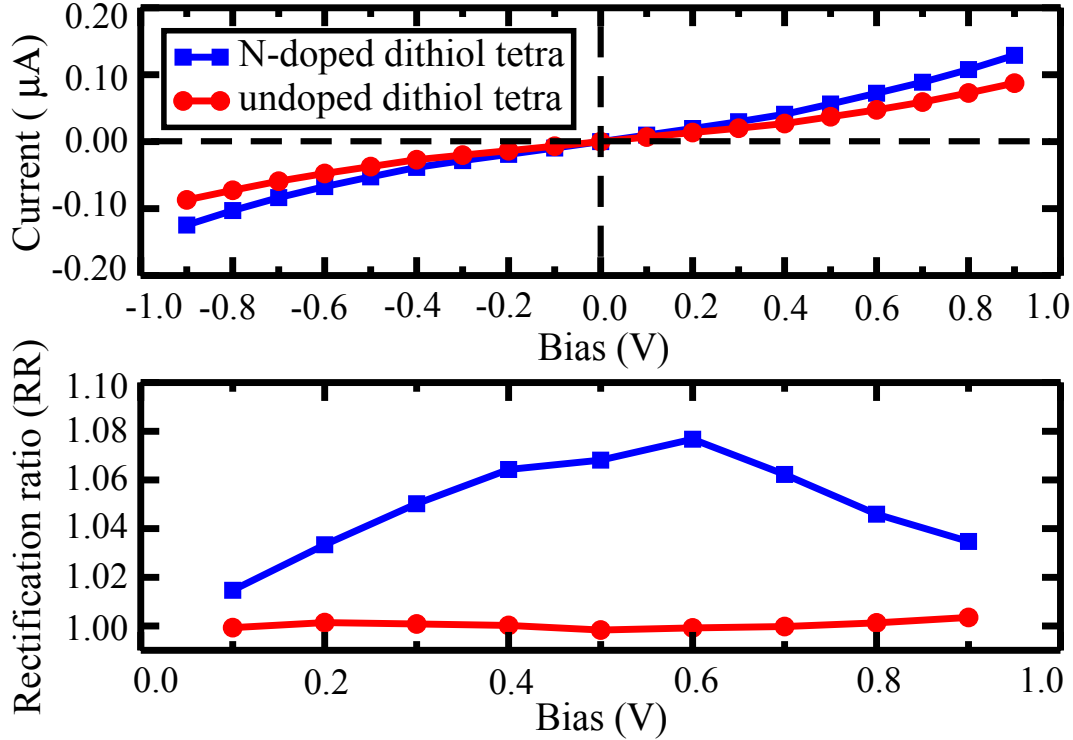


Figure 5.10: I-V characteristics (top panel) and rectification ratio (bottom panel) of undoped dithiol tetramantane (red) and N-doped dithiol tetramantane (blue) based junctions at different bias voltages close to the Fermi level.

to compare the efficiency of doped devices, we have defined the rectification ratio (RR) as : $RR(V) = |I(V)/I(-V)|$. Our aim was to use RR as a means to gain a qualitative understanding of the influence of doping and guide the experiments towards a direction which would certainly affect the rectification. Our work is not intended to fully evaluate in a quantitative way the rectification effect. For this, a more extended study including additional molecules would be needed. The rectification ratios for both the undoped and doped cases are shown in the lower panel of Fig. 5.10. Dithiol N-doped tetramantane-based junctions show a higher rectification ratio for the bias voltages applied in this work as compared to the undoped case. We observe a sharp increase in the rectification from 0.1 V up to 0.4 V. The highest efficiency of the junction is found to be at 0.6 V, at which the rectification ratio is found to be 1.07. There is a sudden drop at 0.7 V where the efficiency decreases up to 1.06. A similar drop is also observed for 0.9 V where the (RR) drops to 1.03. In

the undoped case there is a drop in the (RR) at 0.5 V, but interestingly a minor increase in the efficiency is seen at a higher bias, unlike the doped case. A comparison of the transmission spectra under applied bias is depicted in Fig. 5.11. We present the plots for 0 V, ± 0.6 V, and ± 0.9 V respectively. For both the undoped and N-doped cases, we can observe an increase in the conductance at the Fermi level for ± 0.9 V. We also observe notable peaks for the positive energy range in the transmission spectrum. However, these are not related to the LUMO levels, which are further away from the Fermi level and not in the practically accessible range, as also previously discussed for the zero-bias transmission spectra. At this point, there is no strong indication of the origin of these small peaks and a further investigation is needed. In case of the undoped case the molecular conductance was found to be $2.92 \times 10^{-3} G_0$ for +0.9 V and $2.94 \times 10^{-3} G_0$ for -0.9 V respectively. Similarly, for the doped case the molecular conductance (Fermi level) was found to be $3.15 \times 10^{-3} G_0$ for +0.9 and $3.33 \times 10^{-3} G_0$ for -0.9 V, respectively.

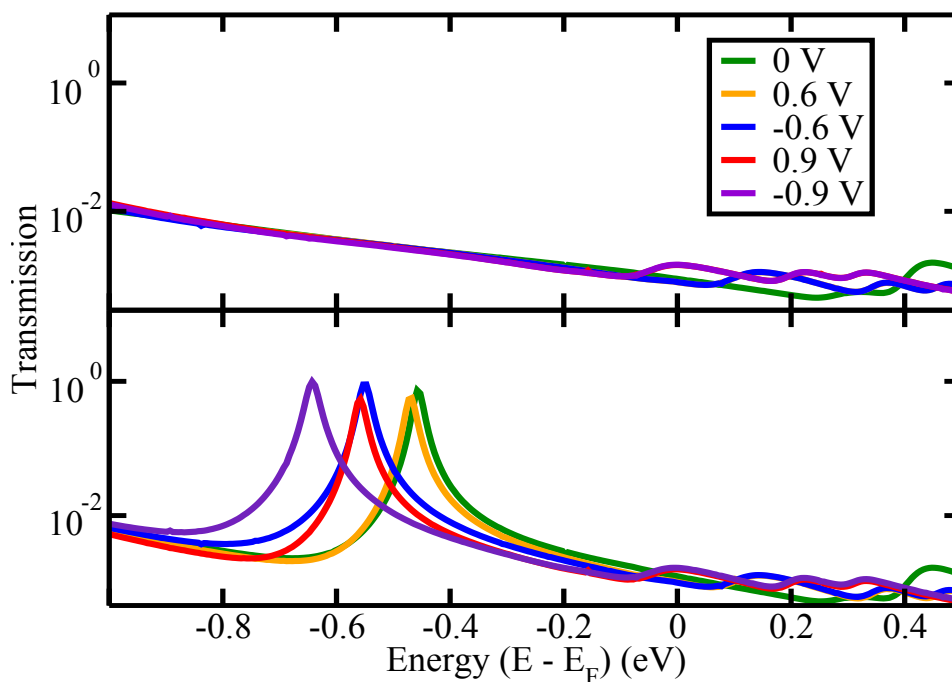


Figure 5.11: Transmission spectra as a function of the applied bias for undoped dithiol tetramantane (top panel) and N-doped dithiol tetramantane (bottom panel).

As observed in the lower panel of Fig. 5.11, there is a characteristic shifting of the zero-bias 'reference' transmission peak with respect to the applied bias. The shift in the positive and negative bias for the N-doped dithiol tetramantane case results in rectification. After the comparison of shift for the reference peaks among symmetric bias voltages (for example: -1, +1 V), we observe that the shift for the positive bias up to 0.6 V is only slightly perturbed with respect to the zero bias reference peak. Further increasing the positive voltage bias moves the reference peak away from the zero bias case towards left. One

can also observe that the bias dependent conductance at the Fermi level for -0.9 is higher compared to its positive counterpart i.e $+0.9$. Combinations of these factors could contribute to lowering of rectification ratios beyond an applied bias of 0.6 V.

5.4 Discussion

Overall, in this chapter we have investigated certain conformations of the modified diamondoids within the gold nano gaps. Our aim was to provide a proof of functioning principles for such molecular junctions. For a more extensive analysis, a conformational scan of the molecules would be needed, which could be the subject of a separate study. If a careful choice of the materials is made, it can lead to highly functional devices with desired properties. Our work indicates that the search for the molecule intended to fill a metallic junction should be made with care, as small modifications in its structure significantly influence the properties of a diamondoid-based molecular device. Finally, we have manifested the use of diamondoids in molecular devices and their rectification effect.

Chapter 6

Conclusions and outlook

The main result of this work is the possibility to selectively tune the electronic, transport, and optical properties of diamondoids by means of structural and chemical modification. Doping and functionalization were used to modify these small diamondoids. Using both DFT and TDDFT, we found out that the tuning of the band gap of these modified diamondoid complexes was possible through doping and/or functionalization. We observe that different dopants and functional groups lead to interesting conduction and optical properties. Double functionalization as compared to a single-functionalization was found to further decrease the band gap moving it closer to the semiconducting region in the ground state and towards the visible region in the excited state. Subsequently, synthesizing diamondoid complexes of a various size and modification has the potential to tune their conduction or optical properties. In terms of industrial applications, the presence of doping and functional groups provides additional functional properties. Functionalized diamondoids include sites which not only tune their properties but also provide binding sites to other structures. The fact that a double functionalization leads to a larger increase in the conduction and optical properties provides the potential to form novel diamondoid-based devices which include one functional group for the attachment of diamondoid on the device and another atomic group which provides the diamondoid with functionalities.

Modelling the adsorption of carbene-functionalized diamondoids on metal surfaces led to interesting results. Two different form of N-hetero-cyclic carbenes were used as an alternative to thiol-based SAMs. Au(111) and Pt(111) were found the most efficient metal surfaces for adsorbing carbene-mediated diamondoid SAMs. Orbitals of d-symmetry were essential in order to have orbital overlapping with carbon p-electrons and bond formation as in the case of the Au(111) and Pt(111) surfaces. In Ag(111), the weaker bonding was justified by the non-availability of the d-orbital of the metallic first layer of the surface around the Fermi level. Calculation of the work functions of carbene-mediated diamondoid SAMs on Au(111), Ag(111), and Pt(111) surfaces demonstrated that the modulation of the work function with respect to the properties of clean metal surfaces and a dynamic tuning can be easily achieved in NHC-ada/metal

devices for organic electronic applications. The charge re-distribution and the simulated STM images of the surfaces showed that on Pt(111) the whole carbene ring of the NHC-ada molecule is associated with the SAM/metal bonding, increasing the adsorption energy of SAMs. By comparing the molecular adsorption energies on reconstructed Au(111), Ag(111), and Pt(111) surfaces, we conclude that these geometries are stable and of practical interest. However, it is essential to examine the thermal stability of these structures and the influence of environmental conditions on their stability. Nevertheless, carbene molecules have proven to be a better alternative to the thiol-based bonding of diamondoids on metallic surfaces, opening up the path for more stable and efficient SAMs/metal devices. Based on these findings and in view of electronic applications such as field emitting devices or sensors, optical properties of carbene-mediated SAMs on metal surfaces need to be investigated.

Electronic transport across molecular junctions made up of functionalized and doped diamondoids were also studied in this work. The comparison of the results was discussed based on the functionalization, the type of dopants, and the size of diamondoid. The dithiol linker group was found to be efficient as compared to a carbene group attached to the Au(111) nano gap. The zero bias transmission function of the undoped diamondoid systems reveals that the HOMO peaks are away from the Fermi level, which is beyond any practical voltage bias window (-1 to +1 V). We have selectively tuned the electronic and transport properties of the diamondoid-based molecular junctions by doping the molecules of boron and nitrogen. The doping with nitrogen leads to an addition of a transmission peak very close to the Fermi level leading to higher molecular conductance. Increasing the diamondoid size leads to a slight decrease in the zero bias conductance. Such a decrease was also observed when using the carbene molecules as a linker of the diamondoid on the nano gap surfaces. Bias dependent transport calculations revealed that doping leads to a higher rectification ratio at very small applied bias voltages. This behavior is the result of the energy shift of the HOMO peaks with respect to the zero bias case. Overall, the rectifying effect in N-doped diamondoids is related to the asymmetry in the structure when introducing the dopant. Since a similar asymmetry is introduced by means of doping in the case of B and B-N co-doping, we can assume that a similar rectifying behavior is observed also for these latter cases. Nevertheless, a separate study needs to be carried out to further quantify these effects.

The investigation carried out here has an impact on the design of novel molecular devices for electronics and sensing applications. A careful choice of the materials can lead to functional devices with desired properties. Our work indicates that the search for the molecule intended to fill a metallic nano gap should be made with care, as small modifications in its structure significantly influence the properties of the molecular device. The use of a simple thiol group for grafting the diamondoid on metal electrodes typically leads to high electronic transmission. When a smaller transmission is desired the use of

molecules such as N-heterocyclic carbene is more suitable. Similarly, when a larger conductance is needed further away from the Fermi level, than the NHC molecule can be more efficient.

Overall, our results have shown that the choice of doping, functionalization, as well as the choice of the molecule in the metal nano gap, could allow a very specific tuning of the whole device by unveiling the electronic functionalities of the single molecules. Specifically, the binding of the molecule on the gold electrodes is crucial in controlling the flow of electrons from one electrode to the other by introducing additional electronic states for promoting the electronic transport and increasing the conductance across the device. Additional investigations should further quantify the effect of structural fluctuations of the molecule in the device on the signal-to-noise ratio in the electronic measurements. This issue was not tackled here but is expected to have a great impact on the efficiency of the molecular device. These investigations need to be supplemented by research at the circuit level in order to prove their optimal functionality. It would also be very interesting to investigate the properties of these modified diamondoids attached to a polymer backbone. Such a study would be very promising in view of practical applications using polymer-based electronics. Based on our findings and in view of electronic applications such as field emitting devices or sensors, optical properties of carbene-mediated SAMs on metal surfaces need to be investigated. In the end, it is chemically possible to produce modified diamondoids of different sizes. What remains to be done is to use these in novel applications along the above lines. This thesis clearly showed the suitability of diamondoids for such applications.

Appendix A

Promoting assembly of carbon onions

In this chapter, we perform atomistic simulations at two levels, classical and quantum-mechanical in order to probe the binding possibilities of the smallest multi-shelled concentric fullerenes, known as *carbon onions*. We focus on the binding behavior of adjacent carbon onions and promote their binding through the addition of vacancies, as well as through doping with boron and nitrogen atoms. Molecular dynamics (MD) simulations are used to address the effect of different conditions of temperature and pressure on the binding of the onions and the thermal stability of the assembled structure. At a smaller scale, density functional theory (DFT) based calculations reveal the electronic structure of the coalesced carbon onions, their charge density, and frontier orbitals. Our main finding is that binding of adjacent carbon onions is promoted through the addition of vacancies and/or dopants on the outer surface of the carbon onions. The results are evaluated with respect to the relative distance between the adjacent carbon onions, the number of vacancies, and the amount or type of doping. We aim to optimize the conditions for assembling these nanoscale building blocks and understand their corresponding electronic properties in view of their potential in nano-assembling novel functional nanomaterials. In section A.2, we present the methodology applied for the study of small carbon onions. Next, in section A.3 we discuss the binding possibilities, various factors which guide coalescence and the corresponding electronic properties and conclude in the final section A.4. This appendix is the part of our published article "B. Adhikari et. al. Phys. Status Solidi A 211, No. 2, 277–287 (2014) Copyright Wiley-VCH Verlag GmbH & Co. KGaA. Reproduced with permission. All rights reserved".

A.1 Introduction

The discovery of novel unconventional forms of carbon with fullerenes [133,134] and carbon nanotubes [135] being the most representative examples led to a potential broader use of carbon materials in various kinds of applications ranging from electronic devices to drug delivery. Within this new era of carbon

materials, *carbon onions* were synthesized [136]. These are concentric multi-shelled fullerene clusters held together by van der Waals forces and are built up of spherical graphene layers of up to a few nanometers in size [137–144]. Carbon onions are considered to be the most stable among the carbon nanostructures [145]. The smaller carbon onion is that with a C_{20} fullerene in the core [146]. The onion-like graphite nanoparticles can occur in a wide range of structures, from polyhedral to nearly spherical ones [147]. The striking importance of these carbon structures is that these can give a complete insight into the mechanism by which carbon atoms rearrange themselves [148]. Carbon onions can also be viewed as nano-building blocks with important applications in nanotechnology. The potential possibilities of tuning the electronic and mechanical properties by stuffing the hollow graphitic onions with metals or also doping the carbon sheets themselves with atoms such as boron seem endless [149, 150]. The spherical structure of carbon onions can be better described through the existence of pentagon-heptagon pairs [151–153], rather than hexagons and heptagons [154, 155]. Continuous loss of atoms due to sputtering induces a self-compression of the spherical carbon onions, which allows diamond to nucleate in the core of the carbon onions [156]. Existing studies have revealed the field emission characteristics [157], conductivity [158], optical and tribological properties of carbon onions [159], their potential use as solid lubricants, gas storage [160], supercapacitor electrode materials [161], while they have good wear behavior, and buckle under hydrostatic pressure [162].

Carbon onions are often produced under extreme conditions and become strongly interlinked or coalesced. This inter-linking is fundamental in understanding new synthetic routes to selected carbon onion sizes and encapsulation compounds. Coalescence is optimal for building novel materials from nano-building blocks like carbon onions and render these particles candidates for molecular electronics and composite materials applications [163]. Coalescence of spherical graphitic-like molecules was observed in nanotubes, where the encapsulated fullerenes self-assembled in chains [164, 165] forming a tubular structure [166]. The fullerene chains, which initially interact through van der Waals forces coalesce into interior tubes after high-temperature annealing [163] or when subjected to high electron flux [167]. Theoretically, the topological rearrangements that lead to coalescence of fullerene cages have been tracked [168]. Fusion of fullerenes can also occur through molecular collision processes [169–171]. Carbon nanotubes have also been observed, both theoretically and analytically, to coalesce. It was found that a zipper-like mechanism for coalescence can proceed through the existence of vacancies on the nanotubes allowing the carbon atoms to reorganize [172]. Along these lines, joining nanoscale units is of fundamental and practical importance. Along these lines, we focus on the bonding possibilities of carbon onions. In order to render carbon onions into building blocks in nanotechnology, a controllable way to connect these units together is needed. It is of high importance to qualitatively understand how the properties of carbon onions are altered because of their coalescence is of importance. In this work, we try to understand and tune the binding possibilities of two adjacent

carbon onions by evaluating the effects of pressure, temperature, the number of vacancies (experimentally induced through electron irradiation), separation distance, as well as amount and type of doping.

A.2 Methodology

A multi-level approach for the investigation of the binding possibilities of small carbon onions. Specifically, the focus is based on the effect of the external conditions on their binding, as well as how this binding influences the electronic properties of the isolated carbon onions. Within our approach, a density-functional theory based simulations, as well as Molecular Dynamics are used. The results obtained from each calculation are complementary and give a wider overview on the binding possibilities of small carbon onions. At the smaller scale, a density functional theory (DFT) based scheme is used as implemented in the SIESTA code [59], in which the Kohn-Sham eigenstates are expanded using a linear combination of atomic orbitals as the basis set. We use norm-conserving Troullier-Martin pseudopotentials [83] and a split valence double zeta polarized basis set. A mesh cutoff parameter (which corresponds to the fineness of the real space grid) of $200Ry$ has been found to be optimal for the calculations. We have been using the exchange-correlation functional VDW-DF2 [173]. Due to the explicit inclusion of a strictly non-local correlation term, this functional is found to describe dispersion interactions with improved accuracy in comparison to a semi-local generalized-gradient-approximation (GGA) functional [174]. The geometry optimization was performed using the conjugate gradient algorithm and the structure was relaxed until forces on the atoms were lower than $0.04 \text{ eV}/\text{\AA}$. We refer to these calculations as static DFT in the following. In addition to the static DFT calculations, we also performed *ab initio* Molecular Dynamics (MD). (We refer to these as *ab initio* MD or DFT-MD in the following sections.) For these simulations, a time step of 1.0 fs was used and the total simulation time varied between 2-5 ps. The temperature was set at 2000 K and a Nosé thermostat was used to ensure that this temperature is reached. No pressure is applied in the DFT simulations.

At a next level, classical Molecular Dynamics simulations are performed as implemented in the code LAMMPS [175], which performs well for materials calculations. For the intra-molecular (among atoms on the same fullerene) interaction, the bond-order Tersoff potential [176] is used. This potential has been widely and efficiently used in simulations of various forms of carbon structures. The Tersoff potential includes also parameters for boron and nitrogen atoms [177], which are used here as dopants. For the inter-molecular (among atoms of the inner and outer fullerenes) interactions, a Lennard-Jones type of potential is implemented. For this potential, parameters are taken which have been previously published in the literature [178]. The simulation box is cubic, with an edge length ranging between 3-10 nm. Periodic boundary conditions are applied and the system is large enough so that finite size effects are not significant. The time step of the simulations was set at 1.0 fs and the typical time

for gathering statistics was 1 ns. Two types of simulations are being performed in order to unveil the role of temperature and pressure in the binding process of the two onions. Accordingly, our simulations are done separately under two statistical ensembles, the (N,V,T) and the (N,P,T) ensemble. We fix always the number of particles N in the (N,V,T) ensemble we fix the pressure at 0 bar and perform different simulations with temperatures ranging from 500 K - 3500 K. Similarly, we set the temperature at 1000 K and 2000 K and perform different simulations with the pressure ranging from 0.01 bar to 10 bar. In our simulations we have used Nosé-Hoover thermostat and barostat. We refer to these calculations as empirical or classical MD in the following sections.

We have applied the computational schemes mentioned above to study the binding possibilities of two small carbon onions, namely two adjacent $C_{20}@C_{96}$. Each onion has an inner fullerene, the C_{20} which is concentric with an outer larger fullerene, the C_{96} . For the C_{96} we randomly chose one of its isomers, namely, #96 with the C_2 point group symmetry. The random choice was based on the fact that all isomers could accommodate the inner C_{20} . We have, though, performed test simulations with another isomer, the $C_{96}(D3h)$ and have seen that the results do not change qualitatively.

We have modelled these small structures instead of larger ones for computational efficiency. The diameter of the carbon onion (the outer C_{96}) is 9.7 Å, while the diameter of the inner (C_{20}) fullerene is 3.7 Å. Accordingly, the distance between the inner and outer fullerenes is about 3.0 Å. Note, that here the smallest carbon onion is modelled and this includes only 5- and 6-fold rings, rather than 6- and 7-fold rings as in the case of larger carbon onions [151–153]. The two carbon onions are placed at close distances. This distance was varied in order to promote the binding more easily and found that an initial 1.8 Å separation could lead to binding of the two carbon onions under specific conditions. Using an initial larger separation would increase the computational time and would also require a collision process, i.e. an initial velocity assigned to each onion in order to move towards each other. We wanted to avoid this and rather placed the carbon onions closer together. Nonetheless, here, we are interested in how changes in the structure of the carbon onions (vacancies, doping) or tuning the temperature or pressure applied, can promote their binding.

Having this goal in mind, we focus on the following systems: (i) an ideal carbon onion, (ii) a carbon onion with vacancies, or (iii) dopants or (iv) carbon onions with dopants and vacancies. The vacancies and dopants are introduced in the outer (C_{96}) fullerene. We vary the number of vacancies from 1 up to 5 on each of the adjacent outer (C_{96}) carbon onion shells. The dopants that were considered are nitrogen and boron. Nitrogen replaces a carbon atom on the outer carbon onion shell, while boron dopes the outer fullerene of the adjacent carbon onion. The two dopants are placed in such a way so that they are exactly opposite each other and could potentially bond. In order to create

the vacancies in cases (ii) and (iv), carbon atoms on the sides of the outer fullerenes which are closest to each other were randomly chosen and removed.

Creating vacancies resembles the irradiation of carbon onions with electrons. The chosen set-up is simplified, but our aim is not to waste computational time in searching for the conditions which could lead to coalescence. Rather we try to bring our structures at optimum distances, with vacancies and dopants at desired sites, so that the carbon onions may eventually bond under certain pressure and temperature conditions. We should also mention here that we have tried to use similar conditions for all the schemes we have used here, and have tried to change one parameter at a time. However, all the methods describe the inter-atomic interactions in a different way. In addition, the thermostat in the *ab initio* MD method is not exactly the same as the ones in MD. We could unfortunately not avoid this as the Nosé-Hoover thermostat is not implemented in the DFT code. Though we expect small deviations in our results and not a significant qualitative difference arising from the different thermostats, we cannot exclude it.

A.3 Results and discussions

In the following, focus is given on two adjacent $C_{20}@C_{96}$. Two of these ideal onions (without vacancies or donors) are taken and placed at different distances ranging from 1.5 to 3.0 Å. As expected, these ideal, unmodified carbon onions repel each other. It is energetically very unfavorable to break the five- and six-fold rings on the carbon onion surface in order to form bonds to the adjacent onion. Accordingly, in order to favor the binding of the two carbon onions, we introduce different kinds of alterations on their structure. We begin with the introduction of vacancies on the outer carbon onion shells and at a next step add dopants again on the outer shells of the carbon onions. The pressure and temperature serve as free parameters to the problem. We fix one of the two and vary the second. The temperature is varied from 500 to 3500 K while the pressure from 0.01 to 10 bar. In all figures, different colors are used to visualize the different fullerene cases of the carbon onions.

A.3.1 Introducing vacancies

Vacancies, which experimentally can be introduced by electron irradiation are introduced on both the outer shells of the onions. The vacant sites are randomly chosen but are always on opposite sides of the carbon onions in order to promote the binding. In principle, irradiation can introduce vacancies on the inner fullerenes as well, which is an additional study we have not focused on here. We have found bonding of the two carbon onions in all the cases.

The results obtained from both *ab initio* DFT and empirical MD reveal a bonding between the two onions, but the picture qualitatively differs as indicated in Fig. A.1, where the results after 2 ps of DFT-MD and classical MD are shown. In both cases, a preferential binding between the two carbon onions is

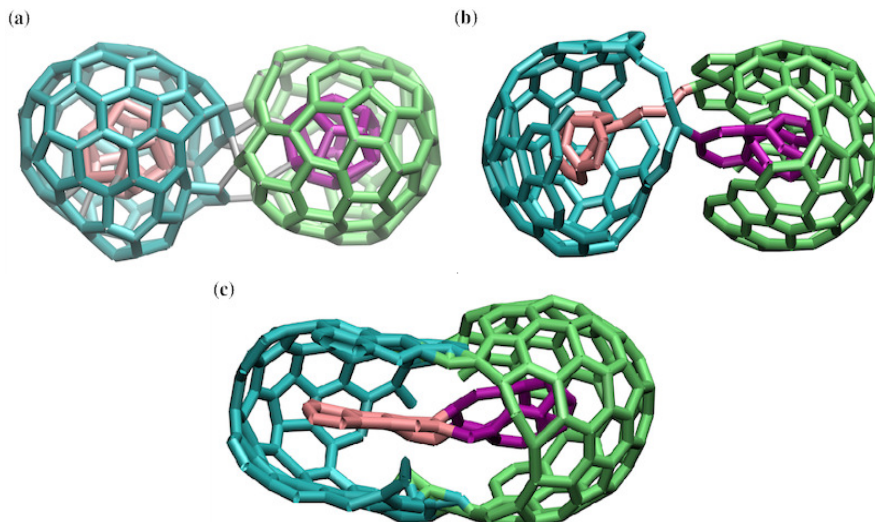


Figure A.1: Snapshots of two $C_{20}@C_{96}$ placed initially at a separation of 1.8 Å. Three vacancies were introduced on each of the outer shells of the carbon onions. The results are obtained through (a) *ab initio* MD, and (b)-(c) empirical MD. In (b) only a temperature of 2000 K was applied, while in (c) a pressure of 0.01 bar was additionally applied for the first 0.01 ns of the simulation. All snapshots correspond to a time of 5 ps. In all cases, the temperature was set at 2000 K. The silver bonds in (a) denote the interlinkings which are formed between the carbon onions.

seen, which results in a more closed form of the *ab initio* MD case and a more open compound in the classical MD case. The different structural details of both results are given through a ring statistics analysis in Fig. A.2. Apart from the 5- and 6-fold rings which compose the initial $2C_{20}@C_{96}$, the DFT description results in a structure with higher order rings only, while in the coalesced structure formed within the classical MD description, also lower (3- and 4-fold rings) exist. These smaller rank rings probably occur due to the unphysical compression by increasing the pressure. Varying the temperature in the empirical MD simulations revealed, that for higher temperatures the inner fullerenes tend to open up, enclosed by the outer C_{96} , which still form a cage-like, but more open structure. The structures start to open up from temperatures of about 1000 K. The two carbon onions do form bonds for all temperatures. It was also observed that the application of pressure for the first 0.01 ns of the classical MD simulations results in a complete bonding than in the case where the only temperature is applied. The result of such a simulation with 0.1 bar applied for the first 0.01 ns and then removed is shown in Fig. A.1(c) for comparison. The temperature was 2000 K. In order to underline the role of pressure as obtained from the classical MD simulations, representative conformations are shown in Fig. A.3. The panels of the figure show random snapshots for the carbon onions with three vacancies each (six in total). The snapshots in this figure correspond to a different amount of pressure, which ranges from 0.01 bar up to 5 bar. In all the cases temperature was set at

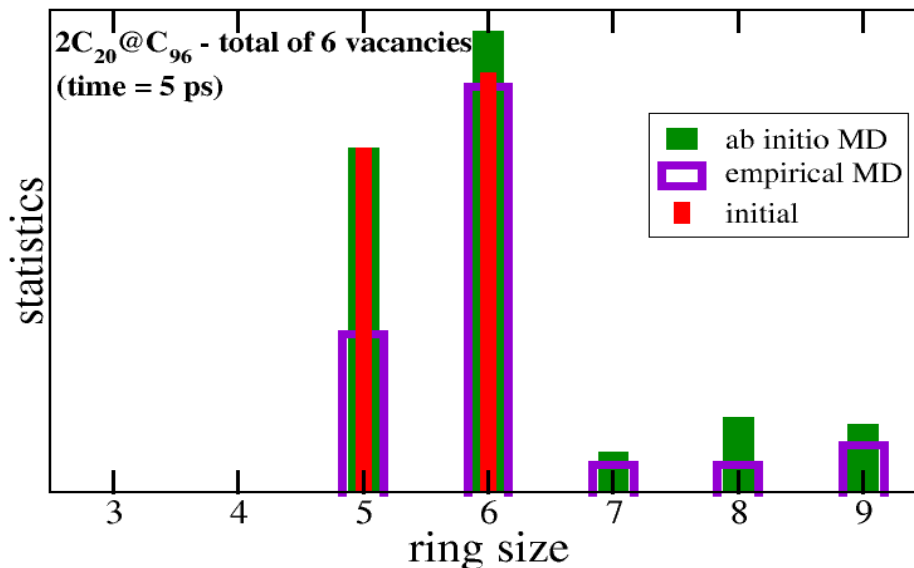


Figure A.2: Ring statistics distributions for the DFT *ab initio* MD and classical MD results depicted in Fig. A.1 after a simulation of 5 ps. The labels '*ab initio* MD' and 'empirical MD' correspond to panels (a) and (b) in Fig. A.1, respectively. The term 'initial' corresponds to the initial structure before the application of either temperature or pressure.

2000 K. Binding of two carbon onions was evident in all cases, but occurred as expected faster for a higher pressure. We present the bonded conformations at a time 5 ps in order to promote comparison to the DFT results shown in Fig. A.1(b). For the smallest pressure applied, 0.01 bar, it was observed that after about 0.02 ns the two carbon onions have already merged. A similar behavior occurred at about 0.01 ns when a pressure of 5 bar was applied. We conclude that a pressure leads to a faster and more complete (more interlinkings between the adjacent carbon onions) bonding, but should not be applied for a long time (not over 5-10 ps) to avoid the collapse of the carbon onions. Coalescence of the neighboring nano units was not exactly perfect, as in most of the cases the outer C₉₆ opens up increasing its diameter, as mentioned above. This opening of the outer fullerene is most likely based on the interplay between the Tersoff and Lennard-Jones potentials used here. The initial distance between the inner and outer fullerenes is close to 3.0 Å. The minimum distance according to the Lennard-Jones potential should be close to 3.4 Å (similar to the inter-layer distance in graphite).

Accordingly, the Lennard-Jones potential tends to increase the inter-onion distance to this value. This is opposed to the Tersoff potential applied to the atoms on the outer fullerene shell, which tends to keep the *sp*² bond distances close to the values for graphite. This interplay leads to a coalesced compound,

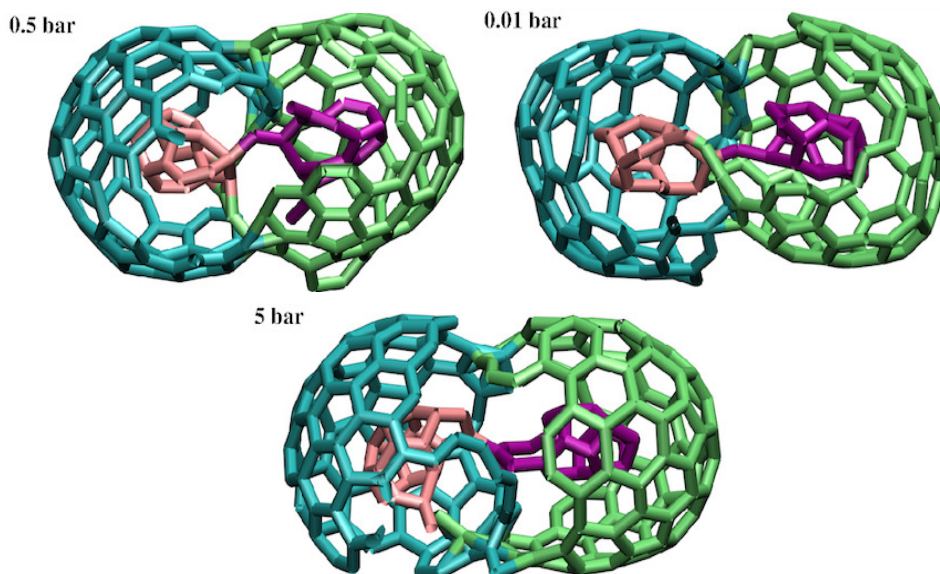


Figure A.3: Snapshots of two $C_{20}@C_{96}$ placed initially at a separation of 1.8 Å on which a different amount of pressure is applied, as indicated from the panels. The temperature is 2000 K and the snapshots correspond to 5 ps of classical MD simulations.

which has a more open form and includes dangling bonds as well. Such a trend was not observed in the DFT results. However, MD captures qualitatively the bonding pathway. Coalescence was indeed observed (in a more complete-closed form) in our DFT simulations. It should also be noted, that we have calculated the mean values of the temperature and pressure in our calculations in order to evaluate the differences between the data that we obtain from the classical and *ab initio* MD simulations. Results are provided for the carbon onions with three vacancies each. The mean temperature in the empirical MD simulations was found to be 2046 K, while the same property in the *ab initio* MD simulations was 2000 K. The averages were done over a time of 5 ps. The average temperature over the total time of 1 ns in the classical MD calculations was 2095 K. For one of the simulations where a pressure of 0.5 bar was applied, the average pressure was 1.15 bar and 0.32 bar over a time of 5 ps and 1 ns, respectively.

A.3.2 Introducing dopants

We further investigate pathways to promote bonding of the carbon onions, by adding dopant atoms on the outer fullerene cage of both carbon onions. Boron-doped fullerene-like shells have been experimentally produced and exhibit a polyhedral faceted circumference [179]. These may occur through irradiation-induced solid-state phase transformation. Other doped carbon onions, such as $C_{48}N_{12}$, have been the core of cross-linked carbon onions grown on a substrate to yield thin solid films ideal for wear-protective applications [180]. Here, two dopant atoms are used, one for each carbon onion and substitute with these

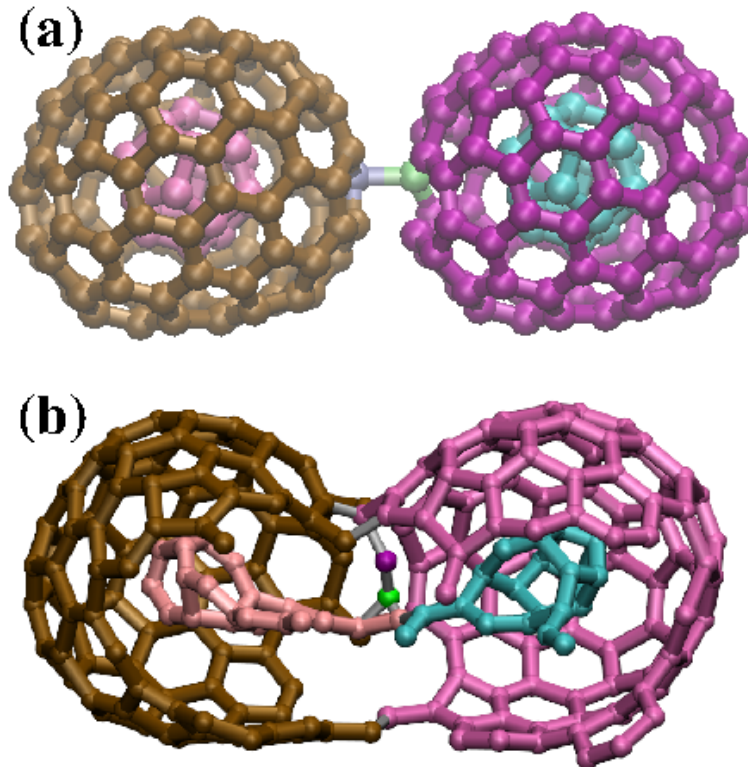


Figure A.4: (a) The initial and (b) final (after a 5 ps) structures of doped carbon onions with an additional vacancy on each C_{96} . The graph shows the ring statistics analysis for these two structures. No pressure is applied and the temperature is 2000 K. The different coloring corresponds to the different fullerene cages and the dopant atoms. The silver bonds denote the interlinks between different fullerene cages and the dopants. The results are obtained through the classical MD simulations.

two carbon atoms. A reasonable choice is to choose elements, such as boron and nitrogen, which are similar (in atomic size) to carbon. A similar scheme for functionalization was used in the case of diamondoids [15], nano-building blocks made up from diamond cages. This choice is also justified by another study which studied the substitution of carbon atoms by nitrogen and boron in fullerenes and nanotubes [181]. Similarly to that work, we substitute a carbon atom on the outer shell of an onion with a boron and that of its adjacent carbon onion with a nitrogen atom. Both dopant atoms are placed on opposite sides of the carbon onions and are the nearest neighbors atoms of the neighboring carbon onions. Vacancies are again introduced on both outer fullerenes. It is expected that this substitution will enhance the binding of the two carbon onions as it should result in a much stronger bond between the two doped carbon onions. Temperature and pressure are again varied separately. It is first observed, that in the case of doped carbon onions an elevated temperature of 2000 K is sufficient to promote the binding of the adjacent structures. The results are shown in Fig. A.4 for the doped carbon onions which also include

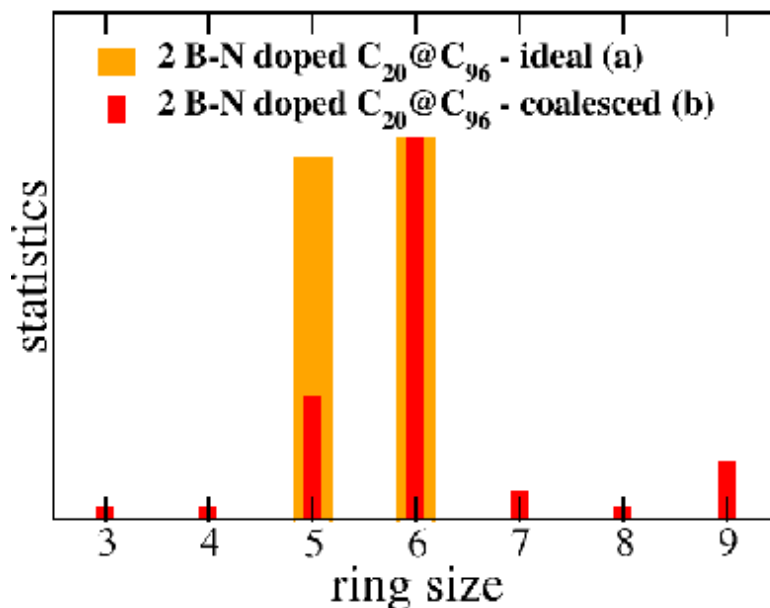


Figure A.5: (a) The initial and (b) final (after a 5 ps) structures of doped carbon onions with an additional vacancy on each C₉₆. The graph shows the ring statistics analysis for these two structures. No pressure is applied and the temperature is 2000 K. The different coloring corresponds to the different fullerene cages and the dopant atoms. The silver bonds denote the interlinks between different fullerene cages and the dopants. The results are obtained through the classical MD simulations.

two vacancies. The initial structure is also sketched together with the relevant ring statistics analysis. Doped coalesced carbon onions form very few lower order rings and higher order ones as in the undoped carbon onions discussed in Fig. A.2.

The effect of pressure and temperature on differently doped carbon onions was also investigated. The results are shown in Fig. A.6 for doped carbon onions each with one or two additional vacancies, respectively. In all cases, binding of the outer fullerene shells occurs, together with the interlinking of the two inner fullerenes. The difference among the cases shown lies on the structure of the inner C₂₀s. These can be almost spherical, quite elongated, or open up and become planar. This planarity occurs when parts of the outer fullerene also tend to become planar. This occurs as the number of vacancies increases and the very stable curved sp² cages try to transform to a very stable graphite-like structure. This is though to a large extent prevented due to the bonding of the adjacent fullerenes. As a general remark regarding the doped carbon onions, it was surprising to realize that the boron and nitrogen atoms do efficiently promote the binding of adjacent carbon onions. The addition of dopants has a larger effect on the coalescence of the adjacent nanostructures as solely the addition of vacancies.

It was also very interesting to observe the following trend, which cannot be

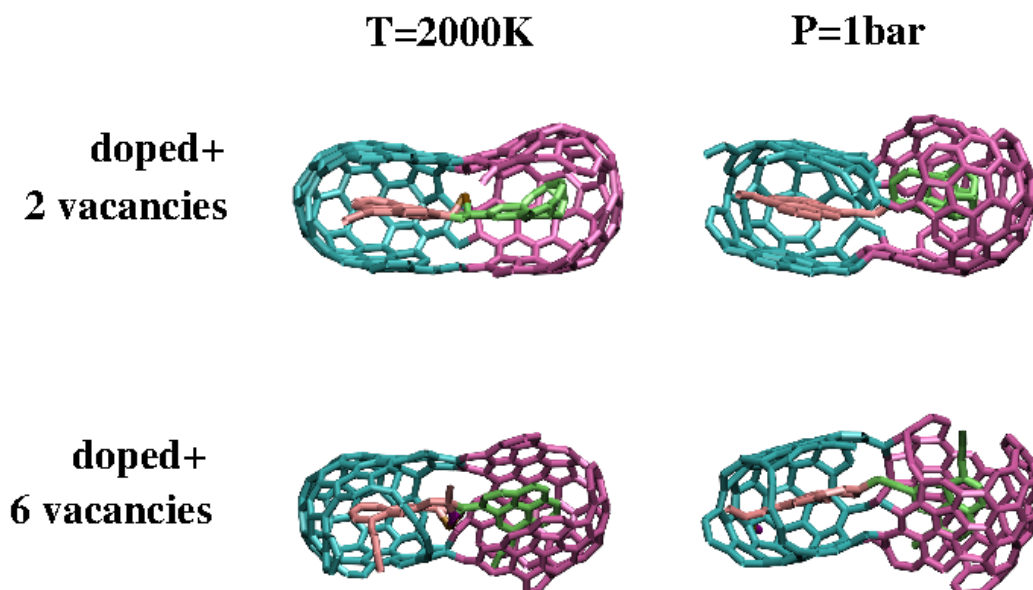


Figure A.6: Snapshots of two doped $C_{20}@C_{96}$ placed initially at a separation of 1.8 \AA . The snapshots correspond to 0.1 ns simulation time. Different conformations occur when either temperature or pressure are applied to these molecules, as denoted by the labels in the panels. The results are obtained through the classical MD simulations

easily visualized in Fig. A.6: when only temperature is applied the boron and nitrogen atoms remain bonded with some of the atoms, typically the ones from the inner C_{20} s. On the other hand, when pressure is applied, though these dopants still promote binding between the adjacent carbon onions, once binding has occurred the dopants are then "expelled" from the coalesced molecule. Boron and nitrogen at the either edges of carbon onions are strong donor and acceptors and have a high tendency to bind first. The carbon atoms that come along and form new bonds, tend to form these bonds with other carbon atoms and not the dopants. The carbon atoms which bond to the dopants, similarly prefer binding with other carbon atoms instead. A similar trend was previously shown, as the carbon-carbon bond is preferred against the carbon-nitrogen or carbon-boron bonds in carbon structures [182]. In our investigations, though, the carbon-carbon bonding is preferred when pressure is also applied and not temperature alone.

A.3.3 Electronic properties

At a next step, the electronic properties of a carbon onion are compared to those of the fullerenes that make up the carbon onion. The results discussed in this section are obtained through quantum mechanical simulations: static and MD. The electronic properties are probed through the electronic density of states and the frontier orbitals. The latter refer to the highest-occupied

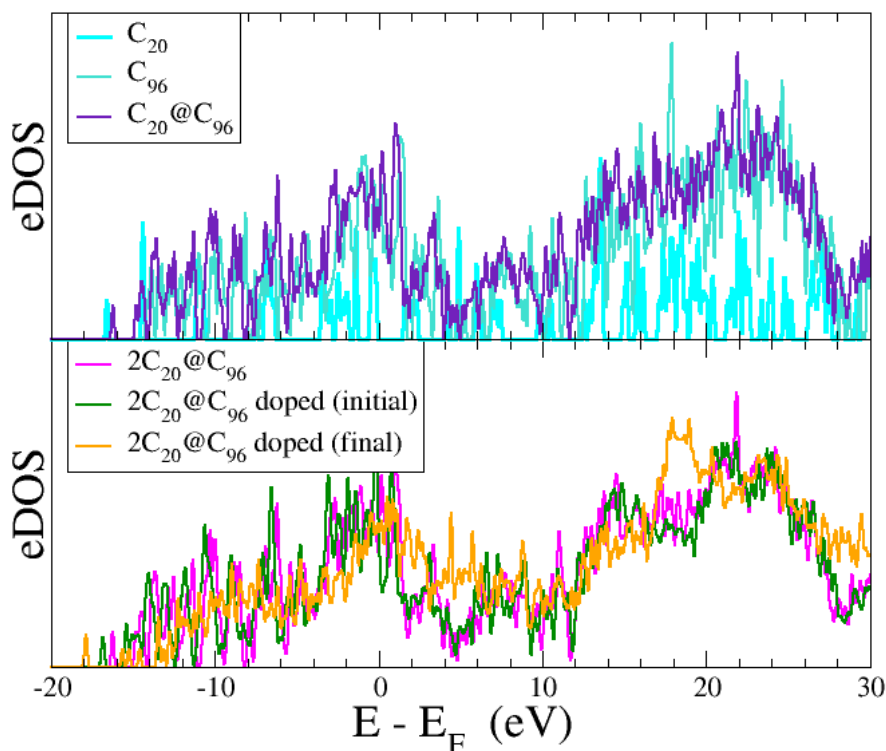


Figure A.7: Electronic density of states (eDOS) for the fullerenes that form the carbon onion, C_{20} and C_{96} , for $C_{20}@C_{96}$, as well as the two adjacent doped $C_{20}@C_{96}$ having each an additional vacancy. Results for both the initial 2 $C_{20}@C_{96}$ and final 2 $C_{20}@C_{96}$ are given. The Fermi energy has been shifted to zero. The results are obtained through the *ab initio* MD simulations and correspond to a 5 ps simulation time.

molecular (HOMO) and lowest unoccupied molecular orbitals (LUMO), which are involved in the bonding of two structures.

The electronic density of states (eDOS) of the ideal C_{20} , C_{96} , and $C_{20}@C_{96}$ are sketched in Fig. A.7 together with the doped carbon onions with one vacancy each. These are obtained from the static DFT calculations, where only energy minimization was performed. In the same figure, we show results for two doped carbon onions before and after the *ab initio* MD simulation. The results for the initial configuration resemble the data for the ideal carbon onion. The eDOS of the final coalesced carbon onions, though, is being considerably altered by the exact presence of the interlinks between the two adjacent carbon onions. In order to evaluate qualitatively how the eDOS was altered through binding, we have turned to the projected density of states (PDOS) for the outer and inner fullerenes. The results are summarized in Fig. A.8. The total density of states is also shown for comparison. The main contribution in the total density of states comes from the outer C_{96} of the carbon onions. We also track the atoms of the different fullerenes in the carbon onions, which are involved in

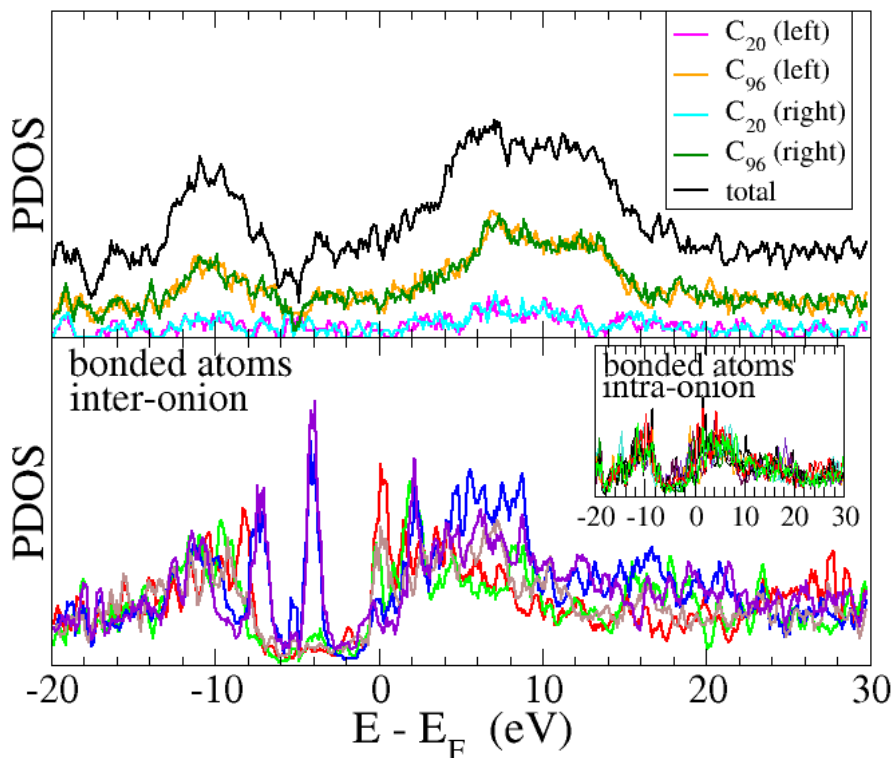


Figure A.8: Partial (projected) density of states (PDOS) for the carbon onions with three vacancies each. The upper panel shows the PDOS of different fullerenes consisting the carbon onions after the bonding has occurred. The lower panel shows the PDOS of all the bonded atoms corresponding to the inter-carbon onion binding. The inset shows the PDOS of the bonded atoms, which correspond to the intra-carbon onion binding (see text). The Fermi energy has been shifted to zero. The results are obtained through 5 ps of *ab initio* MD simulations.

the bonding of the two carbon onions and present the PDOS of these representative atoms in the same figure. This contribution is divided into two parts: the PDOS of the atoms involved in the bonding of the two carbon onions and the PDOS of the atoms of the different fullerenes in each carbon onion which form bonds. The former correspond to the inter-carbon onion bonding and the latter correspond to the intra-carbon onion bonding and are shown in the lower panel of the figure and its inset, respectively. Regarding the contribution of the atoms that are involved in the carbon onion coalescence, we could not observe any specific signatures. Only a peak coming from the bonded atoms of the molecule is observed.

In order to understand in more detail the bonding behavior of the doped carbon onions their frontier orbitals, which are essential for understanding the coalescence are shown in Fig. A.9. These are compared to the orbitals for C_{20} , C_{96} , and $C_{20}@C_{96}$ in the same figure. Inspection of this figure reveals the

change in the HOMO, LUMO orbitals when two carbon onions are brought together. This change is more pronounced when these carbon onions include defects. It is interesting to observe that when defects such as vacancies are introduced on the carbon onion surfaces the frontier orbitals of the neighboring carbon onions overlap. This is an indication, that the binding of the carbon onions can easily be triggered, as long as certain conditions are reached, as for example an elevated temperature. In essence, this can be described by the frontier molecular orbital theory [183], which states that the occupied orbitals of one molecule and the unoccupied orbitals of another molecule interact with each other causing attraction. In this case, the two molecules - here the carbon onions - clearly interact with each other. Similar results for the doped carbon onions with one vacancy each are presented and compared to the distributions of the frontier orbitals before and after the *ab initio* MD simulations, that is the initial and final configuration after 5 ps. The frontier orbitals are sketched in Fig. A.10 in a 3-D representation. These orbitals are also represented as 2-D contours on a plane passing through the midpoint along the direction where the coalescence occurs. There is again a higher "activity" close to the doped/defect regions clearly evident in both these representations. The frontier orbitals become more confined in the final coalesced case, and the electrons are more localized close to the interlinks. In fact, the LUMO states are associated with the inner C_{20} , while the HOMO is extended on the C_{96} and close to the center of the coalesced compound. This HOMO state is strongly involved in the bonding between the outer C_{96} s.

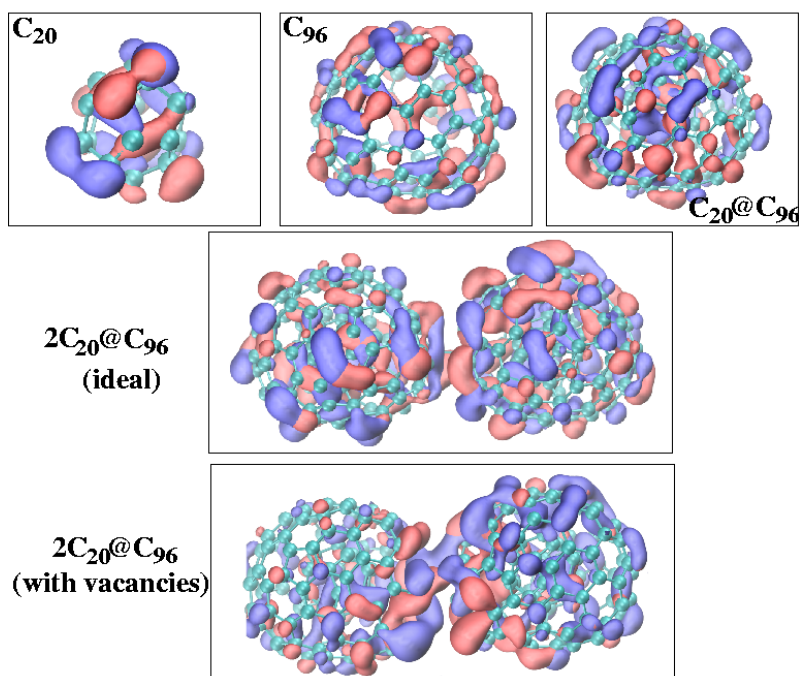


Figure A.9: The frontier orbitals (HOMO, LUMO) for the molecules labelled in the panels. The results are obtained through the static DFT simulations

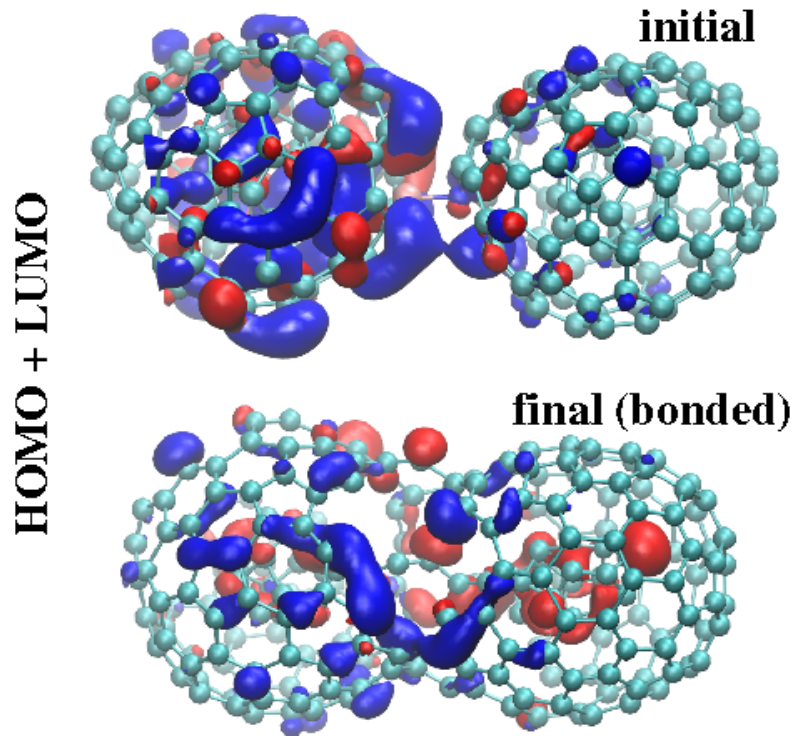


Figure A.10: The 3-D iso-surfaces of the frontier orbitals (HOMO, LUMO) for the doped carbon onions with one additional vacancy on each structure. The results are shown for the initially generated (upper panel) and the final MD structure (lower panel), respectively. The results are obtained through the *ab initio* MD simulations and correspond to a simulation time of 2 ps and a temperature of 2000 K.

A.4 Summary and conclusions

In summary, in this work we have studied the binding possibilities of small concentric carbon onions. Binding is promoted by introducing vacancies and/or dopants on the outer surfaces of the carbon onions and in some cases also by applying pressure and/or increasing temperature. Binding could potentially also be promoted by other ways, such as Stone-Wales defects on the carbon onions, but this was not the subject of this work. Focus was given to the quantification of the factors that guide the coalescence of two carbon onions. The structural and electronic properties of the coalesced carbon onions were analyzed. Although binding was promoted under different structural (vacancies, dopants) and external (temperature, pressure) conditions as mentioned above, the bonding characteristics of the two carbon onions do differ. An additional detailed insight on these characteristics was gained by analyzing the electronic properties, such as the total and partial electronic density of states and the frontier orbitals. Through these, the distribution of the frontier states was revealed. These orbitals are involved in the coalescence and are distributed

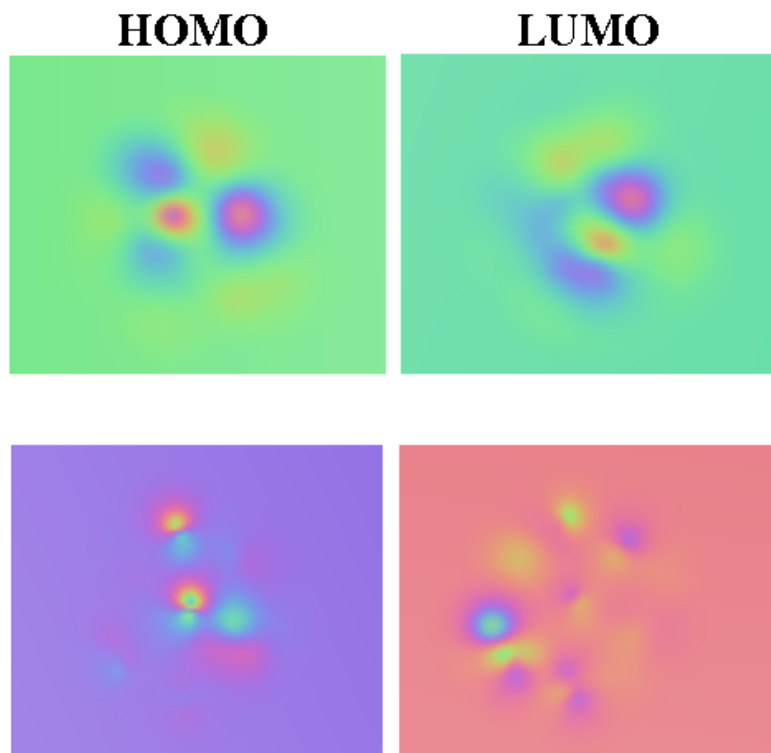


Figure A.11: The 2-D contours are shown along the bonding direction of the two $C_{20}@C_{96}s$ and exactly at the midpoint. The results are obtained through the *ab initio* MD simulations and correspond to a simulation time of 2 ps and a temperature of 2000 K.

closely to the interface between the two carbon onions.

Overall, it was found that the presence of dopants more effectively leads to coalescence of the carbon onions compared to the introduction of vacancies alone. An elevated temperature is sufficient to promote the coalescence and the application of pressure leads to a faster and a complete bonding of the carbon onions. Most importantly, when only temperature is applied, the resulting coalesced compound is more stable and does not include any unphysical bonding as sometimes introduced due to the presence of pressure. The effect of the van der Waals forces in the binding was also evaluated and can potentially also lead to the formation of a small nanotube. Finally, small carbon onions were included in our studies for computational efficiency. Our aim was to indicate a coalescence pathway and present a proof of principles regarding the binding of two small nano-units, like the carbon onions. This study can be further expanded to include higher order carbon onions with additional defects/vacancies or dopant atoms, which are expected to enhance the functionalization of these as well as similar nano-carbons.

List of Tables

3.1	Structural properties of ideal and functionalized adamantane. Bond lengths are given in Å and angles in degrees.	40
3.2	Structural properties of ideal and functionalized diamantane. Bond lengths are given in Å and angles in degrees.	44
4.1	Structural properties and adsorption energies (E_{ads}) for the carbene-mediated diamondoid SAMs on metal surfaces	56
4.2	Bader charge analysis comparing the charges on the SAM and the metal surfaces before and after adsorption	64
5.1	Conductance in units of $2e^2/h$ at zero bias for the modified diamondoid junction at the Fermi level	77

List of Figures

1.1	Different sizes and shapes of diamondoids are shown	3
1.2	Fused diamond cages along the tetragonal axes of the bulk diamond	3
1.3	Illustration of a self-assembled monolayer of diamondoid	4
2.1	General sketch of a pseudopotential	13
2.2	The SCF algorithm implemented in DFT.	14
2.3	The schematic arrangement of a molecular junction	17
3.1	Ideal, doped, single- and double-functionalized diamondoids are sketched	25
3.2	Variation of bond length and bond angle of doped adamantane	27
3.3	Variation of the substitution energies for doped and functionalized adamantane	28
3.4	Electronic density of states (eDOS) for doped and functionalized adamantane	28
3.5	The frontier orbitals for the ideal, doped, and functionalized adamantane	30
3.6	2-D contour plots for ideal, doped, and functionalized adamantane	31
3.7	Electronic band gap for doped, single, and double-functionalized adamantane	32
3.8	The electronic density of states (eDOS) for the ideal and double-functionalized tetramantane isomers	33
3.9	The electronic band gaps for the ideal and double-functionalized tetramantane structures	34
3.10	Frontier orbitals for the four double functionalized tetramantane isomers	34
3.11	The variation of band gap for double-functionalized for higher diamondoids	35
3.12	2-D contour plots for double-functionalized higher diamondoids	36
3.13	Electronic density of states for the double-functionalized higher diamondoids	37
3.14	Optimized geometries of ground state and excited state of doped and functionalized adamantane	39
3.15	Excited state geometries, HOMO, and LUMO of ideal and functionalized adamantane	41
3.16	Absorption spectra for ideal, single, and double-functionalized adamantane	42

3.17	Optimized geometries of the ground state and excited state of doped and functionalized diamantane	43
3.18	Excited state geometries, HOMO, and LUMO of ideal and functionalized diamantane	46
3.19	Absorption spectra for ideal, single and double functionalized diamantane	48
3.20	The variation of the optical band gap for functionalized adamantane and diamantane	48
3.21	Frontier orbitals at the ground state and excited state for both adamantane and diamantane	49
4.1	General structural formula of imidazolylidene-structures	52
4.2	The NHC1-functionalized adamantane (left) and the NHC2-functionalized adamantane (right).	53
4.3	Adsorption of diamondoids on metal surfaces	54
4.4	Charge density of HOMO and LUMO	58
4.5	Projected density of states (PDOS) for both carbene-functionalized adamantane molecules before adsorption	59
4.6	Projected density of states (PDOS) for both carbene-functionalized adamantane molecules after adsorption	60
4.7	Total density of states (TDOS) of the NHC1 and NHC2 molecules	61
4.8	Contributions of the s-, p-, and d-orbitals to the PDOS of the metal surfaces	62
4.9	Plane averaged electrostatic profiles of the two different configurations of carbene-functionalized adamantane SAMs on all three surfaces	63
4.10	Simulated STM images of the systems after adsorption on metal surfaces	65
4.11	Re-distribution of the charge density after adsorption on metal surfaces	66
5.1	A general setup for the transport calculations	69
5.2	The relaxed atomic structures of the dithiol-molecules which will be inserted in the gold nano gap	70
5.3	The relaxed atomic structures of the dicarbene-molecules which will be inserted in the gold nano gap.	71
5.4	Final relaxed structures of dithiol-tetramantane and diNHC-tetramantane in between gold layers	73
5.5	Partial density of states (PDOS) for the dithiol- and N-doped tetramantane molecular junctions	76
5.6	The zero-bias transmission function is plotted on a semi-log scale for all diamondoid-based devices	77
5.7	Bar charts of the conductance at zero bias for the modified-diamondoid nano gaps at the Fermi level	78
5.8	Eigenchannel wavefunctions for the dithiol-tetramantane devices	80
5.9	Eigenchannel wavefunctions comparing the doped dithiol-tetramantane and doped diNHC-tetramantane cases	81

5.10	I-V characteristics and rectification ratio of undoped dithiol tetramantane and N-doped dithiol tetramantane based junctions	82
5.11	Transmission spectra as a function of the applied bias for undoped dithiol tetramantane (top panel) and N-doped dithiol tetramantane (bottom panel).	83
A.1	Snapshots of two $C_{20}@C_{96}$ placed initially at a separation of 1.8 Å.	93
A.2	Ring statistics distributions for the DFT <i>ab initio</i> MD and classical MD	94
A.3	Snapshots of two $C_{20}@C_{96}$ placed initially at a separation of 1.8 Å with applied pressure	95
A.4	Initial and final structures of doped carbon onions with vacancy	96
A.5	Ring statistics of initial and final structures after 5 ps	97
A.6	Snapshots of two doped $C_{20}@C_{96}$ placed initially at a separation of 1.8 Å	98
A.7	Electronic density of states (eDOS) for the fullerenes that form the carbon onion	99
A.8	Partial (projected) density of states (PDOS) for the carbon onions with three vacancies each	100
A.9	The frontier orbitals (HOMO, LUMO) for ideal carbon onions and carbon onions with vacancies	101
A.10	The frontier orbitals (HOMO, LUMO) for the doped carbon onions with one additional vacancy on each structure	102
A.11	The 2-D contours are shown along the bonding direction of the two $C_{20}@C_{96}$ s and exactly at the midpoint	103

Bibliography

- [1] A. T. Balaban and P. V. R. Schleyer, *Tetrahedron* **34**, 3599 (1978).
- [2] H. Schwertfeger, A. Fokin, and P. Schreiner, *Angewandte Chemie International Edition* **47**, 1022 (2008).
- [3] Y. Lifshitz *et al.*, *Science* **297**, 1531 (2002).
- [4] J. E. Dahl, S. G. Liu, and R. M. K. Carlson, *Science* **299**, 96 (2003).
- [5] M. Yao *et al.*, *Carbon* **49**, 1159 (2011).
- [6] J. Zhang *et al.*, *ACS Nano* **6**, 8674 (2012).
- [7] S. B. Legoas, R. P. B. dos Santos, K. S. Troche, V. R. Coluci, and D. S. Galvão, *Nanotechnology* **22**, 315708 (2011).
- [8] J. B. Crumpton and W. L. Santos, *Chem. Commun.* **48**, 2018 (2012).
- [9] G. Sivaraman and M. Fyta, *Nanoscale* **6**, 4225 (2014).
- [10] W. L. Yang *et al.*, *Science* **316**, 1460 (2007).
- [11] S. Roth *et al.*, *Chemical Physics Letters* **495**, 102 (2010).
- [12] J. E. Dahl *et al.*, *Angewandte Chemie International Edition* **49**, 9881 (2010).
- [13] Y. Wang *et al.*, *Nat Mater* **7**, 38 (2008).
- [14] G. Zhang, *Physics Today* **66** (2013).
- [15] G. C. McIntosh, M. Yoon, S. Berber, and D. Tománek, *Phys. Rev. B* **70**, 045401 (2004).
- [16] Y. Xue and G. A. Mansoori, *International Journal of Molecular Sciences* **11**, 288 (2010).
- [17] J. Reiser, E. McGregor, J. Jones, R. Enick, and G. Holder, *Fluid Phase Equilibria* **117**, 160 (1996).
- [18] L. Landt *et al.*, *The Journal of Chemical Physics* **132** (2010).
- [19] L. Landt *et al.*, *The Journal of Chemical Physics* **132** (2010).

- [20] N. D. Drummond, A. J. Williamson, R. J. Needs, and G. Galli, *Phys. Rev. Lett.* **95**, 096801 (2005).
- [21] U. Drechsler, B. Erdogan, and V. M. Rotello, *Chemistry - A European Journal* **10**, 5570 (2004).
- [22] B. D. Gates *et al.*, *Chemical Reviews* **105**, 1171 (2005).
- [23] R. G. Nuzzo and D. L. Allara, *Journal of the American Chemical Society* **105**, 4481 (1983).
- [24] J. C. Love, L. A. Estroff, J. K. Kriebel, R. G. Nuzzo, and G. M. Whitesides, *Chemical Reviews* **105**, 1103 (2005).
- [25] C. D. Bain *et al.*, *Journal of the American Chemical Society* **111**, 321 (1989).
- [26] A. D. Jewell, H. L. Tierney, and E. C. H. Sykes, *Phys. Rev. B* **82**, 205401 (2010).
- [27] D. V. Leff, L. Brandt, and J. R. Heath, *Langmuir* **12**, 4723 (1996).
- [28] D. I. Gittins and F. Caruso, *Angewandte Chemie International Edition* **40**, 3001 (2001).
- [29] C. Vericat, M. E. Vela, G. Benitez, P. Carro, and R. C. Salvarezza, *Chem. Soc. Rev.* **39**, 1805 (2010).
- [30] J. J. Gooding and S. Ciampi, *Chem. Soc. Rev.* **40**, 2704 (2011).
- [31] J. Noh, H. S. Kato, M. Kawai, , and M. Hara, *The Journal of Physical Chemistry B* **110**, 2793 (2006).
- [32] L. Srisombat, A. C. Jamison, and T. R. Lee, *Colloids and Surfaces A: Physicochemical and Engineering Aspects* **390**, 1 (2011).
- [33] C. Vericat, G. A. Benitez, D. E. Grumelli, M. E. Vela, and R. C. Salvarezza, *Journal of Physics: Condensed Matter* **20**, 184004 (2008).
- [34] D. R. Hartree, *Mathematical Proceedings of the Cambridge Philosophical Society* **24**, 89 (1928).
- [35] P. E. Blöchl, *Phys. Rev. B* **50**, 17953 (1994).
- [36] J. Callaway, *Phys. Rev.* **97**, 933 (1955).
- [37] D. R. Hamann, M. Schlüter, and C. Chiang, *Phys. Rev. Lett.* **43**, 1494 (1979).
- [38] P. Hohenberg and W. Kohn, *Phys. Rev.* **136**, B864 (1964).
- [39] M. Born and R. Oppenheimer, *Annalen der Physik* **389**, 457 (1927).

- [40] W. Kohn and L. J. Sham, *Physical Review* **140**, A1133 (1965).
- [41] J. P. Perdew, *Phys. Rev. Lett.* **55**, 1665 (1985).
- [42] S. K. Ghosh and R. G. Parr, *Phys. Rev. A* **34**, 785 (1986).
- [43] A. D. Becke, *The Journal of Chemical Physics* **98** (1993).
- [44] O. Gunnarsson, M. Jonson, and B. Lundqvist, *Physics Letters A* **59**, 177 (1976).
- [45] J. P. Perdew, K. Burke, and M. Ernzerhof, *Phys. Rev. Lett.* **77**, 3865 (1996).
- [46] V. Fock, *Zeitschrift für Physik* **61**, 126 (1930).
- [47] A. Dreuw, J. L. Weisman, and M. Head-Gordon, *The Journal of Chemical Physics* **119**, 2943 (2003).
- [48] J. N. Harvey, *Physical Chemistry C* **102**, 203 (2006).
- [49] L. O. Wagner, E. M. Stoudenmire, K. Burke, and S. R. White, *Phys. Chem. Chem. Phys.* **14**, 8581 (2012).
- [50] E. M. Stoudenmire, L. O. Wagner, S. R. White, and K. Burke, *Phys. Rev. Lett.* **109**, 056402 (2012).
- [51] E. Fermi, *Rend. Accad. Naz. Lincei* **6**, 32 (1927).
- [52] N. Troullier and J. L. Martins, *Phys. Rev. B* **43**, 1993 (1991).
- [53] D. Vanderbilt, *Phys. Rev. B* **41**, 7892 (1990).
- [54] G. Kresse and J. Furthmüller, *Phys. Rev. B* **54**, 11169 (1996).
- [55] P. Giannozzi *et al.*, *Journal of Physics: Condensed Matter* **21**, 395502 (19pp) (2009).
- [56] X. Gonze *et al.*, *Computer Physics Communications* **180**, 2582 (2009).
- [57] F. Bloch, *Zeitschrift für Physik* **52**, 555 (1929).
- [58] N. W. Ashcroft and N. D. Mermin, *Solid State Physics* (Holt, Rinehart and Winston, New York, 1976).
- [59] J. M. Soler *et al.*, *J.Phys.-Condens. Mat.* **14**, 2745 (2002).
- [60] G. H. Wannier, *Phys. Rev.* **52**, 191 (1937).
- [61] C. Toher and S. Sanvito, *Physical Review Letters* **99**, 056801 (2007).
- [62] M. Büttiker, Y. Imry, R. Landauer, and S. Pinhas, *Phys. Rev. B* **31**, 6207 (1985).

- [63] E. Runge and E. K. U. Gross, Phys. Rev. Lett. **52**, 997 (1984).
- [64] M. Brandbyge, J. Mozos, P. Ordejón, J. Taylor, and K. Stokbro, Phys. Rev. B **65**, 165401 (2002).
- [65] M. W. Schmidt *et al.*, Journal of computational chemistry **14**, 1347 (1993).
- [66] H.-J. Werner and P. J. Knowles, The Journal of chemical physics **89**, 5803 (1988).
- [67] K. Andersson, P.-Å. Malmqvist, and B. O. Roos, The Journal of chemical physics **96**, 1218 (1992).
- [68] G. E. Scuseria, Chemical physics letters **176**, 27 (1991).
- [69] N. D. Drummond, A. J. Williamson, R. J. Needs, and G. Galli, Phys. Rev. Lett. **95**, 096801 (2005).
- [70] L. Landt *et al.*, Phys. Rev. Lett. **103**, 047402 (2009).
- [71] M. Vörös, T. Demjén, T. Szilvási, and A. Gali, Phys. Rev. Lett. **108**, 267401 (2012).
- [72] A. A. Fokin and P. R. Schreiner, Molecular Physics **107**, 823 (2009).
- [73] A. A. Spasov, T. V. Khamidova, L. I. Bugaeva, and I. S. Morozov, Pharmaceutical Chemistry Journal **34**, 1 (2000).
- [74] H. Huang, E. Pierstorff, E. Osawa, and D. Ho, Nano Letters **7**, 3305 (2007).
- [75] J. R. Schnell and J. J. Chou, Nature **451**, 591 (2008).
- [76] W. J. Geldenhuys, S. F. Malan, J. R. Bloomquist, A. P. Marchand, and C. J. Van der Schyf, Medicinal Research Reviews **25**, 21 (2005).
- [77] Y. Xue and G. A. Mansoori, International Journal of Nanoscience **07**, 63 (2008).
- [78] A. S. Barnard, S. P. Russo, and I. K. Snook, The Journal of Physical Chemistry B **109**, 11991 (2005).
- [79] A. V. G. Chizmeshya *et al.*, Chemistry of Materials **18**, 6266 (2006).
- [80] H. Uetsuka, D. Shin, N. Tokuda, K. Saeki, and C. E. Nebel, Langmuir **23**, 3466 (2007).
- [81] J. C. Randel *et al.*, Nature Communications **5** (2014).
- [82] J. P. Perdew *et al.*, Phys. Rev. B **46**, 6671 (1992).
- [83] N. Troullier and J. L. Martins, Physical Review B **43**, 8861 (1991).

- [84] T. Yanai, D. P. Tew, and N. C. Handy, *Chemical Physics Letters* **393**, 51 (2004).
- [85] J. Junquera, O. Paz, D. Sánchez-Portal, and E. Artacho, *Phys. Rev. B* **64**, 235111 (2001).
- [86] M. J. Peach *et al.*, *Physical Chemistry Chemical Physics* **8**, 558 (2006).
- [87] M. L. Zimmerman, M. G. Littman, M. M. Kash, and D. Kleppner, *Physical Review A* **20**, 2251 (1979).
- [88] S. Hirata and M. Head-Gordon, *Chemical Physics Letters* **314**, 291 (1999).
- [89] R. Richter *et al.*, *Physical Chemistry Chemical Physics* **16**, 3070 (2014).
- [90] T. Rander *et al.*, *The Journal of chemical physics* **138**, 024310 (2013).
- [91] M. Vörös and A. Gali, *Phys. Rev. B* **80**, 161411 (2009).
- [92] A. J. Arduengo, R. L. Harlow, and M. Kline, *Journal of the American Chemical Society* **113**, 361 (1991).
- [93] O. Schuster, L. Yang, H. G. Raubenheimer, and M. Albrecht, *Chemical Reviews* **109**, 3445 (2009).
- [94] J. C. Y. Lin *et al.*, *Chemical Reviews* **109**, 3561 (2009).
- [95] M. Niehues *et al.*, *Organometallics* **21**, 2905 (2002).
- [96] J. P. Wagner and P. R. Schreiner, *Journal of Chemical Theory and Computation* **12**, 231 (2016).
- [97] C. M. Crudden *et al.*, *Nat Chem* **6**, 409 (2014).
- [98] R. G. Nuzzo, B. R. Zegarski, and L. H. Dubois, *Journal of the American Chemical Society* **109**, 733 (1987).
- [99] D. Otálvaro, T. Veening, and G. Brocks, *The Journal of Physical Chemistry C* **116**, 7826 (2012).
- [100] P. J. Feibelman *et al.*, *The Journal of Physical Chemistry B* **105**, 4018 (2001).
- [101] B. Adhikari and M. Fyta, *Nanotechnology* **26**, 035701 (2015).
- [102] G. Henkelman, A. Arnaldsson, and H. Jónsson, *Computational Materials Science* **36**, 354 (2006).
- [103] D. Xiang, X. Wang, C. Jia, T. Lee, and X. Guo, *Chemical Reviews* **116**, 4318 (2016).

- [104] M. A. Reed, C. Zhou, C. J. Muller, T. P. Burgin, and J. M. Tour, *Science* **278**, 252 (1997).
- [105] A. Nitzan and M. A. Ratner, *Science* **300**, 1384 (2003).
- [106] Y. Matsuura, *Computational and Theoretical Chemistry* **1074**, 131 (2015).
- [107] A. Aviram and M. A. Ratner, *Chemical Physics Letters* **29**, 277 (1974).
- [108] T. A. Su, M. Neupane, M. L. Steigerwald, L. Venkataraman, and C. Nuckolls, *Nature Reviews Materials* **1**, 16002 (2016), Review Article.
- [109] D. M. Guldi, H. Nishihara, and L. Venkataraman, *Chem. Soc. Rev.* **44**, 842 (2015).
- [110] S. V. Aradhya and L. Venkataraman, *Nat Nano* **8**, 399 (2013), Review.
- [111] J. R. Heath, *Annual Review of Materials Research* **39**, 1 (2009).
- [112] J. K. Gimzewski and C. Joachim, *Science* **283**, 1683 (1999).
- [113] M. R. Stan, P. D. Franzon, S. C. Goldstein, J. C. Lach, and M. M. Ziegler, *Proceedings of the IEEE* **91**, 1940 (2003).
- [114] Q. Yan *et al.*, *Nano Letters* **7**, 1469 (2007).
- [115] T. B. Martins, R. H. Miwa, A. J. R. da Silva, and A. Fazzio, *Phys. Rev. Lett.* **98**, 196803 (2007).
- [116] S.-S. Yu and W.-T. Zheng, *Nanoscale* **2**, 1069 (2010).
- [117] W. Yao, K. Yao, G. Gao, H. Fu, and S. Zhu, *Solid State Communications* **153**, 46 (2013).
- [118] J. Prasongkit, A. Grigoriev, B. Pathak, R. Ahuja, and R. H. Scheicher, *The Journal of Physical Chemistry C* **117**, 15421 (2013).
- [119] S. Chakrabarty, A. H. M. A. Wasey, R. Thapa, and G. P. Das, *AIP Advances* **5** (2015).
- [120] D. H. Zhang, K. L. Yao, and G. Y. Gao, *Journal of Applied Physics* **110** (2011).
- [121] A. Pramanik, S. Sarkar, and P. Sarkar, *The Journal of Physical Chemistry C* **116**, 18064 (2012).
- [122] A. Batra *et al.*, *Nano Letters* **13**, 6233 (2013).
- [123] X. Q. Deng *et al.*, *Applied Physics Letters* **100** (2012).

- [124] J. Zeng, K.-Q. Chen, J. He, Z.-Q. Fan, and X.-J. Zhang, *Journal of Applied Physics* **109** (2011).
- [125] J. Zheng *et al.*, *The Journal of Physical Chemistry C* **115**, 8547 (2011).
- [126] H. Wang and Y. Leng, *The Journal of Physical Chemistry C* **119**, 15216 (2015).
- [127] B. Adhikari, S. Meng, and M. Fyta, *Nanoscale* **8**, 8966 (2016).
- [128] G. Sivaraman, R. G. Amorim, R. H. Scheicher, and M. Fyta, *Nanoscale* **8**, 10105 (2016).
- [129] P. Hohenberg and W. Kohn, *Phys. Rev.* **136**, B864 (1964).
- [130] W. Kohn and L. J. Sham, *Phys. Rev.* **140**, A1133 (1965).
- [131] W. Ding *et al.*, *Journal of Chemical Theory and Computation* **11**, 5888 (2015).
- [132] M. Paulsson and M. Brandbyge, *Phys. Rev. B* **76**, 115117 (2007).
- [133] H. W. Kroto *et al.*, *Nature* **318**, 162 (1985).
- [134] W. Kratschmer, L. D. Lamb, K. Fostiropoulos, and D. Huffman, *Nature* **347**, 27 (1990).
- [135] S. Iijima *et al.*, *Nature* **354**, 56 (1991).
- [136] D. Ugarte, *Nature* **359**, 707 (1992).
- [137] S. Iijima, *Journal of Crystal Growth* **50**, 675 (1980).
- [138] H. Terrones, M. Terrones, and W. Hsu, *Chemical Society Reviews* **24**, 341 (1995).
- [139] R. S. Ruoff, D. C. Lorents, B. Chan, R. Malhotra, and S. Subramoney, *Science* **259**, 346 (1993).
- [140] V. L. Kuznetsov, A. L. Chuvilin, Y. V. Butenko, I. Y. Mal'kov, and V. M. Titov, *Chemical Physics Letters* **222**, 343 (1994).
- [141] E. Thune, T. Cabioč'h, M. Jaouen, and F. Bodart, *Physical Review B* **68**, 115434 (2003).
- [142] T. Cabioč'h, J. Riviere, and J. Delafond, *Journal of Materials Science* **30**, 4787 (1995).
- [143] M. Chhowalla *et al.*, *Physical Review Letters* **90**, 155504 (2003).
- [144] R. Powles, N. Marks, and D. Lau, *Physical Review B* **79**, 075430 (2009).
- [145] D. Tománek, W. Zhong, and E. Krastev, *Physical Review-Series B* **48**, 15461 (1993).

- [146] S. Erkoc, Nano Letters **2**, 215 (2002).
- [147] S. Tomita, T. Sakurai, H. Ohta, M. Fujii, and S. Hayashi, The Journal of Chemical Physics **114**, 7477 (2001).
- [148] H. Kroto, Nature **359**, 670 (1992).
- [149] F. Banhart, Reports on Progress in Physics **62**, 1181 (1999).
- [150] B.-S. Xu, New Carbon Materials **23**, 289 (2008).
- [151] C. Brabec, A. Maiti, and J. Bernholc, Chemical Physics Letters **219**, 473 (1994).
- [152] H. Terrones and M. Terrones, Journal of Physics and Chemistry of Solids **58**, 1789 (1997).
- [153] K. R. Bates and G. E. Scuseria, Theoretical Chemistry Accounts **99**, 29 (1998).
- [154] H. Kroto, Science **242**, 1139 (1988).
- [155] A. Maiti, C. Brabec, and J. Bernholc, Physical review letters **70**, 3023 (1993).
- [156] F. Banhart and P. Ajayan, Nature **382**, 433 (1996).
- [157] O. Mamezaki, H. Adachi, S. Tomita, M. Fujii, and S. Hayashi, Japanese Journal of Applied Physics **39**, 6680 (2000).
- [158] V. Kuznetsov, Y. V. Butenko, A. Chuvilin, A. Romanenko, and A. Okotrub, Chemical Physics Letters **336**, 397 (2001).
- [159] T. Cabioc'h *et al.*, Journal of Applied Physics **91**, 1560 (2002).
- [160] N. Sano *et al.*, Journal of Applied Physics **92**, 2783 (2002).
- [161] J. K. McDonough *et al.*, Carbon **50**, 3298 (2012).
- [162] M. G. Fyta and P. C. Kelires, Fullerenes, Nanotubes, and Carbon Nanostructures **13**, 13 (2005).
- [163] B. W. Smith and D. E. Luzzi, Chemical Physics Letters **321**, 169 (2000).
- [164] C. Yeretjian, K. Hansen, F. Diederichi, and R. L. Whetten, Nature **359**, 44 (1992).
- [165] B. W. Smith, M. Monthieux, and D. E. Luzzi, Nature **396**, 323 (1998).
- [166] S. Bandow, M. Takizawa, K. Hirahara, M. Yudasaka, and S. Iijima, Chemical Physics Letters **337**, 48 (2001).
- [167] J. Sloan *et al.*, Chemical Physics Letters **316**, 191 (2000).

- [168] Y. Zhao, R. E. Smalley, and B. I. Yakobson, *Physical Review B* **66**, 195409 (2002).
- [169] E. Campbell, V. Schyja, R. Ehlich, and I. Hertel, *Physical Review Letters* **70**, 263 (1993).
- [170] Y. Xia, Y. Xing, C. Tan, and L. Mei, *Physical Review B* **53**, 13871 (1996).
- [171] J. Jakowski, S. Irle, and K. Morokuma, *Physical Review B* **82**, 125443 (2010).
- [172] M. Terrones, H. Terrones, F. Banhart, J.-C. Charlier, and P. Ajayan, *Science* **288**, 1226 (2000).
- [173] K. Lee, É. D. Murray, L. Kong, B. I. Lundqvist, and D. C. Langreth, *Physical Review B* **82**, 081101 (2010).
- [174] J. Klimeš and A. Michaelides, *The Journal of Chemical Physics* **137**, 120901 (2012).
- [175] S. Plimpton, *Journal of Computational Physics* **117**, 1 (1995).
- [176] J. Tersoff, *Physical Review B* **37**, 6991 (1988).
- [177] C. Sevik, A. Kinaci, J. B. Haskins, and T. Çağın, *Physical Review B* **84**, 085409 (2011).
- [178] L. Girifalco, M. Hodak, and R. S. Lee, *Physical Review B* **62**, 13104 (2000).
- [179] D. Golberg, Y. Bando, K. Kurashima, and T. Sasaki, *Applied Physics Letters* **72** (1998).
- [180] L. Hultman *et al.*, *Phys. Rev. Lett.* **87**, 225503 (2001).
- [181] D. Golberg, Y. Bando, W. Han, K. Kurashima, and T. Sato, *Chemical Physics Letters* **308**, 337 (1999).
- [182] M. F. Genisel *et al.*, *Journal of Applied Physics* **110** (2011).
- [183] K. Fukui, T. Yonezawa, and H. Shingu, *The Journal of Chemical Physics* **20** (1952).